Stony Brook University

Structure and Reactivity Studies of Size-Selected Transition Metal Sulfide Nanoclusters in the Gas Phase and Supported on Au(111)

A Dissertation Presented

by

Melissa Jean Patterson

to

The Graduate School

in Partial Fulfillment of the

Requirements

For the Degree of

Doctor of Philosophy

in

Chemistry

Stony Brook University

May 2009

Stony Brook University

The Graduate School

Melissa Jean Patterson

We, the dissertation committee for the above candidate for the Doctor of Philosophy degree, hereby recommend the acceptance of this dissertation.

Michael G. White, Ph.D., Advisor
Professor, Department of Chemistry
Senior Chemist, Brookhaven National Laboratory

David M. Hanson, Ph.D., Chairperson
Professor, Department of Chemistry

Trevor J. Sears, Ph.D., Third Member
Professor, Department of Chemistry
Senior Chemist, Brookhaven National Laboratory

Jan Hrbek, Ph.D., Outside Member
Senior Chemist, Brookhaven National Laboratory

This dissertation is accepted by the Graduate School

Lawrence Martin
Dean of the Graduate School

Abstract of Dissertation

Structure and Reactivity Studies of Size-Selected Transition Metal Sulfide Nanoclusters in the Gas Phase and Supported on Au(111)

by

Melissa Jean Patterson

Doctor in Philosophy

in

Chemistry

Stony Brook University

2009

The understanding of catalysts used in hydrodesulfurization (sulfur removal from petrochemical feedstock) is important from an environmental and economic standpoint as their efficiency directly correlates to atomospheric quality and fuel costs. Nanoparticles of MoS_2 supported on Al_2O_3 are used industrially for these reactions but the heterogeneity of such catalysts has limited the identification and in turn understanding of the catalytically active sites. Work presented here focuses on developing model catalytic systems where the chemical composition can be controlled in order to gain insight into those properties that are important for these catalytic processes and therefore can be tailored to increase selectivity.

Initial studies were directed towards generating $M_xS_y^+$ (M=Mo,W) clusters in the gas phase via magnetron sputtering. Using tandem mass spectrometry and a gas collision cell we were able to size-select the clusters of interest and react them in the gas phase with probe molecules such as CO. The resulting cluster adducts provided

information regarding the number of active metal sites and the geometry of the cluster. Density functional theory (DFT) calculations were used to search for the lowest energy structures of the bare $M_xS_y^+$ clusters and to obtain their relative stability for sequential CO binding. The calculated trends in CO binding energies were then compared to the experimental adduct distributions for assigning the ground state structures.

A size-selected deposition investigation was also done on the Mo_6S_8 cluster supported on Au(111). Carbonyl sulfide (OCS) undergoes a dissociation reaction on the Mo_6S_8 cluster that is substrate mediated as the Au(111) directly participates in the reaction. The OCS dissociatively adsorbs onto a molybdenum metal site, with the sulfur atom settling onto the Au surface and a CO molecule desorbing in the gas phase. This reaction is very unique in that the Au surface has an active role in the reaction mechanism and also lowers the barrier for OCS dissociation despite reports that the substrate is chemically inert. DFT calculations were done to observe local intermediates in order to generate a reaction pathway for the OCS dissociation on the Mo_6S_8/Au(111) system.

Table of Contents

List of Abbreviations

AES: Auger Electron Spectroscopy

BE: Binding Energy

DC: Direct Current

DOS: Density of States

DFT: Density Functional Theory

E_{ads}: Adsorption Energy

HDN: Hydrodenitrogenation

HDS: Hydrodesulfurization

HOMO: Highest Occupied Molecular Orbital

HYD: Hydrogenation

LUMO: Lowest Occupied Molecular Orbital

ML: Monolayer

QMS: Quadrupole Mass Spectrometer

RF: Radiofrequency

STM: Scanning Tunneling Microscopy

UHV: Ultra-High Vacuum

UPS: Ultraviolet Photoelectron Spectroscopy

XPS: X-ray Photoelectron Spectroscopy

List of Figures

List of Tables

Acknowledgements

It is with great joy that I acknowledge the numerous people that have helped me throughout my time at Brookhaven National Laboratory and StonyBrook University. I would first like to thank my advisor, Professor Michael G. White for his guidance throughout my time working in his laboratory. The great care he has for his students and his work has been greatly appreciated and without his mentorship I would have not been able to achieve this goal. I also wish to thank my advisement committee, Professors Dave Hanson, Trevor Sears, and Dr. Jan Hrbek for their support and direction in my developing career.

I am grateful to my colleagues, group members, and friends for their help, support, and advice. I would particularly like to thank Dr. James Lightstone for his tutelage in using our various laboratory instruments and Dr. Jillian Horn for always being a friend and providing comic relief during my long days at the laboratory. Lastly I'd like to thank Dr. David Sporleder and Daniel Wilson for simply being good friends and friendly faces.

I would not be here today if it were not for the many loved ones who have provided me with advice and encouragement during my time in graduate school. I am forever indebted to my family, Leonard, Martha, Lenny, and Kevin Patterson who are my world. I love you all very much and this accomplishment is as much yours as it is mine, where it not for all of you I would not have survived! And finally to my =M=, you opened my eyes to the beauty of Long Island and for that I will always remember my time here. POP!

List of Publications

1. Patterson, M.J.; Choi, Y.; Liu, P.; White, M.G., *"Dissociation of OCS on the Mo_6S_8 Cluster Supported on Au(111): Importance of the Cluster-Support Interface",*submitted.
2. Patterson, M.J.; Lightstone, J. M.; White, M. G., *"Structure of Molybdenum and Tungsten Sulfide $M_xS_y^+$ Clusters: Experiment and DFT Calculations"*, Journal of Physical Chemistry A, 2008, 112, 12011-12021.
3. Lightstone, J. M.; Patterson, M.J.; Liu, P.; Lofaro, J.C.; White, M. G., *"Characterization and Reactivity of the $Mo_4S_6^+$ Cluster Deposited on Au(111)"* Journal of Physical Chemistry C, 2008,112,11495-11506.
4. Liu, P; Lightstone J.M.; Patterson, M.J.; Rodriguez J.A.; Muckerman J.T.; White M.G., "*Gas-phase Interaction of Thiophene with the $Ti_8C_{12}^+$ and Ti_8C_{12} Met-Car Cluster",* Journal of Physical Chemistry B, 2006, 110, 7449-7455.
5. Lightstone, J.M.; Patterson, M.J.; Liu, P.; White, M.G., ***"****Gas Phase Reactivity of the $Ti_8C_{12}^+$ Met-car with Tri-atomic Sulfur Containing Molecules: CS_2, SCO, and SO_2"*, Journal of Physical Chemistry, 2006, *110,* 3505-3513.
6. Lightstone, J.M.; Patterson, M.J.; White, M.G., "*Reactivity of the $M_4S_6^+$ (M=Mo,W) Cluster with CO and NH_3 in the gas-phase: An experimental and DFT study",* Chemical Physics Letters, 2005, 413, 429-433.

Chapter 1. Introduction

The work presented in this dissertation aims to give insight into the role of size, structure, and chemical composition of transition metal sulfide nanoparticles as it pertains to model systems in catalysis. Transition metal sulfides such as MoS_2 and WS_2 have been the topic of much interest because of their ability to form well organized cage structures on the nanoscale. Like carbon, the S-M-S layered structure of the metal sulfides has a high propensity for forming folded structures such as hollow nanotubes, nanoctahedra, and nanonions.[1-6] Metal sulfide nanomaterials also display a wide range of unique catalytic, photovoltaic, and lubricant properties.[7-9] For example, MS_2 nanotubes have shown potential as a hydrogen storage media[10] whereas small MoS_2 nanoplatelets exhibit size-dependent band-gaps and are active photo-oxidation catalysts.[8] Small nanoplatelets of MoS_2 (1-5 nm) are also considered to be the active species in commercial HDS catalysts[11] whereby impurities are removed from petrochemical feedstock which is an important application as it directly affects the cost of fuel and has environmental impact as well. Not only have experimental methods examined metal sulfide nanomaterials, but theoretical studies[12-21] have been used to look at the unique atomic and electronic properties that these materials possess in this small size regime. Theory proves to be an essential tool when looking at these small systems in order to give a comprehensive look into its atomic structure and mechanistic properties in reaction processes. The research presented herein employs model systems to investigate the structural and chemical implications small size selected nanoclusters have in catalysis both in the gas phase and supported on Au(111).

The study of clusters has allowed an opportunity to evaluate the fundamental properties of nanosized systems as they are being formed atom by atom. Nanoclusters can be synthesized both chemically and in the gas phase and these methods strive to produce nanophase materials in a homogenous fashion. Chemical approaches to nanosized metal particles start with the reduction of positively charged metal atoms.[22] Ligand stabilization is often used in cluster generation and a careful addition of ligand molecules and reducing agents allows for *some* control in the size of the clusters produced. Gas phase methods have proved to be a more suitable way to produce clusters with a known stoichiometry, via supersonic nozzle techniques[23,24], oven sources[25], and plasma techniques such as laser ablation[26-31] and magnetron sputtering.[32-35] In these gas phase methods, mass spectrometry is used to select different particles or clusters according to mass and interest. In the work described here, we use a cluster beam apparatus that utilizes magnetron sputtering to form ionic transition metal sulfide clusters (Chapter 2). Cluster beam lines have been used previously in order to form a focused beam of cluster ions that can be used to study size-selected clusters.[36,37] The unique properties of clusters was first realized with the observation of magic numbers and seen experimentally in the gas phase via supersonic expansion among the noble gases, specifically xenon, by Echt *et.al*.[23] The appearance of high intensity peaks in the mass spectrum sparked interest in the investigation of these particular cluster sizes and the causes for their apparent stability. Preliminary findings indicated that the magic numbers for rare gases were governed by close packing criteria and aggregates of full-shell clusters with face centered cubic or icosahedral structures.[23] For simple metal clusters , like alkali

metals, the origin of the magic numbers depends on cluster size.[38] For small transition metal clusters and cluster alloys (Cu_x, Ag_x, Cu_xPb_y…), the magic numbers 2,8,20,40…, were attributed to closure of an electronic shell, the same effect that gives the noble gases their inertness and chemical stability.[38,39]

Molybdenum and tungsten sulfide nanoclusters have exhibited magic number properties as a consequence of their abundance in mass spectra both as anions and cations.[34,40] However, while the general features of magic cluster formation discussed above can provide a qualitative basis for the appearance of these stable geometries, such considerations would not fully explain the existence of covalently bonded structures like the M_4S_6 (M =Mo,W), whose unique combination of electronic and atomic structure leads to its stability. Specifically, it has been demonstrated that along with its highly symmetric structure, the large HOMO-LUMO[40,41] gap gives rise to its abundance in the mass spectra and consequently defines its magic-like nature.

Research done on supported metal particles has given evidence that the unique behavior of small particles are carried over from the gas phase to single crystal surfaces. Work done by Poppa *et al*., showed how the interactions between simple gases and Pd thin films varied with the change in the physical properties of the supported metal clusters such as particle size, density, and orientation.[42] It was found that the CO desorption energies between the deposited metal clusters and that of the bulk metal, varied considerably sustaining the idea that the size of the supported metals greatly altered the properties of the cluster-surface interface. As the atoms at the surface and the edges have lower coordination than those in the interior, these

atoms are especially active towards adsorbates.[22] Hence, small clusters are generally expected to be more reactive.

Single layer MoS_2 nanoparticles have been synthesized on Au substrates as models for hydrotreating catalysts and have been studied by imaging, spectroscopic techniques and density functional theory.[43-47] In bulk form, gold is considered an unreactive metal and the closed packed Au(111) surface has often been used as a non-interacting substrate for studying the electronic structure and reactivity of supported metal[48-50] and metal compound[51-53] nanoparticles. However, growth of sulfur rich nanoplatelets[46] and strongly bound clusters on the surface[54-56] has demonstrated that the substrate may modify the properties at the nanoparticle support interface. Of particular interest are recent experimental studies of small molybdenum sulfide nanoclusters formed on the Au(111) surface which are used to explore the atomistic details of desulfurization reactions that are relevant to the industrial hydrotreating of fossil fuels.[33,43,45,47,57,58] MoS_x aggregates deposited on Au(111) were able to dissociate thiophene upon adsorption at room temperature as given by XPS.[47] It was seen that as the temperature on the Au surface was increased, extra S 2p signal was observed as a result of atomic sulfur produced by the decomposition of thiophene on the surface. Further studies done by Besenbacher and co-workers saw the formation of triangular MoS_2 nanocrystals on the surface of the Au and has shown that the HDS activity is associated with coordinatively unsaturated metal edge sites that are seen as bright metallic, or "brim" states in a STM image. When pre-treated with hydrogen, DFT showed that the brim states were able to catalyze the hydrogenation of the

carbon double bonds in the presence of thiol groups as well as activate and break the initial carbon-sulfur bond of the hydrogenated thiophene.

Initial studies presented in this dissertation began with gas phase production and size selection of these nanoclusters using tandem mass spectrometry to look at cluster adduct formation with CO molecules (Chapter 3). This provided information about the relative stability of the clusters as well as structural information. Structure is vital in understanding local electronic environment and available sites for reactivity. DFT calculations were used to search for the lowest energy structures of the bare metal clusters and to obtain their relative stability for sequential CO binding. The calculated trends in CO binding energies were then compared to the experimental adduct distributions in order to assign ground state structures. In this way, it was possible to distinguish between nearly isoenergetic isomers for some of the clusters as the most stable/probable structure would give a CO stabilization energy trend consistent with experimental observations.

In light of the previous studies done on supported sulfide nanoparticles on Au(111) [43-50,54-56], we have chosen this substrate for the size-selected deposition of Mo_xS_y nanoclusters (Chapter 4). This gave the advantage of knowing the exact species being deposited on the surface generating a homogeneous system to study using surface science techniques such as UPS, AES, and TPD. Chemical and thermal properties of an array of Mo_xS_y clusters deposited on Au(111) were then investigated.

Finally, the Mo_6S_8 cluster was chosen for a more thorough study on the Au(111) with regards to characterization and reactivity with OCS (Chapter 5). As the metal sulfide particles become very small, i.e., molecular clusters, other structural

motifs have been observed that are nonstoichiometric. These include the Mo_6S_8 moiety that contains an octahedral Mo_6 metallic core that is the building block of the Chevrel phase of MoS_2, e.g., the superconducting AMo_6S_8 compounds (A = main group, transition, or lanthanide metal).[59,60] Crystalline Chevrel phases and amorphous ternary molybdenum sulfides have been found to be active catalysts for methanethiol synthesis and hydrodesulfurization.[61] The interaction of OCS on the Mo_6S_8 supported on Au(111) was studied using thermal desorption. Deposition on Au(111) was supported by recent DFT calculations indicating that the Mo_6S_8 should bind structurally sound on the Au substrate with a binding energy of -1.69eV.[55,56] DFT proved to be an important tool in our studies as well, providing insight to the reaction pathway for the dissociation of the molecule on the surface. This system provides a model for a simple desulfurization reaction which can be studied accurately both experimentally and theoretically. The use of single crystal surfaces to study processes of adsorption, desorption, and simple reaction mechanisms has proven to be a useful way to study important properties of supported nanosystems.[62]

Chapter 2. Experimental Methods

2.1 Cluster Beam Apparatus

All of the experiments in this dissertation were run on a cluster beam apparatus that was constructed at the Chemistry department at Brookhaven National Laboratory. A schematic of the apparatus can be seen in Figure 2.1. There are five separate sections: 1) magnetron sputtering source, 2) quadrupole ion guide, 3) quadrupole mass selector, 4) hexapole ion guide equipped with a gas collision cell, and 5) a UHV chamber. The arrangement of the apparatus serves two purposes. The first is to form a focused cluster beam of ions and the second is for differential pumping. The clusters are born in the cluster source at very high pressures and the chambers allow for differential pumping so that the UHV chamber can maintain a pressure $\leq 1 \times 10^{-9}$ torr. The following chapter will serve as a summary of each of these sections.

2.1.1. Magnetron Sputtering Source

In this work we use a commercially made magnetron sputtering source (Oxford Applied Research NC200U) to generate metal cluster compounds in the gas phase. The source is based off a design developed by Haberland[63,64] in the early 1990's. A detailed view of the magnetron sputtering source can be seen in Figure 2.2. In order to begin the formation of the plasma a sputtering gas, in this case Ar, is introduced into the housing of the magnetron. A bias voltage is then applied through water cooling lines to the back of the target while the magnetron cover is held at ground. A glow discharge is arced as a result of the voltage bias (~200V) at the interface of the metal target. The Ar atoms are ionized to Ar^+ within the plasma and

are confined to the face of the target as a result of the magnets. The Ar^+ ions are then subsequently accelerated towards target and begin to sputter metal particles. In all of the work presented herein, we use a reactive gas mixture of 4% H_2S in Ar in order to form sulfided metal nanoclusters. The sputtered metal particles that are formed are very energetic and so high pressure He is used in the condensation region (see Figure 2.1) in order to cool the particles through collisions, promoting clustering of the metal particles.[63]

2.1.2 Quadrupole Ion Guide and Mass Spectrometer

The quadrupole ion guide acts as an added differential pumping region as well as an extraction region for the newly formed cation clusters. Here we use an RF quadrupole ion guide to transport the ions into the next chamber that houses the mass spectrometer. This technique has been used widely in ion studies done in and a detailed description of method in which the ion guide transports ionic species is presented in work done by Gerlich.[65] In short, the ion guide works as a two-dimensional ion trap where ions can be confined by a RF field (600 kHz) that is applied to the rods at opposite phases. RF voltages in this way are applied in equal but opposite potentials to the two sets of rods.[66] A bias voltage or dc "float" potential is normally applied during operation between ~150V-250V to give a centerline potential within the ion guide. This value is optimized during operation to maximize regions of the mass spectrum that are of interest. Once extracted from the ion guide the resulting mass distribution can be analyzed in a commercial mass spectrometer that has been purchased from Extrel, CMS.

The quadrupole mass spectrometer acts similarly to that of the ion guide except that along with and RF field, a DC field is also applied to the rods. Basic operation involves varying the RF amplitude while fixing the ratio between the DC and RF voltages.[67] The mass spectrometer is very efficient in transmitting ions and we are able to acquire unit resolution with our current system.

2.1.3 Hexapole Ion Guide and Collision Cell

A hexapole ion guide with a built in collision cell is used to extract mass selected clusters from the mass spectrometer and allow them to react in the gas phase with different reactive molecules. Tandem mass spectrometry of gas phase ion molecule reactions such as collision induced dissociation and titration of metal sites have been used previously to study gas phase reaction chemistry.[26,68-71] Typically higher order ion guides are used for these types of studies therefore a hexapole was selected.[72,73] In our work, we use the collision cell primarily for titration of available metal sites using simple adsorption molecules such as CO and NH_3. Ionic products generated in the hexapole are then focused through a series of electrostatic lenses and detected with another mass spectrometer. Just as the previously described ion guide, we run at frequencies on the order of 600Hz with dc "float" potentials between ~15-30V.

2.2. UHV Chamber

Along with doing tandem mass spectroscopy of gas phase reactions of the resulting clusters generated in our magnetron source, we have the ability size select and deposit clusters of interest onto single crystal substrates. The following section will serve as a description for the active components for the deposition process in our

machine. The UHV chamber has several surface science instruments that allows for characterization and reactivity of the deposited clusters. The upper and lower levels of the UHV chamber as shown schematically in Figure 2.3.

2.2.1 Quadrupole Bender

The magnetron cluster source produces both ionic and neutral clusters. When depositing, it is key that the cluster of interest is the only species on the surface. Since we are unable to detect neutral species in the mass spectrometer, a quadrupole bender has been attached to the final hexapole ion guide before deposition. This allows for the deflection of cationic species onto the substrate, while neutral species are unaffected and pass through the bender. The quadrupole bender is made up of four cylindrical rod electrode sectors whose voltages are controlled by external power supplies. Entrance and exit lenses are used to create fringe fields that will enhance the throughput of the quadrupole deflector.[74] The addition of the electrode apertures converges the cluster beam within the deflector in order to focus the ions towards the exit lens increasing throughput. The potential of each sector of the quadrupole bender is optimized for maximum ion current.

2.2.2 Single Crystal Substrate: Au(111)

We use Au(111) as the single crystal substrate for deposition studies done in this work. Au(111) was selected as a substrate because its structure has been widely studied in literature and is believed to be chemically inert.[47-49,75] The crystal is 10mm in diameter and is electropolished on one side. A groove of 0.5mm is machined along the edge so that the crystal can be wrapped in tantalum wires and mounted. Figure 2.4 shows a schematic view of the Au(111) crystal mounted on a

UHV feedthrough (CeramTec). The tantalum wire that surrounds the crystal is spot welded to 1.0mm tantalum posts that are fitted onto copper blocks. This thermal contact is essential for resistively heating the crystal via a DC power supply (KEPCO) and cooling via a liquid N_2 bath. Temperature is monitored using a Eurotherm temperature controller which acquires information from a K-type thermocouple that is in direct contact with the back of the crystal. The crystal can be cooled to ~92K and heated to ~850K.

In order to remove surface contaminants on the crystal prior to deposition, a series of sputtering and annealing cycles are done. An ion gun (Model-20-045, Physical Electronics) is used to sputter the crystal with Ar^+ ions. The chamber is backfilled with $\sim 5.5\times10^{-5}$ torr of ultra high purity Ar (Matheson Tri-gas). The sputter gun is aligned to the face of the crystal and is manipulated to maximize the ion current measured using a picoammeter (Keithley). The ion gun is run at 0.5-1.0keV which gives ion currents between 2-4μA. After a sputtering cycle lasting 30 minutes, annealing the crystal is necessary to repair the surface. This is typically done for approximately 10 minutes at a temperature of ~800K. This is repeated three times to ensure all impurities are removed.

2.2.3 Auger Electron Spectroscopy

Auger Electron Spectroscopy is used as a spectroscopic technique to identify chemical species on a surface through core-level electron transitions. It has high sensitivity for chemical analysis in regions between 5-20Å on the surface.[76] Auger analysis is performed in UHV and utilizes an electron beam with enough energy (~1.5-5kV) to excite and eject an electron from a core-hole shell such as a K-shell

(see Figure 2.5). The resulting ionized atom that remains is highly excited and will relax back to a lower energy state by x-ray fluorescence (photon emission) or Auger emission (ejection of an electron from a higher energy state). In the Auger process the core hole is created and then occupied by an electron from a higher energy state and the energy from this transition allows for an Auger electron to be emitted simultaneously. The nature of the Auger transition is described by the energy level of the initial core hole and the resulting final two holes (Figure 2.5 depicts a KLL transition). The kinetic energy of the Auger electron can be detected using a hemispherical electron analyzer and is unique to a specific element, therefore allowing for information of all chemical species present on the surface.

In the experiments herein Auger electrons are produced using an electron gun (EQ 22/35, SPECS) at an operating voltage of 5.0kV with a beam current of ~10-50nA. The electrons are observed using a 100mm hemispherical analyzer (Phoibos 100, SPECS). The single crystal substrate is positioned normal to the analyzer with incident electrons striking the surface at 45º and data acquisition software provided by SPECS is used to monitor resulting electron energies.

2.2.4 Ultraviolet Photoelectron Spectroscopy

Ultraviolet Photoelectron Spectroscopy is another sensitive technique that can probes the BE of electrons emitted from the valence shell of a surface species. It is performed using a He gas discharge source that produces photons of HeI radiation (21.22eV). In our studies we use a He capillary discharge lamp (Model 628, McPherson), that is operated under a continuous flow of He gas in the cathode region which is water cooled. The discharge achieved by applying a high voltage (Model

730, McPherson) to the anode. A capillary tube guides the resulting radiation to the face of the sample. The sample is positioned normal to the hemispherical analyzer while the striking radiation is at 45º from the crystal face. Maximization of signal is achieved by manipulating the position of the crystal versus the lamp.

2.2.5 Temperature Programmed Desorption

Temperature programmed desorption is an important surface science technique that is used to acquire information about adsorption/desorption processes of molecules bound to a surface. In principle, information regarding heat of adsorption (reversible and non-dissociative processes), molecular coverage information, energetics and kinetics can be obtained. TPD's in our laboratory are performed under UHV conditions where molecular species are adsorbed onto a single crystal substrate and heated in a linear fashion while a mass spectrometer detects the products evolving from the surface as a function of temperature. The peak shapes give information regarding the desorption kinetics while the peak temperature gives information about binding energies of the adsorbed species. For simple molecular adsorption and desorption of CO molecules, a first order desorption rate can be assumed.

The main application of TPD is the measurement of the kinetics of different surface processes and a Redhead analysis allows desorption energies and kinetics to be estimated. This analysis begins by assuming the desorption rate is described by a rate law of first order given by the following expression:

$$\frac{r_{des}}{N} = -\frac{d\Theta}{dt} = k \bullet \Theta \qquad (2.1)$$

where r_{des} is the desorption rate, Θ is the coverage and N is then number of surface sites. The rate constant k can then be described using an Arrhenius equation:

$$k = \nu \bullet \exp\left(-\frac{\Delta E_{des}}{RT}\right) \tag{2.2}$$

where ΔE_{des} is the desorption energy, ν is the pre-exponential factor, R is the universal gas constant, and T is the peak temperature. When combining both expressions the rate law is defined and referred to as the Polanyi-Wigner equation:

$$\frac{r_{des}}{N} = -\frac{d\Theta}{dt} = \nu\Theta \bullet \exp\left(-\frac{\Delta E_{des}}{RT}\right) \tag{2.3}$$

The Redhead analysis assumes that the experimental set up is such that the temperature, T, varies linearly with time, t:

$$T = T_0 + \beta t \tag{2.4}$$

where T_0 is the initial temperature and β is the heating rate. Combining equations 2.3 and 2.4 allows us to get an expression that varies with temperature, which is what we are monitoring in our desorption experiments:

$$\frac{r_{des}}{\beta N} = -\frac{d\Theta}{dT} = \frac{\nu\Theta}{\beta} \bullet \exp\left(-\frac{\Delta E_{des}}{RT}\right) \tag{2.5}$$

Therefore, at low temperature E_{des} > RT little desorption occurs and at high temperature $\exp(-E_{des}/RT)$ rapidly rises and the number of molecules desorbing peak at a certain temperature. Then at very high temperature all molecules desorb and the desorption approaches zero. This leads to the characteristic peak in a TPD spectrum.

The Redhead equation can then be rearranged to relate E_{des} to the peak of the desorption curve T_{max}, and this equation can be used to obtain desorption energies:

$$\Delta E_{des} = RT_{max}\left[\ln\left(\frac{\nu_1 T_{max}}{\beta}\right) - \ln\left(\frac{\Delta E_{des}}{RT_{max}}\right)\right] \qquad (2.6)$$

where R is the universal gas constant, T_{max} is the temperature as measured from the peak maximum, ν is the frequency or pre-exponential factor, and β is the heating rate in K/s (in our experiments we use a heating rate of 2 K/s for all desorption studies). An estimation of desorption energy can be obtained from the above equation by making ideal assumptions for a few of the values. The pre-exponential factor, ν, can be assumed to be $10^{13}s^{-1}$ and the last expression in equation 2.6 may be estimated to be 3.64.[77]

TPD spectra are acquired by first manipulating the substrate towards a directed doser for adsorption of a particular molecule. On occasion backfilling the chamber with a reactive gas can also be used to adsorb molecules of interest. In our system, it is necessary to cryogenically cool the single crystal prior to exposure to the reactive molecule if not, the molecules of interest would not be able to adsorb on the surface. Once the desired coverage is reached the crystal is then translated to the entrance of the mass spectrometer (Hiden Analytical). Multiple ion detection studies can be performed, that allows one to monitor several chemical species desorbing from the surface. A schematic of the TPD set up is shown in Figure 2.6.

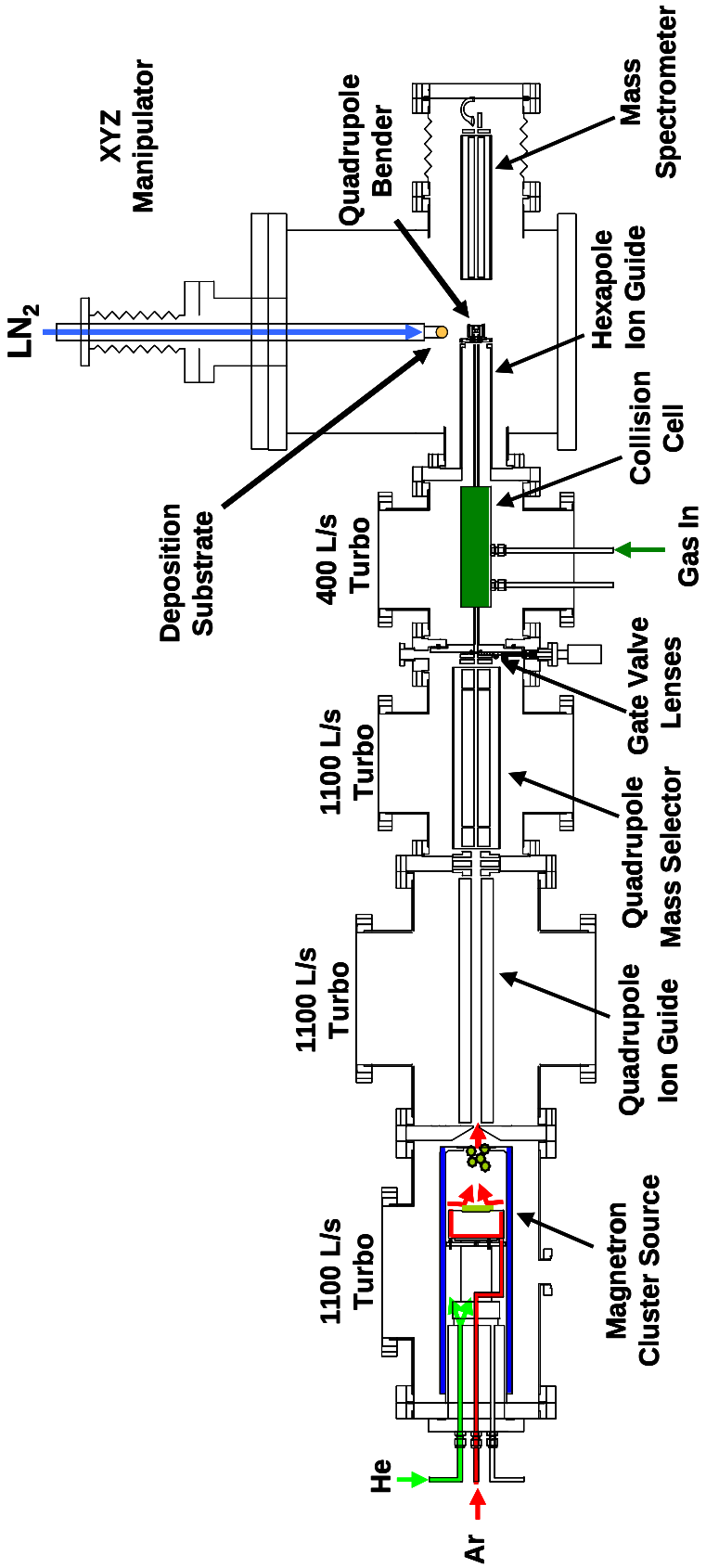

Figure 2.1: Schematic of cluster beam apparatus.

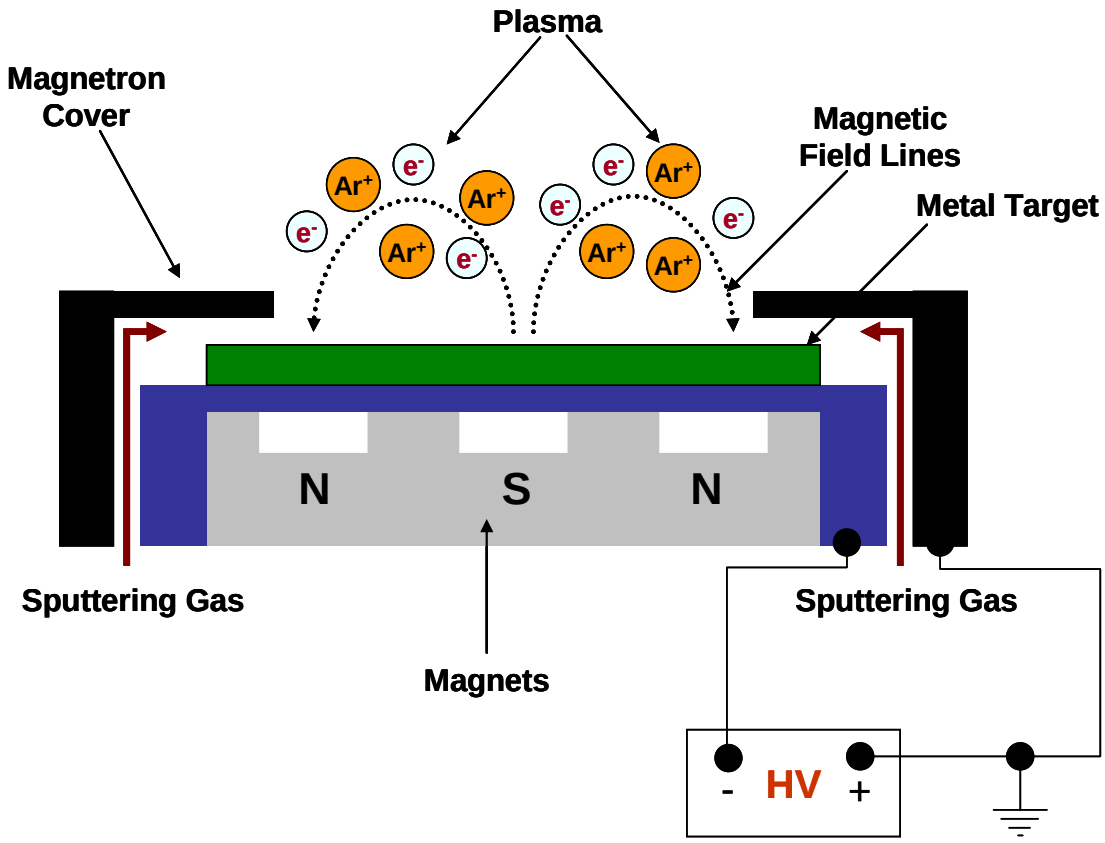

Figure 2.2: Detailed view of magnetron sputtering source.

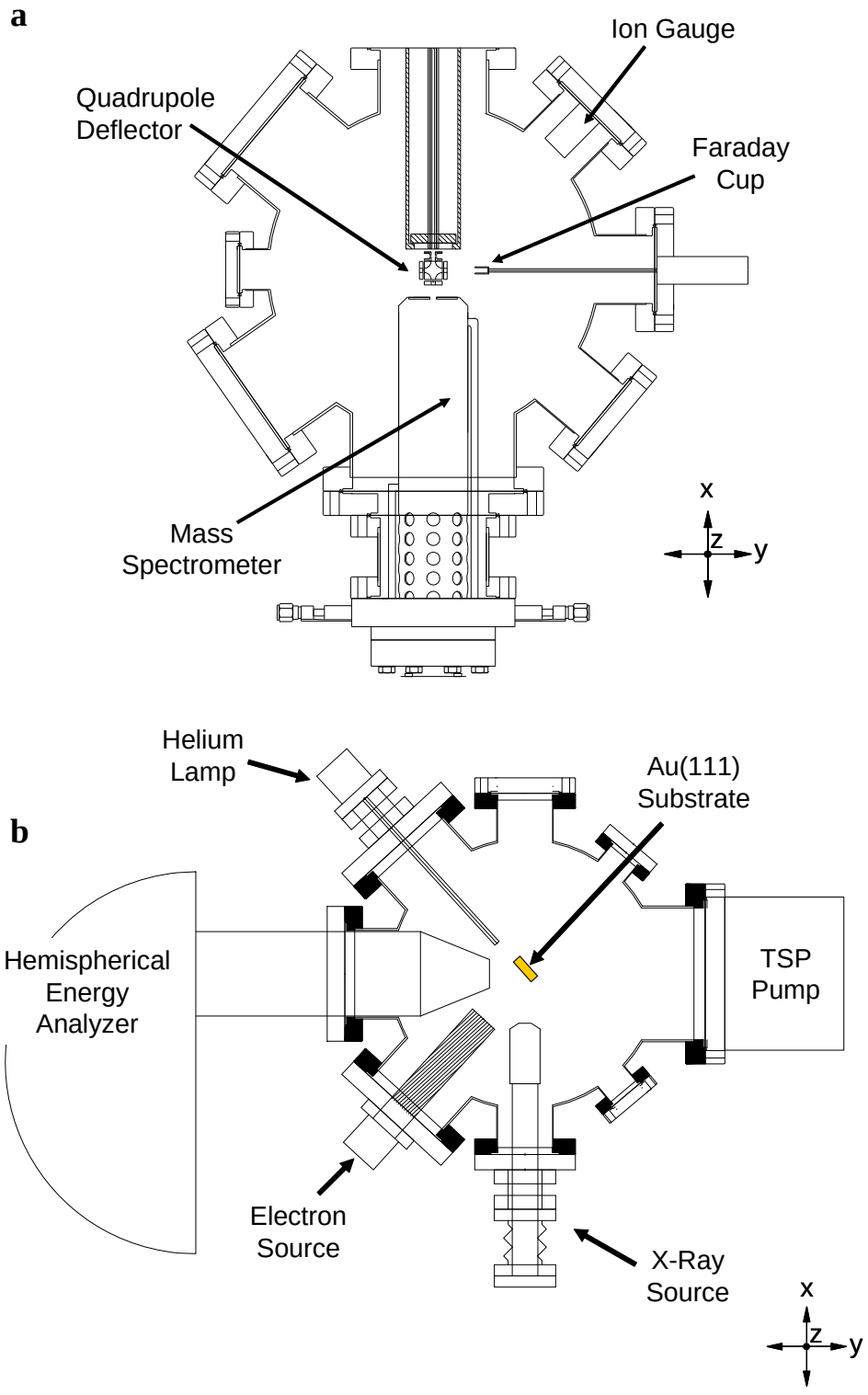

Figure 2.3: Schematic picture of the two levels of the UHV chamber, a) lower and b) upper.

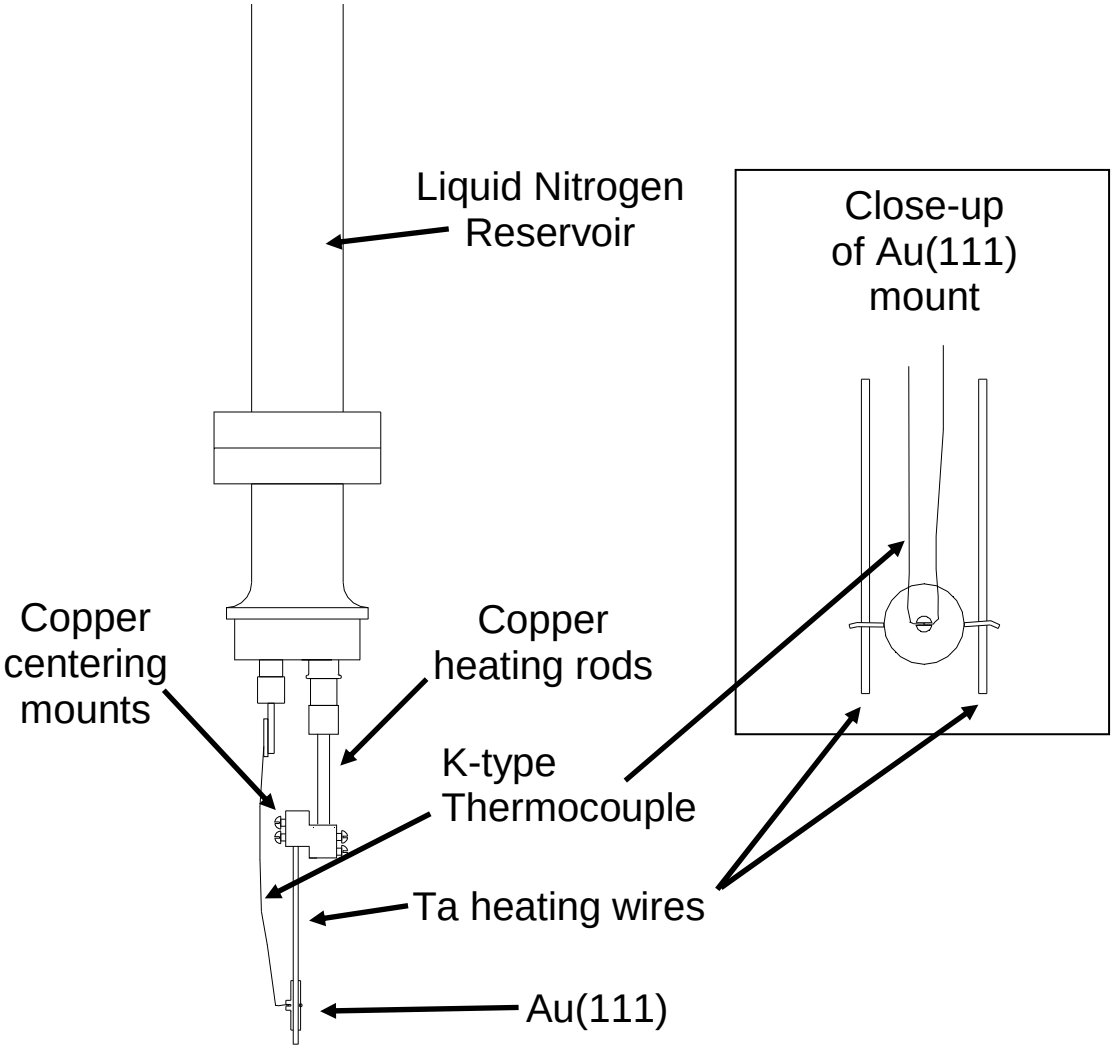

Figure 2.4: A schematic view of the Au(111) crystal mounted onto a UHV feedthrough is shown. The temperature is measured with a K-type thermocouple in direct contact with the back of the gold. The crystal is resistively heated by the tantalum wires and cooled with liquid nitrogen (92K – 850K). A detailed view of the Au(111) crystal mounting and thermocouple position is shown in the insert.

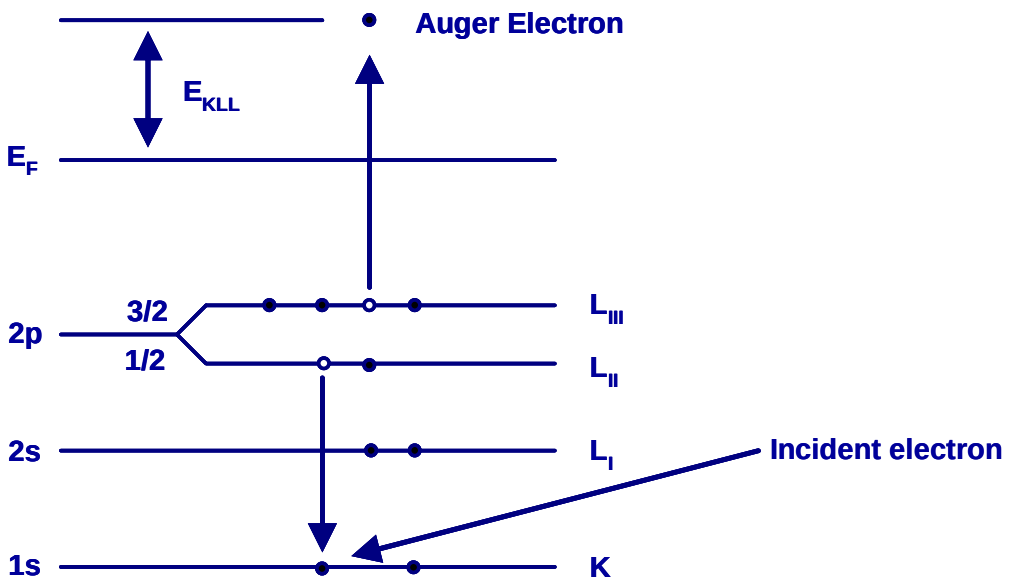

Figure 2.5: Schematic diagram of Auger electron emission.

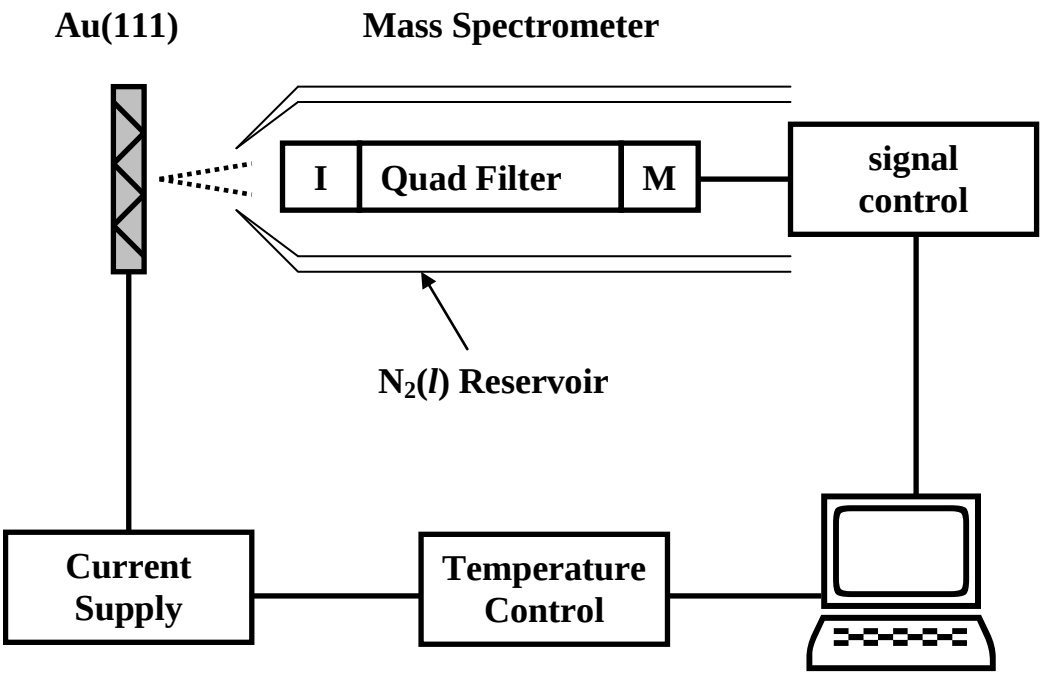

Figure 2.6: Diagram of the TPD set-up. The mass spectrometer that detects products from the surface is cooled by liquid N_2 through a shroud that encases it. Typical ionizer emission is 0.3mA, with an electron beam energy of 70eV. Multiplier values are on the order of 2100V.

Chapter 3. Structure of Molybdenum and Tungsten Sulfide $M_xS_y^+$ Clusters: Experiment and DFT Calculations

This section was published in *J. Phys. Chem. A*, 112, 12011-12021, 2008.

3.1. Introduction

The observation of small cluster units in the condensed phase has given rise to a number of experimental[30,40,78-83] and theoretical studies[12-20,84] of isolated metal sulfide clusters as a function of size and metal-to-sulfur ratio. In the case of molybdenum and tungsten sulfide, gas-phase cluster techniques using laser ablation and sputtering sources have been used to generate M_xS_y clusters as neutral,[30] anion[18,40] and cation[30] species with a wide range of stoichiometries. Experimental investigations are primarily limited to probes of reactivity and electronic structure, whereas the atomic structure of the clusters is derived mainly from theoretical calculations using DFT. A few clusters have been observed as "magic" due to their large abundance in anion and cation cluster mass spectra and large HOMO-LUMO gaps as determined by anion photodetachment spectroscopy. One such species is the M_4S_6 cluster (M = Mo, W) which is prominent in both anion[18,21,40] and cation cluster[34] mass distributions with measured HOMO-LUMO gaps of ~2 eV for the neutral cluster.[40] DFT calculations for the Mo_4S_6 cluster confirm its large HOMO-LUMO gap and predict a highly symmetric structure consisting of a Mo_4 tetrahedral core with the six sulfur atoms bridge bonded along the Mo-Mo edges.[18-21,30,40] The free Mo_6S_8 cluster with the "Chevrel" structure is also predicted to be a highly stable "magic" cluster with a relatively large HOMO-LUMO gap of 0.8-0.9 eV.[20,85] Murugan, et al, used DFT to show that that the structurally-related Mo_6S_{12}

stoichiometric cluster has a similar HOMO-LUMO gap (0.7 eV) as well as large magnetic moment ($4\mu_B$).[19] A general conclusion of these DFT studies is that the small, gas-phase M_xS_y (M = Mo and W) clusters energetically favor three dimensional structures with metal-metal bonding cores. These structures can be contrasted to the platelet structures of larger, near-stoichiometric M_xS_y nanoclusters which exhibit the same S-Mo-S layered structure of bulk MS_2. Nanoplatelets with sizes down to $Mo_{10}S_{24}$ have been recently observed in STM studies of self-assembled clusters on the surfaces of Au(111) and graphite.[44]

In the work reported in this chapter, we use the interaction of CO with mass-selected cluster beams to explore the structure of $M_xS_y^+$ (M = Mo, W) cation clusters. As demonstrated in a previous study of the $M_4S_6^+$ (M = Mo, W) magic cluster, a probe molecule such as CO or NH_3 preferentially binds to the exposed metal sites on the cluster. For these gas pick-up experiments, a beam of mass-selected $M_4S_6^+$ cluster cations is passed through a high-pressure collision cell containing the probe molecule (CO or NH_3) diluted in a He buffer gas. Mass analysis of the resulting cluster adducts, e.g., $M_xS_y^+(CO)_n$, provides information on the number and relative stability of the M-CO binding sites. In the case of $M_4S_6^+(CO)_n$, the product mass spectra showed that the cluster binds up to four (n = 4) probe molecules with only a small amount of n = 5 adduct observable. DFT calculations of the total CO adsorption energies for the lowest energy $M_4S_6^+$ structure were consistent with the binding of only four CO molecules, beyond which the M-CO binding energy decreased dramatically. This combination of experiment and theoretical analysis provided further evidence for the highly symmetric structure of the $M_4S_6^+$ cluster.

As a follow up to this earlier work on the $M_4S_6^+$ cluster, a combined experimental and computational study is presented of the structure and CO-adduct stability for the $M_2S_6^+$, $M_3S_7^+$, $M_5S_7^+$, and $M_6S_8^+$ clusters (M = Mo, W) which are the most prominent mass peaks in the $M_xS_y^+$ cation cluster distributions. In general, we find that the CO pick-up data is very sensitive to the individual metal-CO binding energies and can be used to distinguish between geometrical isomers that are predicted by DFT to have similar total energies. For the small, sulfur-rich $M_2S_6^+$ and $M_3S_7^+$ clusters, the experimentally favored geometries involve M-S-M bridge bonds and terminal sulfur bonds. The sub-stoichiometric $M_5S_7^+$ and $M_6S_8^+$ clusters are predicted to have metallic cores consistent with trends found in earlier DFT studies. In addition to probing the relative isomer stabilities, the DFT calculations also illustrate the effects of multiple CO binding, which can induce structural changes and/or break bonds within the cluster framework as more CO molecules are added. The latter may have implications for using such clusters deposited on supports as catalysts for heterogeneous reactions under high pressure (high coverage) conditions.

3.2 Experimental

The experimental work was performed on a cluster beam apparatus [32], described in Chapter 2, Section 2.1. The $M_xS_y^+$ clusters are formed by reactive sputtering of a metal target (Mo or W) with a mixture of 4% H_2S in Ar gas in a region containing high-pressure He gas (aggregation gas). Both the sputtering and aggregation gases are introduced into the source using variable leak valves with typical backing pressures of 7.6 Torr (4% H_2S/Ar) and 22 Torr (He) for Mo-sulfide, and 7.9 Torr (4% H_2S/Ar) and 24 Torr (He) for W-sulfide. The magnetron was

operated at a power of 185 watts. The length of the high-pressure He region between the metal target and first exit aperture (cluster condensation region) for Mo-sulfide was 0.75 inches and 1.25 inches for W-sulfide. The cluster ions leaving the source enter a quadrupole ion guide which transmits them to a quadrupole mass filter. A single cluster mass is then selected by its mass-to-charge ratio and then focused into a hexapole ion-guide which also houses a collision cell for the reaction of the cluster with different probe molecules. Mass spectra presented in this work were taken with the hexapole ion guide kept at ground potential, so that the relative ion-molecule collision energies mirrored the kinetic energy distribution of the incoming $M_xS_y^+$ ions (≤ 2 eV in the lab frame). Gases of interest, in this case CO, are introduced into the collision cell using a variable leak valve with the pressure measured by a capacitance manometer (MKS). The CO sample was introduced as a mixture of 25% CO in He gas. The He gas collisionally cools the cluster adducts following the addition of CO molecules. Typical collision cell pressures for these experiments were in the range of 10-15 mTorr. The products were mass analyzed by a second quadrupole mass spectrometer and detected by a channeltron electron multiplier. All experiments were performed at room temperature.

3.2.1 Computational Details

The theoretical calculations were performed on the $M_xS_y^+$ clusters using all electron DFT with the DMol^3 code. A double numerical basis set with p- and d-polarization functions, comparable in accuracy to a Gaussian 6-31G** basis set, was used with a real-space cut-off of 4.9 Å. The generalized-gradient corrected approximation (GGA), with the Becke exchange plus Lee-Yang-Parr correlation

(BLYP) functional was used. The FINE quality standard was chosen for tolerances of energy, gradient, displacement, and self-consistent field convergence criteria of 1×10^{-5} au, 2×10^{-3} au/Å, 5×10^{-3} Å, and 1×10^{-6} au, respectively. The calculations were performed with spin state unrestricted. All of the cation isomers have a doublet state (s = 1/2) as their final spin configuration with the exception of Isomer I (C_{3v} symmetry) of the $M_3S_7^+$ cluster which is a quartet (s = 3/2). In the case of the highly symmetric $M_6S_8^+$ cluster (O_h), where degenerate orbitals can give also rise to higher spin states, the low spin configuration (s = 1/2) is calculated to be the lowest energy. Therefore, all the clusters have a magnetic moment of 1 μ_B with the exception of the $M_3S_7^+$ cluster (Isomer I) which is 3 μ_B. Relativistic effects were included in the calculations for the heavier tungsten atoms in the $W_xS_y^+$ clusters.[86]

Density functional calculations were also used to examine the bonding of CO with the $M_xS_y^+$ clusters. The total adsorption energy was defined relative to the energies of the bare cluster and the number of free CO molecules, i.e.,

$$E_{ads}(n)= E_{(cluster+nCO)} - [E_{cluster} + nE_{CO}] \quad (3.1)$$

where n is the number of CO molecules bound to the cluster, $E_{(cluster+nCO)}$ is the energy of the CO cluster adduct, $E_{cluster}$ is the energy of the free cluster cation and E_{CO} is the energy of the free CO molecule. We also define the relative binding energy of a CO molecule to a cluster adduct as the change in total adsorption energies between adducts with one more adsorbate attached, i.e.,

$$\Delta E_{ads}(n) = E_{ads}(n) - E_{ads}(n-1) \quad (3.2)$$

Note that $\Delta E_{ads}(n)$ represents only an *apparent* CO binding energy as sequential CO addition can lead to structural changes that can significantly alter the stability of the

cluster adduct. Hence, it is somewhat oversimplified to attribute the total energy difference between the n and n – 1 adducts to the CO binding energy alone.

In general, the total energy for binding n×CO molecules depends on the specific metal locations of each of the CO molecules on the cluster, and only the lowest energy arrangements for sequential CO addition are presented in this work. For example, we searched for the lowest energy position of the first bound CO molecule to the $M_xS_y^+$ cluster ion, then searched for the lowest energy configuration among the remaining x-1 metal sites for the second CO molecule, and so on, until all the metal sites are occupied. This approach is justified based on the experimental evidence that multiple collisions with He gas are required to stabilize the internally "hot" adduct that results from CO addition. Simultaneous additions of CO are unlikely due to the large amount of internal energy (1-2 eV) that would be needed to be dissipated to prevent the CO molecules from simply boiling off the "hot" cluster adduct. Nonetheless, when the relative energies of different CO binding arrangements are small (< 0.1 eV), multiple adduct structures may be possible. Although many of these were explored in this work, we limit the discussion to only those that represent the minimum energy path for sequential CO addition.

Structural isomers examined in this work were based on those obtained in previous studies of metal sulfide clusters. A combination of theoretical [19,20] as well as experimental studies in the gas phase[41,87], solid state[59,60], and solution phase[88-91] provided preliminary structures with similar stoichiometry or M_xS_y fragments observed in our experiment. Structures with no imaginary frequencies were considered valid, and those that had total energies within ~2eV of the lowest energy

structure were chosen for further calculations of CO binding. Optimized structures and total energies were generated for sequential nCO binding and the energy trends compared with the experimental CO adduct product distributions. Structural assignments were based primarily on the correct prediction of the CO "saturation" limit, i.e., the point where the apparent CO binding energy for nCO molecules becomes positive or decreases appreciably relative to that of (n-1)CO (see equation 2). Except in the case of $Mo_6S_8^+$, the lowest energy isomers of the $M_xS_y^+$ clusters also yielded the best agreement with experimental trends in CO binding.

3.3 Results and Discussion

Figure 3.1 shows the mass spectra of the $M_xS_y^+$ (M= Mo,W) clusters produced by reactive sputtering. The mass spectra show "islands" of $M_xS_y^+$ clusters each having the same number of metal atoms but different number of sulfur atoms. The most prominent mass peaks within each cluster island are considered to be the most stable and can be assigned to $M_xS_y^+$ clusters with an x/y stoichiometry of 2/6, 3/7, 4/6, 5/7, and 6/8. The $M_4S_6^+$ cluster is observed as the most prominent mass peak over a wide range of source conditions and is considered a "magic number" cluster of unusual stability. In a previous study of the $M_4S_6^+$ magic cluster, we showed that gas-phase pick-up experiments using probe molecules such as CO and NH_3 could be used to provide information on the number of exposed metal sites and the overall structure of the cluster.[30] Similar experiments using CO as the probe molecule are presented here for the other prominent $M_xS_y^+$ clusters (M = Mo, W; x/y = 2/6, 3/7, 5/7, 6/8). The basic idea is that the observed mass distribution of the $M_xS_y^+(CO)_n$ cluster adducts is sensitive to the detailed structure of the cluster and its stability as CO

molecules are added. More specifically, the adduct distributions can help identify the ground state structure of the cluster from among the lowest energy isomers obtained by DFT geometry optimization. This is accomplished by comparing the observed adduct distribution with the calculated trends in total adsorption energies ($E_{ads}(n)$ in equation 1) for the different structural isomers.

The products observed from collisions of the cluster ions with CO correspond to simple cluster adducts in which CO adds molecularly, i.e.,

$$M_xS_y^+ + nCO \rightarrow M_xS_y^+(CO)_n \qquad (3.3)$$

Typically, the pressure of the He/CO gas inside of the collision cell was increased until the relative product yields were found to be approximately constant. Under these conditions, the most intense product masses are expected to correspond to the most thermodynamically stable CO adducts, with variations in reaction rates accounting for local minima or maxima in the adduct distributions. These assumptions are supported by previous ion beam studies of CO association reactions with metal cation clusters, where the most stable adducts (slowest reaction rates) are those that remain at higher CO/He pressures, especially the "saturated" adduct which has the most CO molecules possible for a given cluster ion.[70,92] As seen below, most of the CO adduct product distributions observed in this work exhibit a distinct cut-off corresponding to the CO saturated cluster. It is the prediction of this CO saturation limit that is used to distinguish between structural isomers generated by DFT geometry optimizations.

As is common in transition metal complexes, the most stable orientation for CO binding to the Mo atom sites of these clusters is through the carbon atom. In this configuration, CO bonding involves charge transfer to the partially empty d-orbitals

of the metal atoms through the CO 5σ orbital and back-donation of charge from the metal to the unoccupied CO $2\pi^*$ orbital in order to relieve some of the built up negative charge.[93] Previous DFT studies on larger molybdenum sulfide clusters, e.g., $Mo_{16}S_{32}$, show a binding energy of -0.95 eV[94] for CO on molybdenum which is typical of the binding energies reported here.

3.3.1 $M_2S_6^+$ Cluster

The adducts formed by collisions between CO and the smallest prominent cluster, $M_2S_6^+$, are shown in Figure 3.2. For both Mo and W, adducts with one (n = 1) and two (n = 2) CO molecules are observed, although the bare cluster is the primary product at all pressures studied in this work. The latter suggests weak metal-CO binding and/or dissociation of the adducts before they can be detected by the downstream mass spectrometer. A low sticking probability could be the result of the small size of the cluster (fewer internal degrees of freedom) which makes it difficult to dissipate the energy of adsorption even with multiple collisions with the He background gas. In the case of $Mo_2S_6^+$, very small product peaks are also observed for $3 \leq n \leq 7$, whereas the product distribution for $W_2S_6^+$ falls off more rapidly above n = 2.

The two lowest energy structures calculated by DFT for $Mo_2S_6^+$ are shown in Figure 3.3. Isomer I consists of four bridging sulfur atoms in between the Mo-Mo bond. The other two sulfur atoms are terminally bound to a single Mo atom. The Mo-Mo bond length is 2.82 Å which is comparable to interatomic distances and bond lengths of other Mo-Mo metal systems of the same stoichiometry.[20,88] The structure has a near C_2 symmetry and is predicted to be only 28.0 meV higher in energy than

the lowest energy structure, isomer II, also shown in Figure 3.3. Isomer II has near C_s symmetry with two bridging sulfur atoms connecting the two Mo atoms and four terminal sulfur atoms, two on each Mo atom. The isomer II structure was also found to be the lowest energy structure for the anion ($Mo_2S_6^-$) in the condensed and gas phases.[18,88] From the DFT calculations of Gemming, et.al., isomer II of Mo_2S_6 is expected to be the most stable among smaller Mo_2S_y clusters consistent with its large HOMO-LUMO gap (2.5eV). These authors noted that the high stability of the isomer II structure of Mo_2S_6 could represent a structural motif for larger Mo_xS_y clusters or the bulk phase MoS_3.[18] DFT calculations by He et. al. have found the same lowest energy structure for the $V_2S_6^+$cluster.[87]

Alongside each of the calculated structures for $Mo_2S_6^+$ (I and II) in Figure 3.3 are plots of the calculated total adsorption energy for the sequential addition of CO. Despite being nearly isoenergetic, the two isomers exhibit very different CO adsorption behavior. Specifically, isomer I shows a nearly linear change in E_{ads} from $n = 1$ to $n = 3$, suggesting that adducts with three (or even more) CO molecules should be observable in pick-up experiments. This prediction disagrees with the observed $Mo_2S_6^+(CO)_n$ product distribution (Figure 3.2) which shows almost no $n = 3$ adduct. By comparison, the calculated CO adsorption energies for isomer II plateau at $n = 2$. A similar trend is found for the calculated $n = 1$ and $n = 2$ CO adsorption energies of isomer II of $W_2S_6^+$. For both metals, the calculated trend in CO binding energies for isomer II (see Table 3.1) suggests that the primary product is the $n = 1$ adduct, in agreement with the experimental product distributions (see Figure 3.2). The fact that the experimental $n = 2$ product yield is smaller, especially in the case of

$W_2S_6^+$, indicates a small but non-zero binding energy for the second CO molecule. It is likely that the appearance of the n = 2 adduct depends sensitively on the second CO binding energy relative to the internal energy of the cluster; weakly bound CO molecules could be "desorbed" from the cluster before detection. The low probability for the n = 2 means that larger adducts (n ≥ 3) coming from sequential addition are very unlikely, consistent with the observed product distributions. Based on these comparisons, the structure of the $M_2S_6^+$ (M = Mo, W) cluster is assigned to isomer II. It is interesting to note that for isomer II of $Mo_2S_6^+$, the calculated CO binding energy for n = 2 is nearly zero, but dramatically increases again for n = 3 (see Table 3.1). By contrast, the CO binding energy for the n = 3 adduct of $W_2S_6^+$ (isomer II) is even smaller than n = 2. The difference in CO adsorption behavior can be more readily understood by viewing the optimized structures for the n = 2 and n = 3 adducts in Figure 3.4. It is seen that the adding a third CO to $Mo_2S_6^+(CO)_2$ causes one of the Mo-S-Mo bridge bonds to break. This opening of the cluster framework is clearly energetically favored, but this species is likely to be a short lived intermediate that undergoes further decomposition into smaller fragments. Any cation fragments resulting from dissociation would have masses well outside the range used to detect the cluster-CO adducts. By comparison, the $W_2S_6^+(CO)_3$ cluster remains intact, but the binding energy for the third CO molecule (see Table 3.1) is too small for the n = 3 adduct to be observed. As will be seen below, distortion or fragmentation of the cluster framework when the number of CO molecules exceeds the number of metal atoms is a general feature of these small $M_xS_y^+$ clusters.

3.3.2 $M_3S_7^+$ Cluster

The product mass spectra resulting from collisions between the $M_3S_7^+$ cluster with CO are shown in Figure 3.5. For both Mo and W, the most intense mass peaks correspond to CO adducts with $n \leq 3$, with the most probable product being $M_3S_7^+(CO)_2$. These observations are consistent with a cluster structure in which all three metal atoms are exposed and can bind CO, but with an overall stabilization energy that is a maximum for only two CO molecules (n = 2). Figure 3.6 shows the three lowest energy structures for the $M_3S_7^+$ clusters found by DFT geometry optimizations. Isomer I consists of a triangular metal core with two bridging sulfur atoms along each edge (total of 6). The seventh sulfur atom is face capped on one side of the metal triangle and the cluster has an overall symmetry of C_{3v} (3-fold axis perpendicular to plane of page in (Figure 3.6). Isomer I is thought to be the basic building block of a large number of compounds in the condensed phase such as $[NH_4]_2[Mo_3S_{13}]$[89,91] and the center of a trinuclear cluster complex with outer dithiolate ligands that has been identified as a novel molecular conductor.[90] Isomer II is structurally similar to I, but contains two face capping sulfur atoms, and has a lower symmetry (C_1). The lowest energy structure, isomer III, has C_s symmetry with each metal atom bonded to one terminal sulfur atom, two bridging sulfur atoms, and one face capping sulfur atom. Note that isomer I and II contain a triangular M_3 metal core whereas isomer III is predicted to have only one relatively long metal-metal bond (2.93Å).

The structures for the cluster adducts, $M_3S_7(CO)_n^+$, were geometry optimized and the total adsorption energies, $E_{ads}(n)$, were calculated for each of the three isomers. The computed trends in adsorption energies are shown in Figure 3.6. For

isomer I, the total adsorption energy, $E_{ads}(n)$, steadily increases to n = 6, after which it reaches a plateau. The calculated adduct structures for $n \geq 6$ (not shown) exhibit significant structural distortions which we attribute to steric effects associated with multiple CO binding to the metal atoms. The calculated adsorption energies for sequential CO addition to isomer II show similar behavior (Figure 3.6). For both isomers I and II, the calculated total adsorption energies predict that the n = 6 adduct should be observable, in clear disagreement with the experimental product mass spectra (Figure 3.5).

The calculated adsorption energies for isomer III show very different behavior for sequential CO binding (Figure 3.6). The calculated total adsorption energies for both Mo and W are seen to reach a plateau between n = 4 and n = 5, with the n = 6 adducts predicted to be even less stable. These trends are more easily seen from the apparent CO binding energies, $\Delta E_{ads}(n)$, shown in Table 3.2. For the $Mo_3S_7^+(CO)_n$ adducts, the apparent CO binding energies decrease by ~0.25 eV per added CO until n = 5 for which the binding energy is predicted to be essentially zero. The sequential CO binding energies for $W_3S_7^+(CO)_n$ exhibit a somewhat different behavior, with a large drop in apparent binding energy between the first (n = 1) and second (n = 2) CO addition, whereas the second (n = 2) and third (n = 3) additions have nearly the same binding energy. Beyond n = 3, the apparent CO binding energies for the W adducts steadily decrease and eventually becomes positive for n = 6.

Based on the calculated trends in consecutive CO binding energies, we would expect to observe the n = 4 adducts for isomer III for both the Mo and W clusters. In fact, the n = 4 adduct is observed as a small peak in the $Mo_3S_7^+(CO)_n$ mass spectrum,

but not in the product mass spectrum for the W cluster (see Figure 3.5). As previously found for the $M_2S_6^+(CO)_3$ adducts, the probability of observing the n = 4 adduct depends on the cluster's stability with respect fragmentation when the metal atoms bind more to than one CO molecule. The optimized structures for the n = 3 and n = 4 CO adducts are shown in Figure 3.7. For both Mo and W, addition of the fourth CO causes a M-S-M bridge bond to break. Based on the mass spectra in Figure 3.5, it would appear that the n = 4 adduct survives on the time scale of detection for the Mo cluster but not for the W cluster. According to the DFT optimization results (not shown), when a fifth CO molecule is added to the $W_3S_7^+(CO)_4$ adduct it undergoes in fragmentation into a $WS_3(CO)$ and $W_2S_4^+(CO)_4$ species. Although the latter behavior may be an isolated case, the DFT calculations support the idea that the smaller clusters become structurally unstable when the number of bonded CO molecules exceeds the number of metal atoms, even though the total CO adsorption energy may continue to increase.

Overall, the predicted trends in CO adsorption energies and adduct stability for isomer III are more consistent with the observed product mass spectra than that for isomers I and II for both the Mo and W clusters. Therefore, we assign the structure of the $M_3S_7^+$ cluster to that of isomer III (Figure 3.6).

3.3.3 $M_5S_7^+$ Cluster

The product distributions for the $M_5S_7^+$ clusters interacting with CO are shown in Figure 3.8. For both Mo and W, the observed products correspond to $M_5S_7^+(CO)_n$ adducts up to n = 6, with no higher mass products detected. The n = 5 adduct is the most probable for both the Mo and W clusters, although the n = 6 adduct peak for the

Mo cluster has nearly the same intensity. Although these clusters have only five metal atoms, the high probability for n = 6 suggests that they behave differently towards CO binding than the smaller clusters discussed above.

Figure 3.9 shows the two lowest energy isomer structures for the $M_5S_7^+$ cluster. Two other higher energy structures were also considered ($E_{relative} \geq 1$ eV), but are not presented since their predicted CO adsorption energy trends were also inconsistent with the observed CO adduct product yields. The higher energy structure, isomer I, consists of a trigonal bipyramidal arrangement of the five metal atoms with an overall cluster symmetry of C_{2v} (C_2 axis perpendicular to page in Figure 3.9). This structure maximizes the number of bridge bonded sulfur atoms and results in three sets of inequivalent metal atom sites, i.e., at the poles of the bipyramid, and two distinguishable sites in the equatorial plane. The lowest energy structure, isomer II, has as its core the tetrahedral Mo_4S_6 cluster whose compact cage structure has been shown to be especially stable as both an anion[40] and cation.[30] The fifth Mo atom is attached at the base of the tetrahedron via three sulfur bridge bonds and is capped by a triply bonded sulfur atom. Having no direct metal bonds, the fifth metal atom is more akin to the metal sites in the smaller $M_2S_6^+$ and $M_3S_7^+$ cluster. Isomer II has near C_s symmetry with the reflection plane bisecting the cluster perpendicular to the page (see Figure 3.9).

Also shown in Figure 3.9 are the calculated total adsorption energy plots for the sequential binding of CO to $Mo_5S_7^+$. For isomer I, the calculated total adsorption energy exhibits almost a linear increase up to n = 5, where it abruptly levels off with a relative CO binding energy close to zero ($\Delta E_{ads}(5) \approx -0.03$ eV). This calculated trend

in CO adsorption energies would predict that the $Mo_5S_7^+(CO)_n$ product mass spectrum would terminate at n = 4, whereas the experiments show that both n = 5 and n = 6 adducts are prominent products. Note that in adding a sixth CO molecule, the total adsorption energy increases sharply by ~2 eV. This adsorption behavior is reminiscent of the increase in adsorption energy between the n = 2 and n = 3 adducts of $Mo_2S_6^+(CO)_n$, which undergoes internal bond breaking with the addition of the third CO molecule (see Figures 3.3 and 3.4). Indeed, the DFT calculations predict that the addition of a sixth CO molecule to isomer I leads Mo-Mo bond breaking in the triangular metal core (not shown). Despite the high CO adsorption energy or ultimate fate with respect to dissociation, the probability for forming the n = 6 adduct of isomer I is small due to the low total adsorption energy of the n = 5 adduct which acts as its precursor in sequential addition. The predicted absence of the n = 5 adducts disagrees with the observed product mass spectrum (Figure 3.8), hence, isomer I is unlikely to be the correct structure of the $Mo_5S_7^+$ cluster.

The total CO adsorption energies for isomer II of the $M_5S_7^+$ cluster exhibit an almost linear gain with sequential CO addition up to n = 5, beyond which the adsorption energy begins to level off at n = 8 (see Figure 3.9; Table 3.3). The latter would predict adduct formation beyond what is observed experimentally (n > 6), but a more complete picture of adduct stability comes from consideration of the adduct structures. Figure 10 shows the calculated structures of the n = 5 to n = 7 adducts for isomer II of both Mo and W. It is clearly seen that the $M_5S_7^+$ core of the n = 6 adduct is significantly distorted from that of the bare cluster (see Figure 3.9) with two CO molecules bound to one of the equatorial metal atoms. The ability to accommodate

two CO molecules on one metal site is attributed to the metallic nature of the four metal atoms forming the inner tetrahedron. As seen in Figure 3.10, the seventh CO molecule preferentially binds to the metal atom that is separated from the M_4 tetrahedral core by three sulfur bridge bonds. Binding of CO at this metal site, however, leads to breaking two of the sulfur bridge bonds, with the $MoS(CO)_2$ fragment tethered to the larger $Mo_4S_6^+(CO)_5$ core of the cluster through the remaining bridge bonded sulfur atom. The observation of the internally fractured n = 7 cluster adduct will depend on its stability against further fragmentation on the time scale of our detection measurements. In this case, the dissociation of the n = 7 adduct into two smaller fragments may be energetically driven by the high stability of the "magic cluster" fragment, $Mo_4S_6^+(CO)_n$.[30] Dissociation would lead to cation species whose mass would fall outside the range of the intact cluster adducts in Figure 3.8 and were not detected. Hence, the calculated CO adsorption energetics for isomer II favor adduct formation for n = 1-6, but larger adducts may be subject to cluster fragmentation and dissociation. This overall picture for isomer II for both Mo and W is consistent with the observed product mass spectra that sharply terminate at the n = 6 adduct. Hence, we tentatively assign the structure of the $M_5S_7^+$ cluster cation to that of isomer II.

3.3.4 $M_6S_8^+$ Cluster

The product mass spectra resulting from interactions between the $M_6S_8^+$ (Mo and W) clusters and CO are shown in Figure 11. In the case of Mo, the n = 6 adduct is clearly the most favored product with only very small peaks at higher mass corresponding to CO adducts with n = 7-9. The CO adduct distribution for the W

cluster also shows a maximum at n = 6, however, the mass peaks corresponding to the bare cluster ion and the n = 1 CO adduct are of comparable intensity. A very small peak corresponding to the n = 7 adduct is also observed. The fact that the product mass spectra for both Mo and W exhibit a high probability for the n = 6 adduct is consistent with the qualitative expectation of one CO molecule bound on each of the six metal atoms of the $M_6S_8^+$ cluster.

Figure 3.12 shows the calculated lowest energy structures for the $Mo_6S_8^+$ cluster (the $W_6S_8^+$ cluster is structurally similar) as well as the calculated total adsorption energies for sequential CO addition to both the Mo and W clusters. The highly symmetric structure of isomer I has been previously identified as the building block of the well known Chevrel phase of molybdenum sulfide in $A_xMo_6S_8$ or $ABMo_6S_8$ solid state compounds.[61,95] The metal atoms of isomer I are arranged to form an inner octahedron with the sulfur atoms symmetrically placed in the triangular faces (near O_h symmetry).

Because the Mo_6S_8 moiety is known to have the "Chevrel" structure of isomer I in solid state and solution phase chemistry, it was expected that the calculated CO adsorption energies of isomer I would follow the experimentally observed CO adduct product distributions. In fact, the calculated total CO adsorption energies for Mo and W (see Figure 3.12) suggest that adducts with more than six CO molecules should be observable, whereas the experimental mass spectra show that adducts with n > 6 have very low probability. The theoretical result is perhaps not too surprising, as the $M_5S_7^+$ cluster with a similar metal internal framework was also predicted to bind more than one CO per metal atom. Nonetheless, the calculations for

isomer I show a significant decrease in the binding energy for placing two CO molecules onto a single metal site. Specifically, the decrease in apparent CO binding energy between the n = 6 and n = 7 adducts is 40% for Mo and 53% for W (see Table 3.4). The latter can be qualitatively understood by inspecting the optimized structures for the n = 6, 7 and 8 adducts shown in Figure 3.13. Relative to the n = 6 adduct, it is seen that the addition of a second CO molecule to a single metal atom site introduces strain into the cluster framework as well as reorientation of the nearby CO molecules to minimize repulsive interactions. As a result, the gain in energy resulting from binding additional CO molecules is offset by the strain and CO crowding introduced into the adduct structure. The balance between these two effects will determine the overall stability of the adduct, and the current calculations for isomer I yield the correct *trends* for the relative adduct stabilities, but appear to overestimate the CO binding energies of the larger adducts (n > 6).

In searching for other low energy isomers of $M_6S_8^+$, a geometry optimization was performed in which the beginning structure was that of a bulk MS_2 reduced to the proper stoichiometry. The resulting structure, isomer II (Figure 3.12), has a calculated total energy that is *lower* than isomer I for the Mo cluster (-0.22 eV) and *higher* than isomer I for the W cluster (+0.25 eV). The prediction of different lowest energy structures for the Mo and W clusters is unique among the small clusters studied in this work. The structure of isomer II is similar to isomer I except that two of the face centered sulfur atoms have moved to form a Mo-S-Mo bridge bond on one edge of the base of metal octahedron and a Mo-S dangling bond with one of the metal

atoms at the apex of the metal octahedron. These structural changes lower the symmetry of the cluster to C_s, but the metal atoms retain an octahedral configuration.

From Figure 3.12 and Table 3.4, it is seen that the trends in calculated total CO adsorption energies for isomer II are very similar to that for isomer I for both Mo and W. Moreover, the calculated CO binding energies for the n = 7 and n = 8 adducts are essentially identical for both isomer I and isomer II (see Table 3.4). The latter can be explained by inspection of the optimized CO adduct structures as illustrated for the n = 1-4 adducts of the $Mo_6S_8^+$ cluster in Figure 3.14. For n = 1-3, the CO adducts of isomers I and II retain their distinct structures. For n = 4, however, the geometry optimization procedure results in isomer II rearranging to form an n = 4 adduct of *isomer I*. It is also seen that the n = 4 adduct resulting from rearrangement of isomer II has one of the CO molecules in a different position from the calculated lowest energy structure for the n = 4 adduct of isomer I. As shown in Table 3.4, this difference in CO binding arrangement leads to somewhat different sequential CO binding energies for the n = 5 and n = 6 adducts. The differences in total energies for the adducts of isomer I and isomer II with n > 4, however, are relatively small ($\leq$ 0.02eV) and so these different CO addition pathways are probably indistinguishable under experimental conditions. Beyond n = 6, where all the metal atom sites are occupied by one CO molecule, the cluster adducts formed by either isomeric pathway are structurally identical and so are the n = 7 and n = 8 total adsorption energies. The calculated structures and CO adsorption trends for the $W_6S_8^+$ cluster are essentially the same as the $Mo_6S_8^+$ cluster discussed above.

Due to the similarities in the total energy of the CO adducts and the predicted isomer interconversion for adducts with $n \geq 4$, the experimental product distributions cannot provide unambiguous evidence for isomer I or II as being the preferred structure for the free $M_6S_8^+$ cation cluster. Previous DFT studies have reported the existence of both isomers with binding energies only ~0.1eV apart, with the Chevrel structure (isomer I) still being the most stable.[20] The present DFT calculation, therefore, gives a reasonable prediction of the relative isomer energies for the free $M_6S_8^+$ cation clusters. It is also possible that both isomer I and II coexist under the conditions of our cluster source or readily interconvert depending on the internal energy of the clusters and that adduct product distributions are an average of the two isomers in the gas phase. As shown above, however, isomer I is preferred in the presence of strongly interacting adsorbates like CO. This is consistent with the Chevrel structure being the most stable in other chemically bonded environments, e.g., deposited on surfaces[55,56] and in solid phases.[59,60]

3.4 Summary and Conclusions

In this work, we have used a combination of experiment and DFT to study the CO adsorption properties of several small metal sulfide clusters, $M_xS_y^+$ (M = Mo, W; x/y = 2/6, 3/7, 5/7, 6/8) as a way to probe the cluster's electronic and atomic structure. Specifically, the mass distribution of $M_xS_y^+(CO)_n$ adducts formed by collisions between the cluster cation and CO molecules is found to be very sensitive to cluster structure and provides a way to distinguish between low energy isomers predicted by theory. For the two smallest clusters, $M_2S_6^+$ and $M_3S_7^+$, the structural isomers differ by less than 0.1 eV, yet only the lowest energy structure yielded consecutive CO

adsorption energies that were consistent with the experimental data. The predicted ground state structures for the $M_2S_6^+$ and $M_3S_7^+$ clusters involve M-S-M bridge bonds as well as terminal sulfur atoms on each metal atom.

Similar comparisons of predicted CO adsorption behavior with experimental CO adduct product distributions also provide evidence for assigning the ground state structures of the $M_5S_7^+$ and $M_6S_8^+$ clusters. The latter contain metallic cores with most of the sulfur atoms bonded along the edges or in the faces of the metal core structure. The metallic core structure of substoichiometric clusters like $M_5S_7^+$ and $M_6S_8^+$ has been attributed to partially filled d-orbitals on the metal atoms as well maximizing the number of sulfur binding sites at edges and faces. The latter maximize electronic interactions between the Mo-S atoms via d-s-p orbital hybridization.[19,20]

Experimentally, the most probable $M_xS_y^+(CO)_n$ adducts observed are those with $n \leq x$, i.e., a maximum of one CO molecule per metal site. As a general feature, the DFT calculations show that adding more than one CO molecule to a metal site causes considerable distortion of the cluster. In fact, the $M_2S_6^+$ and $M_3S_7^+$ (M = Mo, W) clusters are predicted to internally fragment when $n > x$, which may explain the absence of such adducts in the experimental product distributions despite having a lower total energy than the $n = x$ adduct. Similarly, the n = 6 and 7 adducts of $M_5S_7^+$ are predicted to be more stable than the $n = x = 5$ adduct, but only the $n = 6$ adduct is observed experimentally. The DFT calculations provide a possible explanation by showing that the $n = 7$ adduct undergoes internal bond breaking whereas the $n = 6$ framework is stable, albeit highly distorted. For the $M_6S_8^+$ cluster, the calculations predict that the two lowest energy isomers can bind to more than six

CO molecules without fragmentation, although the apparent binding energy drops significantly for adducts with $n > 6$. The ability to bind additional CO molecules is likely a reflection of the metallic nature of the M_6 core of the $M_6S_8^+$ cluster. Interestingly, the DFT calculations also show that the addition of four CO molecules to the $M_6S_8^+$ cluster can lead to isomerization of the lower symmetry isomer to the more symmetric "Chevrel" isomer.

Finally, we note that the calculated adsorption energies for the first CO molecule onto the $M_xS_y^+$ cluster cations with x = 2, 3 and 5 are very similar, with a value of ~1 eV for the Mo clusters and ~1.5 eV for the W clusters. Essentially the same adsorption energies were obtained in our earlier study of CO addition to the $Mo_4S_6^+$ and $W_4S_6^+$ "magic" clusters (M = Mo, W).[30] The $M_6S_8^+$ "Chevrel" clusters studied here show somewhat higher CO binding energies for both Mo (1.3 eV) and W (1.8 eV). These values can be compared with previous studies of CO bonding which have focused on larger 2-dimensional clusters (platelets) whose structure mimics bulk MoS_2.[94,96] Binding of CO only occurs at the edges of the platelets which can be either Mo or S terminated. These 2D clusters are used as models for the active catalytic species in hydrotreating catalysts, which are composed of small nanoplatelets of near-stoichiometric MoS_2. In their study of $Mo_{28}S_x$ (x = 48, 60, 84), Zeng, et. al, obtained a first CO binding energy of 1.2 eV at 4-coordinated and ~0.5 eV for 6-coordinated Mo edge sites[96]. For the near stoichiometric $Mo_{16}S_x$ (x = 29, 34, 38) clusters, the same group calculated a range of 1.1-1.3 eV for the first CO binding energies at 4-coordinated Mo edge sites (depending on exact geometry of metal site).[94] Near additivity of adsorption energy is also observed for multiple CO additions on the

large clusters, similar to what is predicted for the smaller $Mo_4S_6^+$, $Mo_5S_7^+$, and $Mo_6S_8^+$ clusters in this work. Despite the large variation in structure, the first CO bonding energies are remarkably similar between these larger bulk-like clusters and the small clusters studied here, even though the $Mo_4S_6^+$, $Mo_5S_7^+$, and $Mo_6S_8^+$ have metallic cores that are absent in bulk MoS_2. These results suggest that the metal-CO interaction is highly localized with the detailed structure of the surrounding cluster playing only a minor role. Since CO is known to bind to the same metal sites that are also active for catalysis, it is likely that that even the smaller clusters 3D clusters are active for promoting surface reactions. In particular, the high CO adsorption energies and high number of active sites (6) per unit volume make the $Mo_6S_8^+$ "Chevrel" cluster an interesting candidate as a supported nanocatalyst. Indeed, recent DFT calculations by Seifert, et al, have explored the binding of the Mo_6S_8 clusters on a Au(111) surface and have shown it to strongly bind to the Au surface with only minor structural changes[55,56].

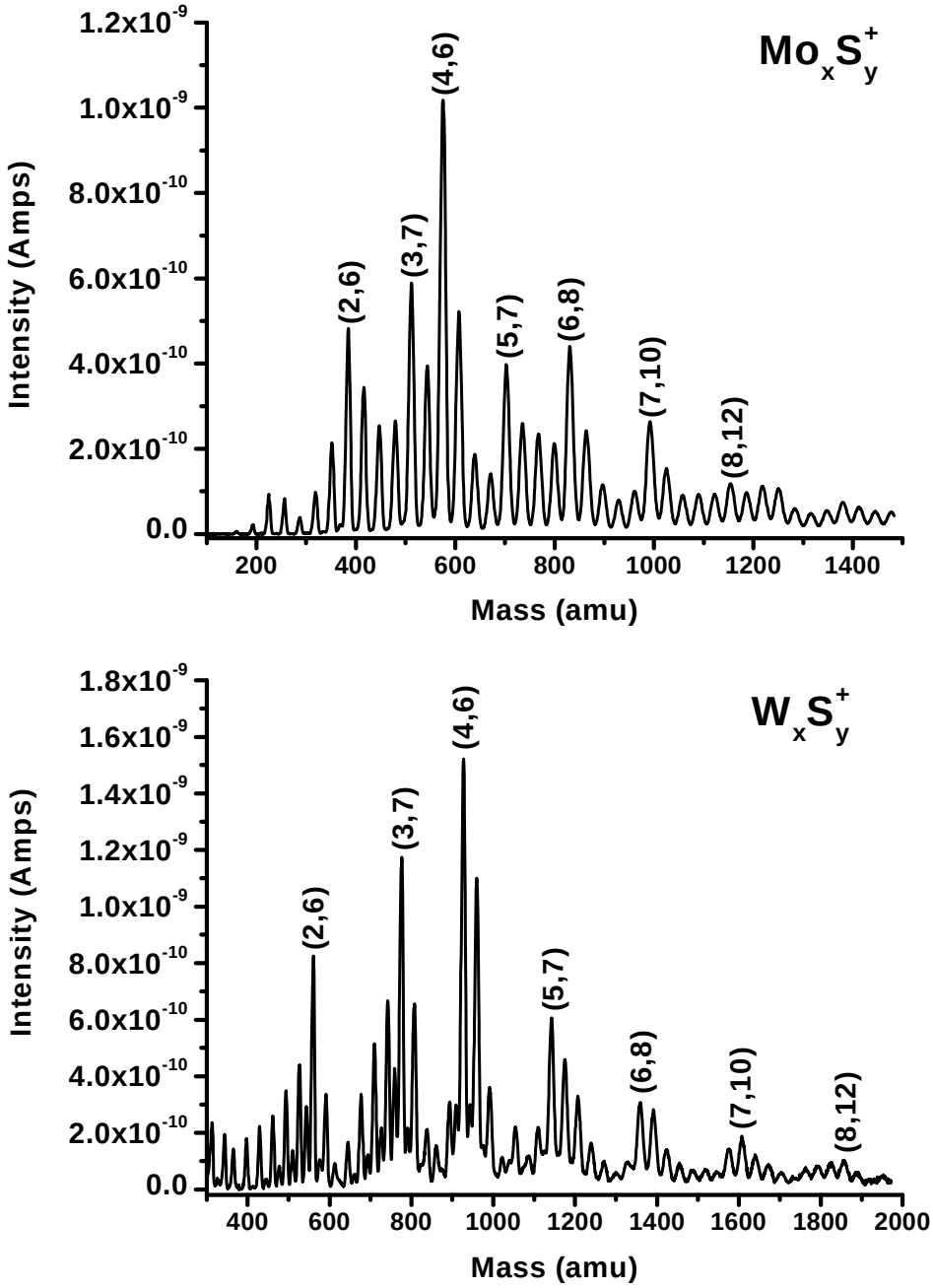

Figure 3.1: Mass spectra of $M_xS_y^+$ cluster ions (M = Mo, W) produced in a magnetron sputtering source. Small peaks between the consecutive sulfur atom peaks in the $W_xS_y^+$ mass spectrum are a result of a small oxygen contamination.

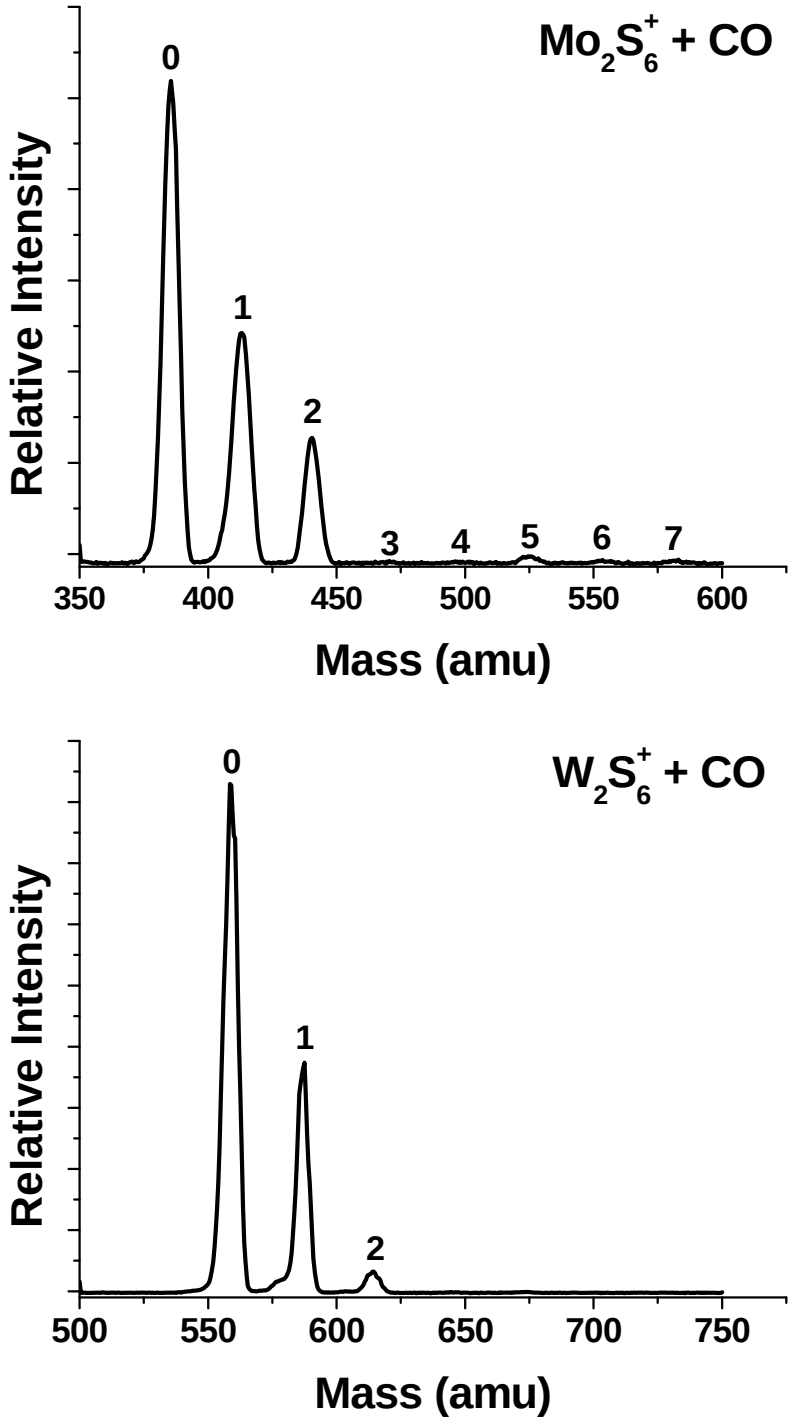

Figure 3.2: Mass spectra of products formed from collisions of the $M_2S_6^+$ (M = Mo, W) cluster with a 25% CO in He gas mixture.

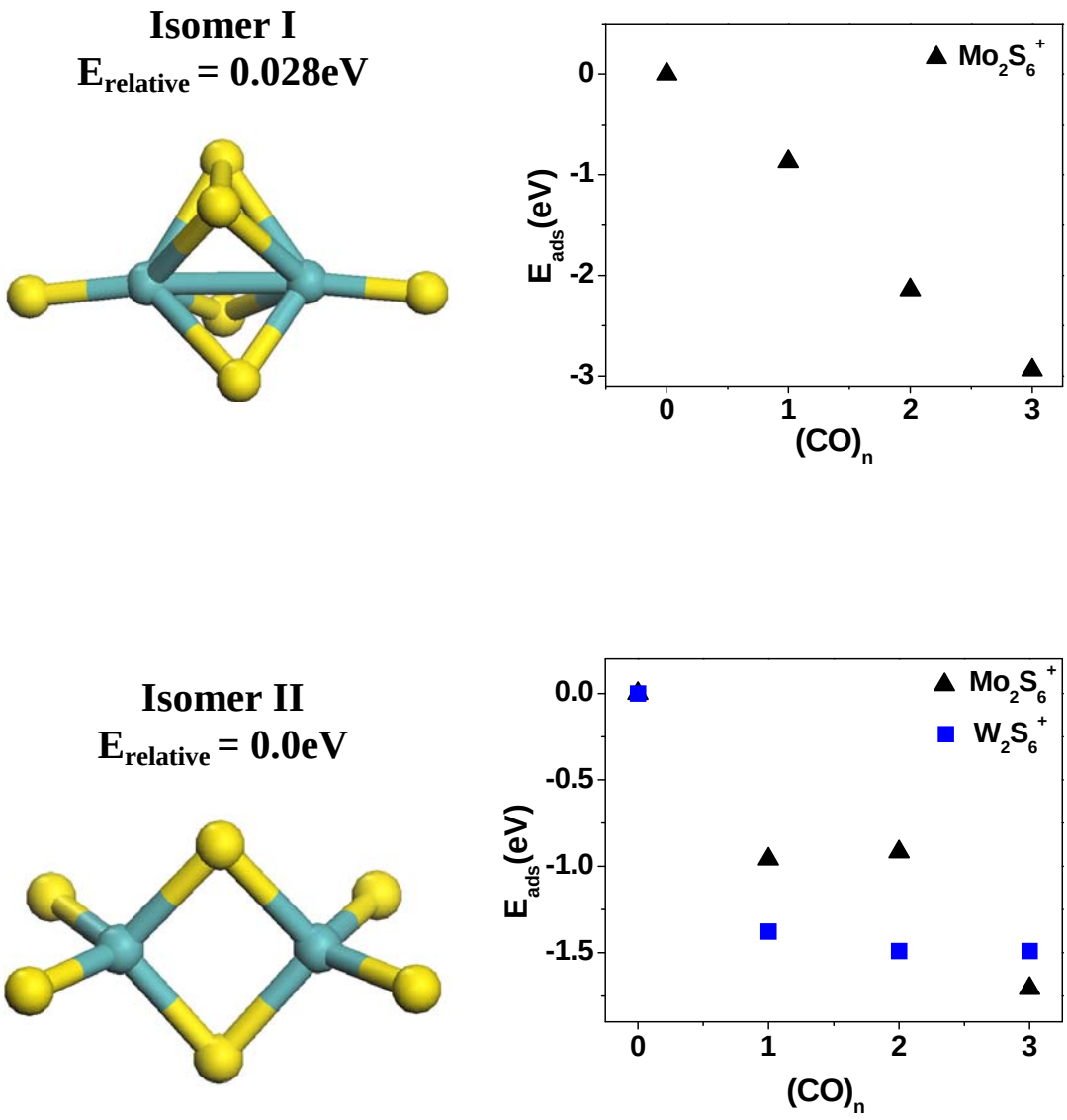

Figure 3.3: Optimized geometrical structures for the lowest energy isomers of the $M_2S_6^+$ cluster (M = Mo, W). Figures adjacent to each isomer show the total adsorption of CO molecules to the $M_2S_6^+$ clusters as determined by DFT calculations.

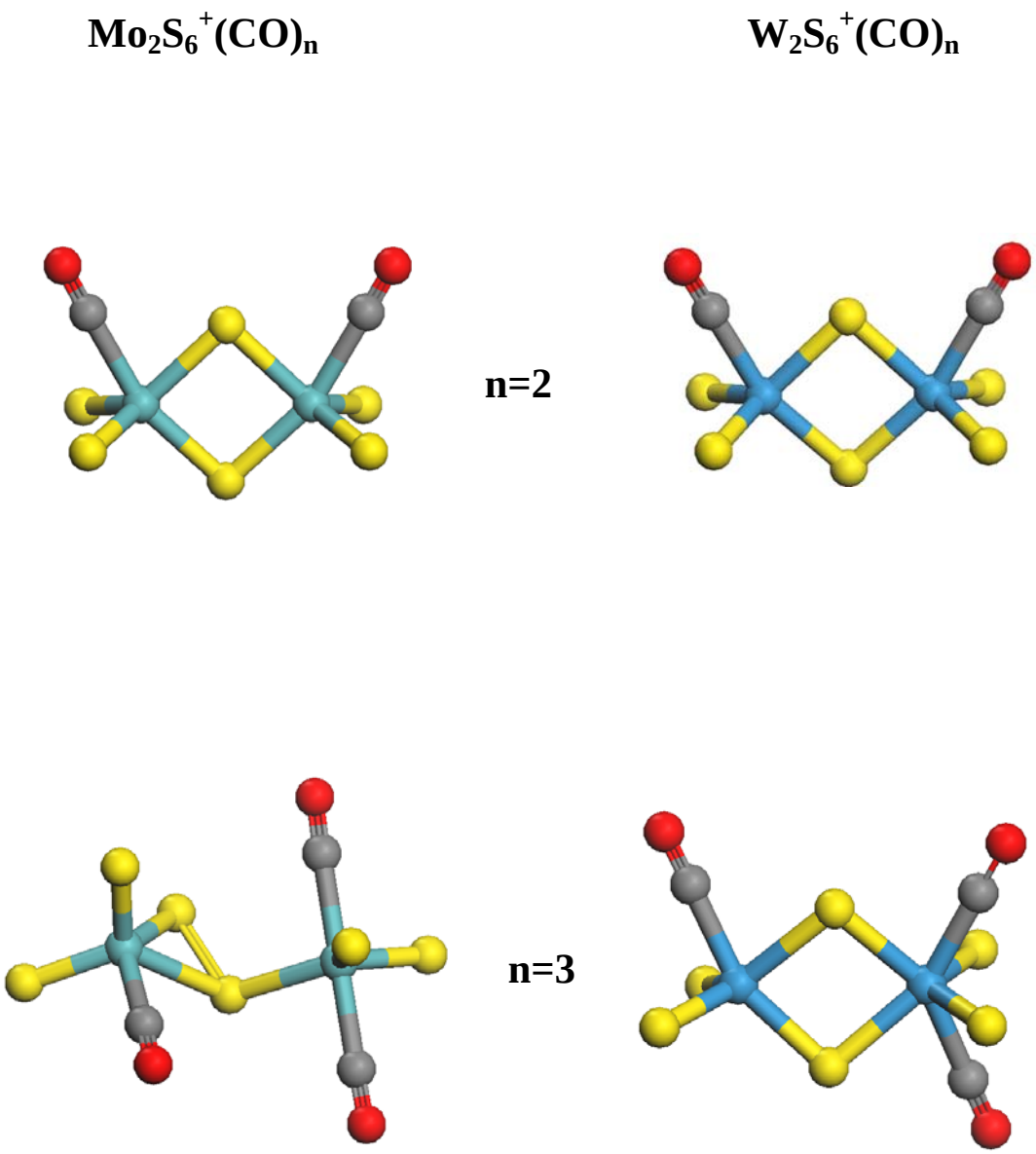

Figure 3.4: Geometry-optimized structures of the *n* = 2 and *n* = 3 CO adducts of isomer II of the $M_2S_6^+$ (M = Mo, W) clusters as determined from DFT calculations.

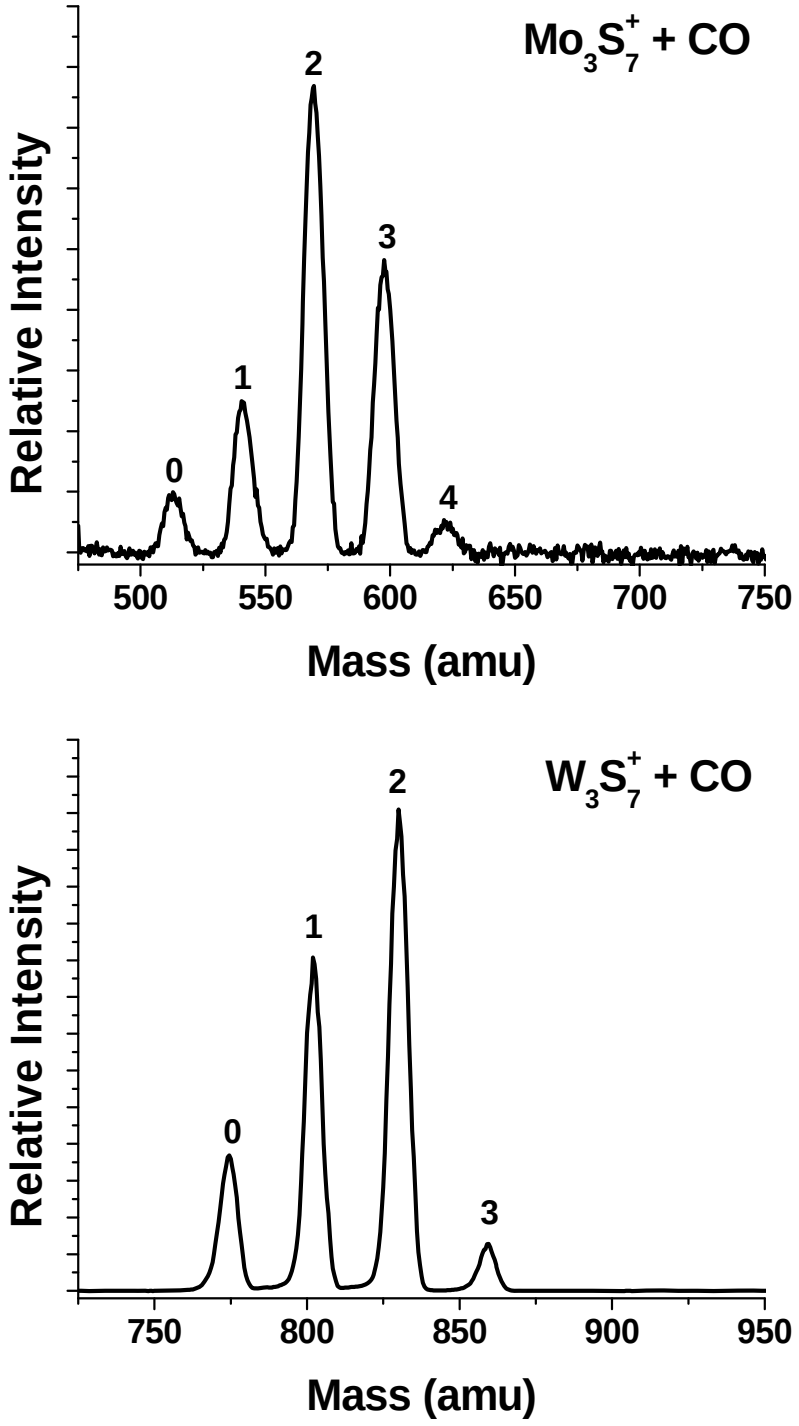

Figure 3.5: Mass spectra of products formed from the collisions of the $M_3S_7^+$ (M = Mo, W) cluster with a 25% CO in He gas mixture.

Isomer I
$E_{relative}$ = 2.01eV

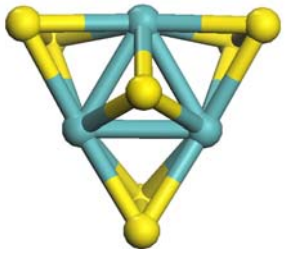

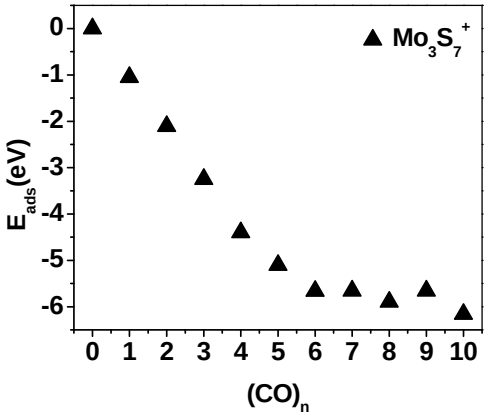

Isomer II
$E_{relative}$ = 0.078eV

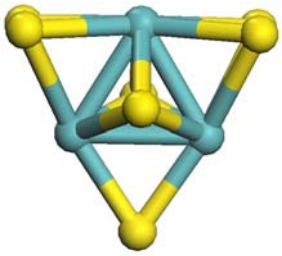

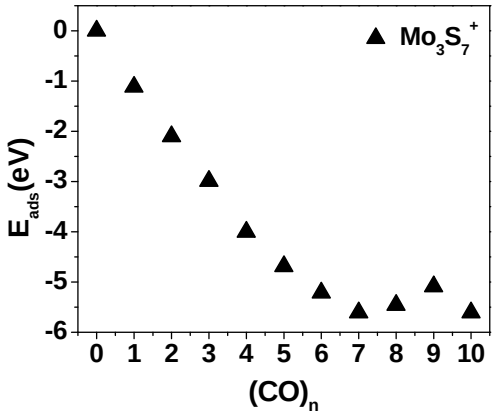

Isomer III
$E_{relative}$ = 0.0eV

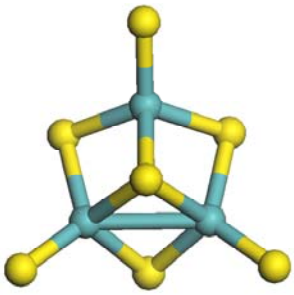

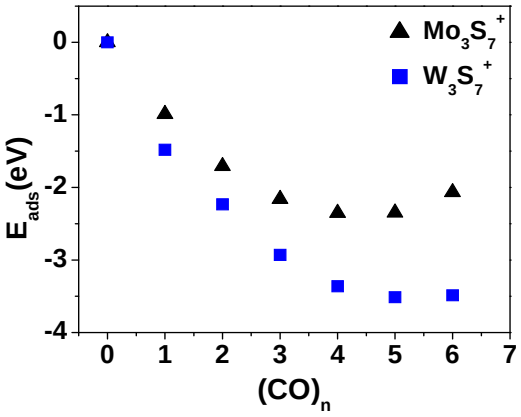

Figure 3.6: Optimized structures for the three lowest energy isomers of the $M_3S_7^+$ (M = Mo, W) clusters. Figures adjacent to each isomer show the total adsorption energies for sequential adsorption of CO molecules to the $M_3S_7^+$ clusters as determined by DFT calculations.

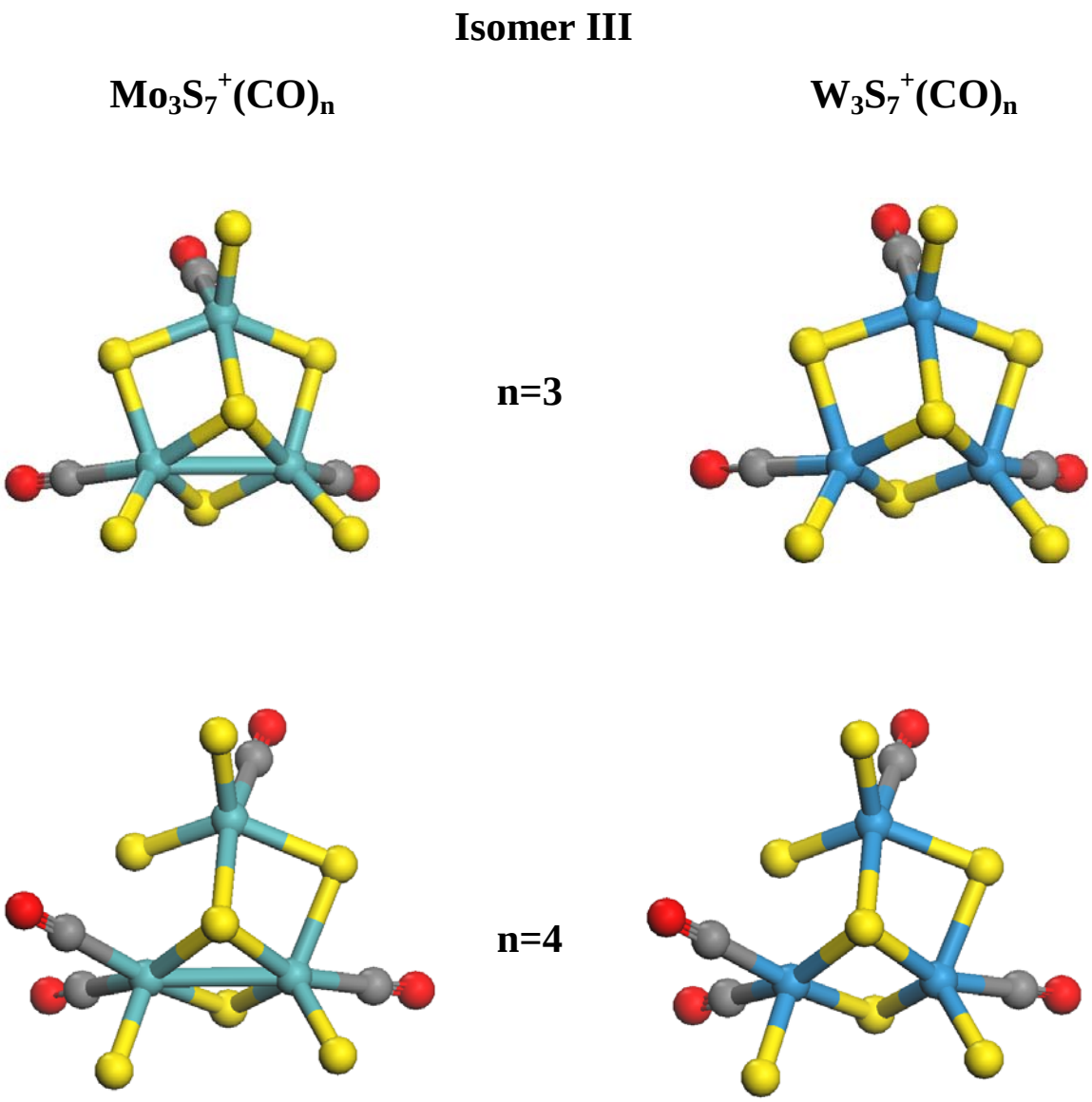

Figure 3.7: Geometry-optimized structure of the *n* = 3 and *n* = 4 CO adducts of isomer III of the $M_3S_7^+$ (M = Mo, W) clusters as determined by DFT calculations.

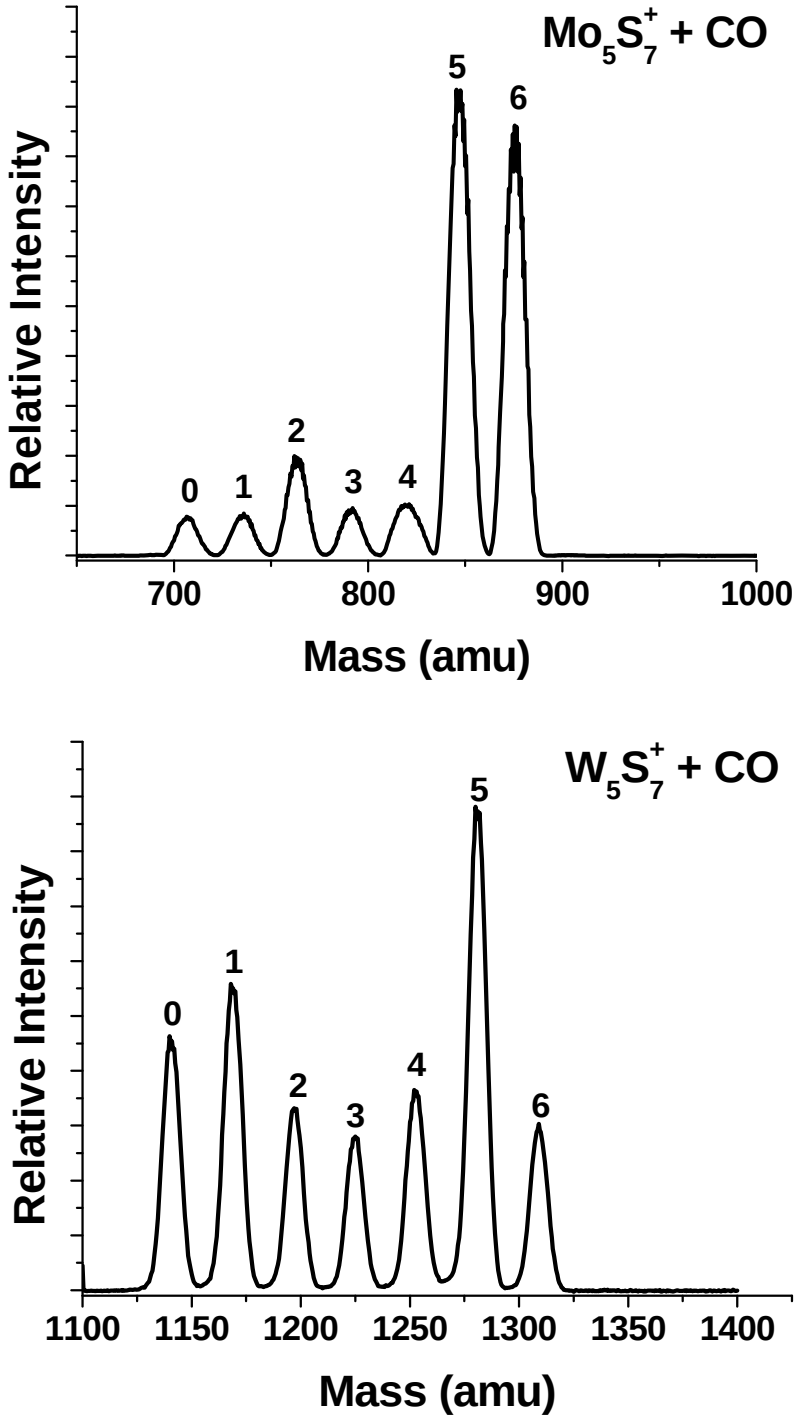

Figure 3.8: Mass spectra of products formed from collisions of the $M_5S_7^+$ (M = Mo, W) cluster with a 25% CO in He gas mixture.

Isomer I

$E_{relative}$ = 1.15 eV

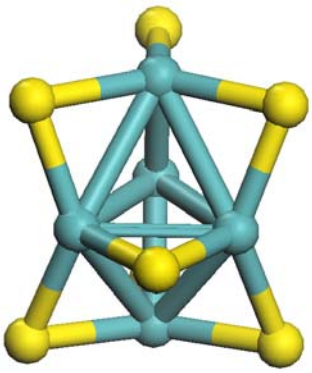

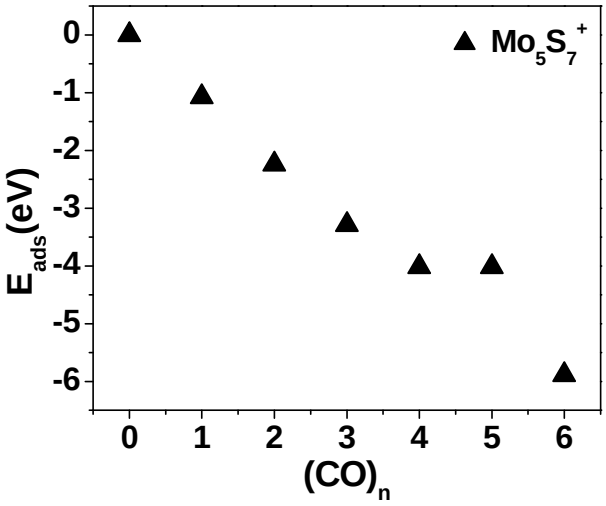

Isomer II

$E_{relative}$ = 0.0 eV

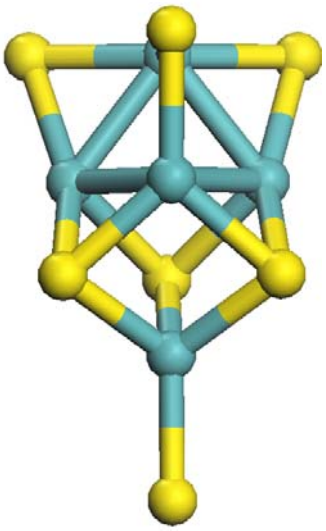

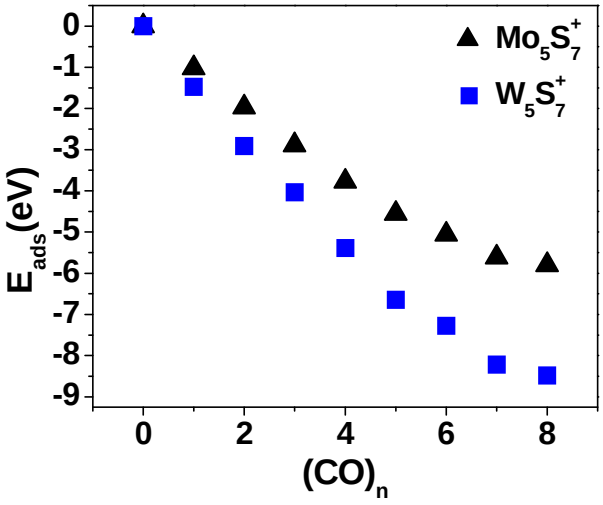

Figure 3.9: Optimized structures for the two lowest energy isomers of the $M_5S_7^+$ clusters (M = Mo, W). Figures adjacent to each isomer show the total adsorption energies for sequential adsorption of CO molecules to the $M_5S_7^+$ clusters as determined by DFT calculations.

Isomer II

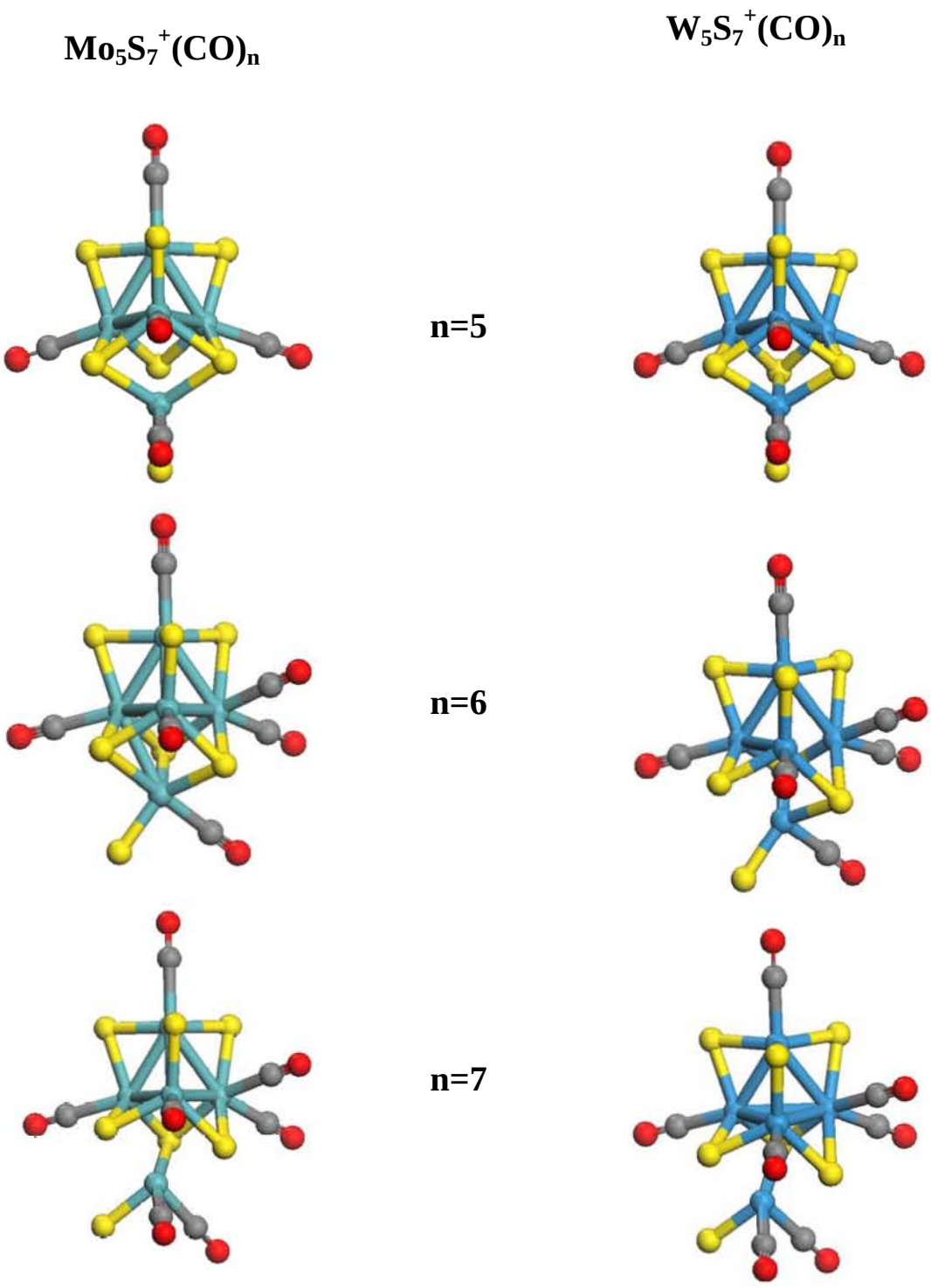

Figure 3.10: Geometry-optimized structures of the *n* = 5-7 CO adducts of isomer II of the $M_5S_7^+$ (M = Mo, W) clusters as determined by DFT calculations.

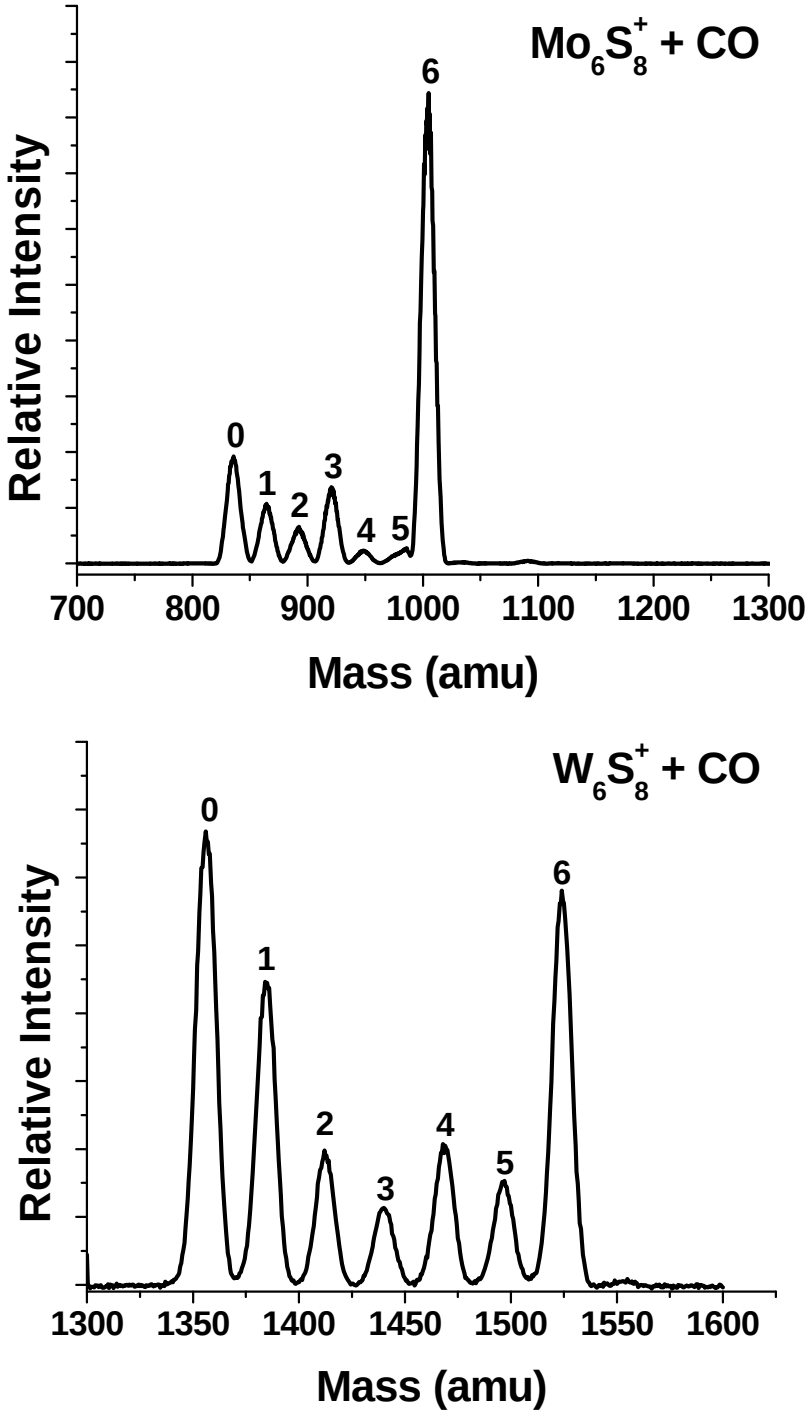

Figure 3.11: Mass spectra of products formed from collisions of $M_6S_8^+$ cluster with a 25% CO in He gas mixture.

Isomer I

Mo: $E_{relative}$ = 0.22 eV

W: $E_{relative}$ = 0.00 eV

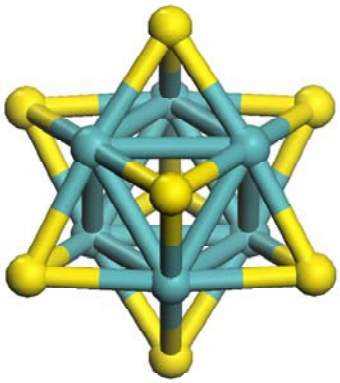

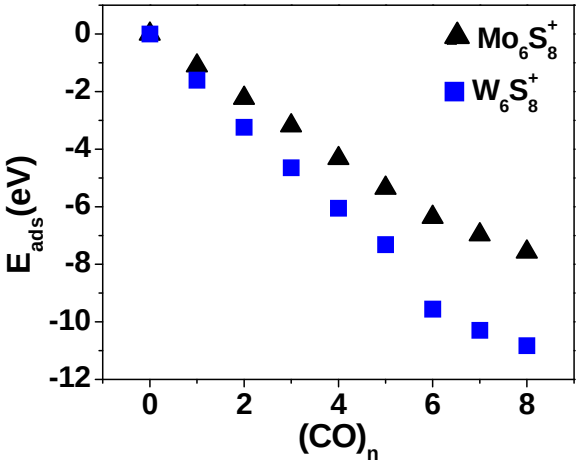

Isomer II

Mo: $E_{relative}$ = 0.00 eV

W: $E_{relative}$ = 0.25 eV

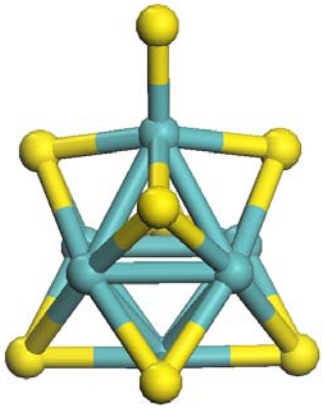

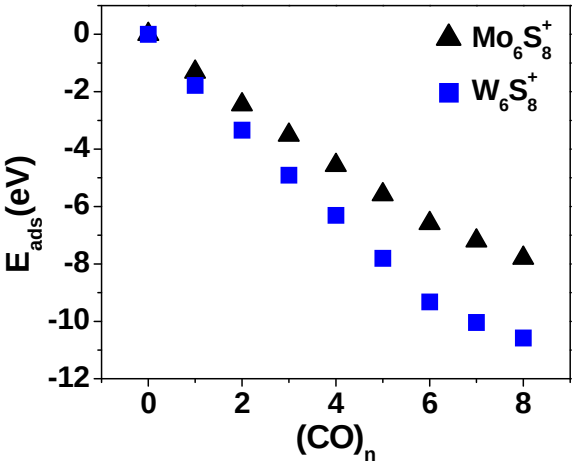

Figure 3.12: Optimized structures of the two lowest energy isomers of the $M_6S_8^+$ (M = Mo, W) clusters. Figures adjacent to each isomer show the total adsorption energies for sequential adsorption of CO molecules to the $M_6S_8^+$ clusters as determined by DFT calculations.

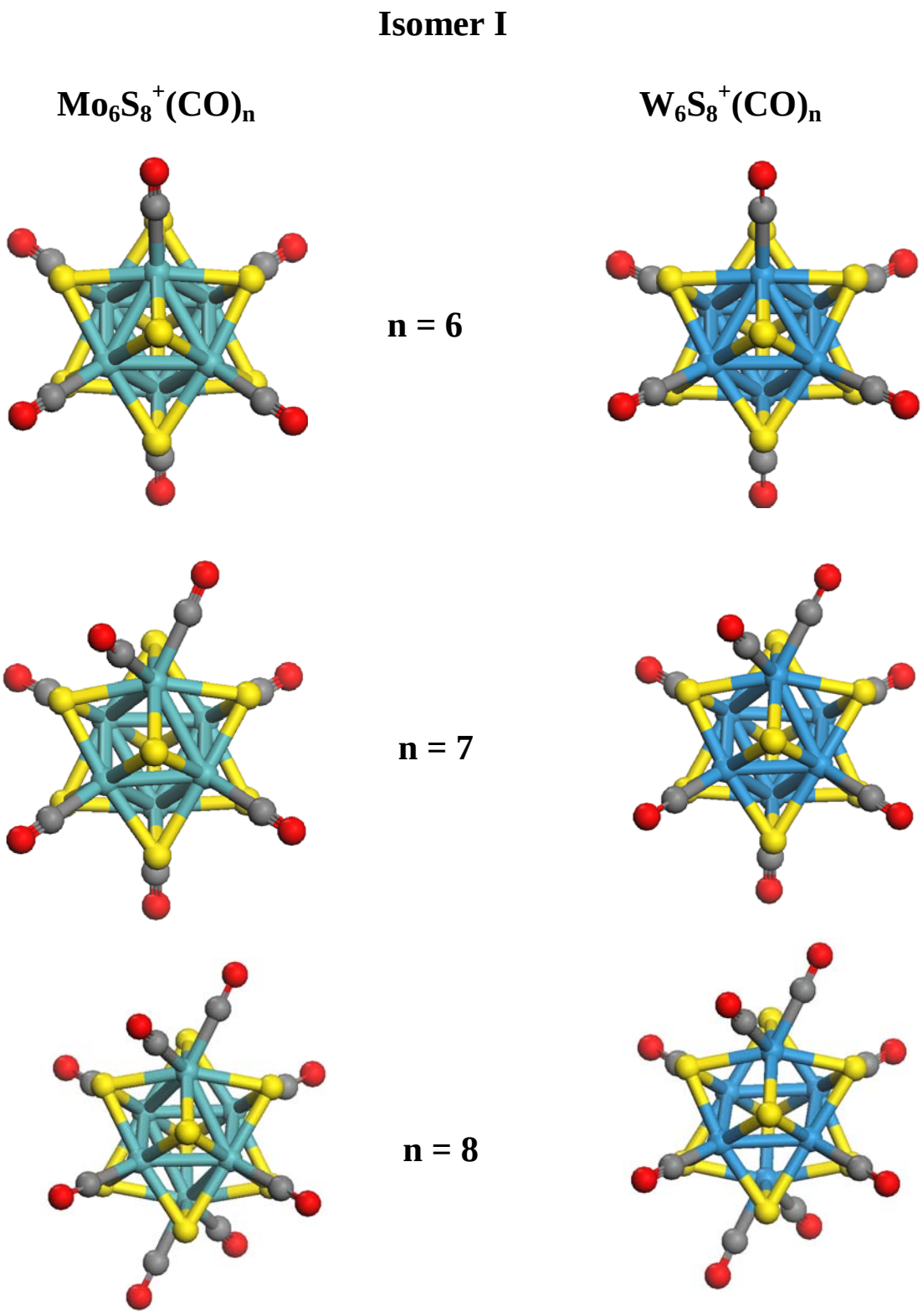

Figure 3.13: Geometry-optimized structures for the *n* = 6-8 CO adducts of isomer I of the $M_6S_8^+$ (M = Mo, W) clusters as determined from DFT calculations.

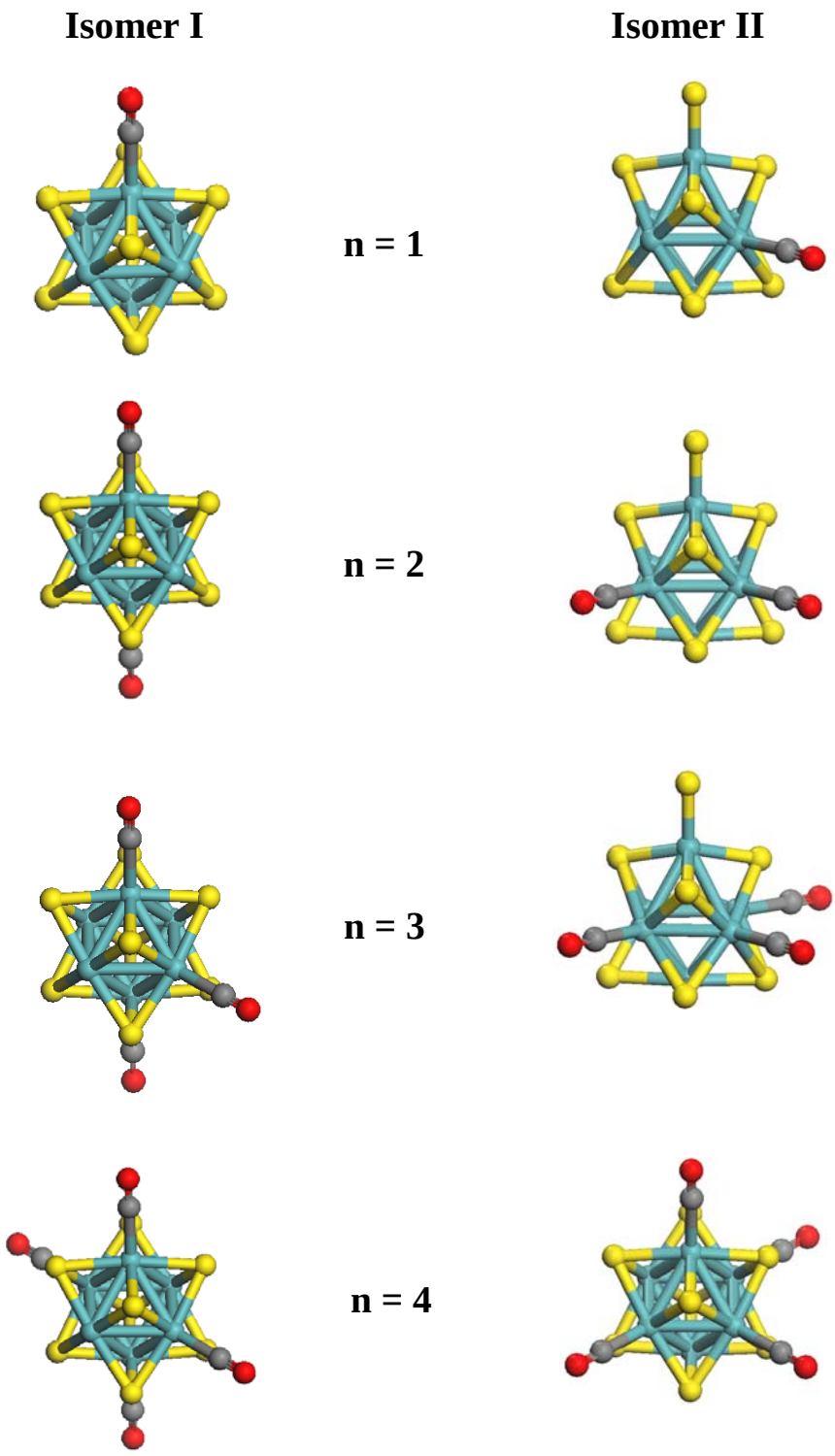

Figure 3.14: Comparison of the geometry optimized structures for CO adducts (*n* = 1-4) of isomers I and II of the $Mo_6S_8^+$ cluster as determined from DFT calculations.

n	$\Delta E_{ads}(n)$ $Mo_2S_6(CO)_n^+$	$\Delta E_{ads}(n)$ $W_2S_6(CO)_n^+$
1	-0.96	-1.38
2	+0.042	-0.11
3	-0.79	0.00

Table 3.1: Calculated binding energies, $\Delta E_{ads}(n)$, for the consecutive addition of *n*CO molecules to isomer II of the $M_2S_6^+$ cluster (M = Mo, W). All energies are given in eV.

n	ΔE_{ads}(n) $Mo_3S_7(CO)_n^+$	ΔE_{ads}(n) $W_3S_7(CO)_n^+$
1	-0.99	-1.48
2	-0.72	-0.75
3	-0.46	-0.70
4	-0.19	-0.43
5	+0.006	-0.15**
6	+0.28	+.026

Table 3.2: Calculated binding energies, $\Delta E_{ads}(n)$, for the consecutive addition of *n*CO molecules to isomer III of the $M_3S_7^+$ cluster (M = Mo, W). All energies are given in eV. ** Denotes breakage in the adduct cluster.

n	$\Delta E_{ads}(n)$ $Mo_5S_7(CO)_n^+$	$\Delta E_{ads}(n)$ $W_5S_7(CO)_n^+$
1	-1.02	-1.48
2	-0.95	-1.43
3	-0.92	-1.12
4	-0.88	-1.35
5	-0.78	-1.26
6	-0.52	-0.63
7	-0.56	-0.94
8	-0.18	-0.26

Table 3.3: Calculated binding energies, $\Delta E_{ads}(n)$, for the consecutive addition of *n*CO molecules to isomer II of the $M_5S_7^+$ cluster (M = Mo, W). All energies are given in eV.

	$\Delta E_{ads}(n)$ $Mo_6S_8(CO)_n^+$		$\Delta E_{ads}(n)$ $W_6S_8(CO)_n^+$	
n	Isomer I	Isomer II	Isomer I	Isomer II
1	-1.32	-1.10	-1.78	-1.60
2	-1.14	-1.12	-1.55	-1.64
3	-1.06	-0.96	-1.57	-1.40
4	-1.04	-0.95	-1.45	-1.41
5	-1.03	-0.86	-1.50	-1.26
6	-1.00	-1.38	-1.52	-2.24
7	-0.60	-0.60	-0.72	-0.73
8	-0.60	-0.60	-0.54	-0.54

Table 3.4: Calculated binding energies, $\Delta E_{ads}(n)$, for the consecutive addition of *n*CO molecules to the $M_6S_8^+$ cluster (M = Mo, W). All energies are given in eV.

Chapter 4. Size-Selected Deposition of $Mo_xS_y^+$ on Au(111)

4.1 Introduction

It is widely known that in its bulk form, molybdenum sulfide is an important catalyst for a wide range of heterogeneous reactions such as HDS, HYD, and HDN.[11,97,98] Typically, these catalysts consist of small MoS_2 nanoparticles dispersed on γ-Al_2O_3 with a Co or Ni metal promoter. Generally in these catalysts it has been accepted that the active sites for reactivity are the metal sites (Mo, Co, or Ni) that lie along the edges of the particles.[11,99] However, due to the inhomogeneity of industrial catalyst, information such as role of particle size, composition, and structure are difficult to determine. Because of this, it is desirable to prepare model catalysts under UHV conditions where surface science techniques can be used to probe such properties. Preparation of catalytically active materials on single crystal substrates allows for well defined systems to study characterization and reactivity through depositon of nanoclusters or casting of thin metal films.[44-47,57,100]

Besenbacher and coworkers used STM to study the structure of MoS_2 nanoclusters deposited on a Au(111) surface.[44-46,57,100] The nanoclusters were found to be single layer S-Mo-S islands that have triangular shapes and possess metallic states that appear in STM as a bright rim along the edge of the nanocluster.[100] As the size of the nanoclusters decrease (#Mo atoms $\leq$ 15), the S/Mo ratio decreases and the structure of the edge terminations is observed to change with an increasing tendency for the formation of S-vacancies. As a general feature, the size variations in the metal sulfide nanoclusters are associated with changes in morphology and electronic

structure that are highly dependent on the optimum metal-to-sulfur ratio for a given cluster size.

In this chapter, results will be presented on the size selected deposition of $Mo_xS_y^+$ (x/y: 3/7, 4/6, 5/7, 6/8, 7/10, 8/12) clusters supported on Au(111). Full characterization of one cluster in particular, Mo_6S_8 supported on Au(111), will also be presented in detail. The Mo_6S_8 cluster is widely known as the building block for the Chevrel phase of MoS_2.[59,60] Crystalline Chevrel phases and amorphous ternary molybdenum sulfides have been found to be active catalysts for methanethiol synthesis from methanol and H_2S as well as for HDS.[61] The most stable structure for the Mo_6S_8 cluster has been calculated via DFT in our laboratory (see chapter 3).[35,55] The cluster consists of an octahedral core of Mo atoms with eight face capping sulfur atoms and a point group assignment of O_h. This particular configuration leaves all six of the Mo atoms exposed for binding molecules such as CO which was demonstrated in gas phase collision studies in our laboratory.[35] The Au(111) surface was used as a support in this work and the Mo_6S_8/Au(111) system has been studied previously using DFT by Popov et.al.[55,56] The authors showed that the Mo_6S_8 cluster remains intact when bonded onto the Au(111) surface and assumes a square bridge orientation with a binding energy of -1.69eV. In our laboratory, we have calculated the supported cluster and the lowest energy configuration is also the square bridge position with a binding energy of -1.79eV, which is comparable to the value reported by Popov et. al.

In this work the $Mo_xS_y^+$ clusters were deposited via size-selected deposition using a magnetron sputtering source described in Chapter 2. A variety of $Mo_xS_y^+$ cation clusters are generated and mass selected by a quadrupole mass spectrometer

before soft landing on the Au(111) surface all under UHV conditions. Here we use cluster deposition because of its advantage of producing a monodisperse distribution of clusters while also being able to control cluster coverage. Conventional surface science techniques such as AES, UPS, and TPD can be used on the as-deposited clusters. TPD and Auger electron spectroscopy show that clusters behave as independent entities up to coverages of ~0.15 ML, beyond which the clusters seem to aggregate on the surface. Temperature programmed desorption spectra of ^{13}CO exhibit near first-order coverage dependence with a peak temperatures between ~240-293K for the different clusters. Annealing of the as-deposited clusters resulted in a significant decrease in the CO adsorption intensity and for all except Mo_3S_7, a low temperature contribution appears once the surface is perturbed at ~240K. This CO desorption peak is attributed to the formation of amorphous Mo_xS_y moieties formed on the surface as the clusters are annealed. Further annealing showed a significant decrease in the CO desorption signal reinforcing the loss of active metal sites and agglomeration of the clusters on the Au substrate. The Mo_6S_8 cluster exhibits the most prominent ^{13}CO desorption spectra, indicating its stability on the surface. As a result, the Mo_6S_8 was used for further investigations with regards to cluster coverage and stability on the Au surface.

4.2 Experimental

The experiments in this chapter were performed using a cluster deposition apparatus that has been described in detail elsewhere[32,33] and brief descriptions of the components can be viewed in Chapter 2. Briefly, $Mo_xS_y^+$ clusters were produced by a magnetron sputtering source using a molybdenum target and a sputtering gas of 4%

H_2S in Ar. Both the sputtering and aggregation gases are introduced into the source using variable leak valves with typical backing pressures of 12.0 Torr (4% H_2S/Ar) and 30 Torr (He). The magnetron was operated at a power of ~217 watts. The length of the high-pressure He region between the metal target and first exit aperture (cluster condensation region) for Mo-sulfide was 2.0 inches. The $Mo_xS_y^+$ cluster ions produced by the source were then guided through a region of differential pumping using a quadrupole ion guide and followed by a quadrupole mass spectrometer which selects a specific cluster mass by its mass-to-charge ratio. The resulting mass-selected cluster beam was guided into the lower level of a UHV chamber using a hexapole ion guide. To prevent the deposition of neutral species, the mass-selected ions are deflected by a 90^o quadrupole bender which is mounted at the exit of the hexapole ion guide. A Faraday cup, mounted on a linear drive, is used to monitor the cluster ion intensity.

The Au (111) single crystal (10mm × 2mm) was mounted on two tantalum posts (1.0 mm diameter) that were suspended from an XYZ manipulator via a UHV feedthrough. The posts can be resistively heated and are in thermal contact with a liquid nitrogen bath. A type-K thermocouple wire was attached to the back side of the crystal in order to monitor the temperature. The Au (111) surface was cleaned by repeated cycles of Ar^+ sputtering for 30 minutes at room temperature (two cycles at 1 keV, 4μA and one cycle at 0.5 keV, 1.75 μA) followed by annealing at 800K for 10 minutes.

The kinetic energy distribution of the $Mo_xS_y^+$ clusters were measured by applying a voltage ramp to the Faraday cup while monitoring the ion current of the

cluster.[101,102] The resulting spectrum was differentiated and fit to a near Gaussian distribution with an average kinetic energy of ~1.3-2.2 eV and a full width at half-maximum of ~2.4-3.3eV. These energy distributions correspond to "soft landing" as the average kinetic energy per atom is ≤0.1-0.2 eV.[103,104] The final lens element prior to deposition on the crystal is held at ground potential so that there is no change in the kinetic energy distribution from when the clusters are formed in the magnetron source. The distance between the quadrupole bender and the crystal was ~1.5-2mm. The deposition occurs in an ultra-high vacuum (UHV) chamber with typical pressures of ~ 1×10^{-9} torr and was done at room temperature with typical ion currents are ~0.75-2.0×10^{-9} amps.

A computer program (LabView) was used to control the cluster coverage via measurements of the ion current on the sample. The cluster coverage was determined by multiplying the total number of ions deposited (0.44 - 4.4×10^{13} ions) by the estimated area per cluster and dividing by the experimentally determined deposition area. The cluster area was estimated assuming a circular cross section using the centroid radius (~3 Å) derived from the DFT calculated structure for the isolated cluster (neutral).[35] The deposition area was obtained from Auger "line scans" where the intensity of the sulfur (152 eV) Auger peak originating from the deposited clusters was measured as a function of distance from the center of the crystal. The size of the Auger electron beam under our operating conditions (≤ 0.2 mm) is significantly smaller than the measured deposition area, thereby allowing reasonably precise measurements. The distribution is somewhat wider in the plane of the 90° beam deflection as a result of velocity dispersion in the electrostatic field of the quadrupole

bender. The deposition area containing 95% of the clusters could be approximated by an ellipse with an area of 23 mm^2. Using these quantities, the cluster coverage probed in this work ranged from 0.05 ML to 0.5 ML.

The bare Au(111) surface as well as the Mo_6S_8/Au(111) surface was probed by AES, UPS, and TPD. Electron energy analysis was performed by a hemispherical energy analyzer with a 100 mm mean radius. A 5 KeV electron beam was used to excite the Au (MNN; 74 eV), S(LMM; 153 eV) and Mo (MNN; 190 eV) Auger transitions. The valence bands of the surface were probed using a differentially-pumped, hollow-cathode discharge lamp using He gas to produce 21.22 eV photons (HeI transition).

Temperature programmed desorption of ^{13}CO were used to probe the exposed Mo metal sites of the deposited clusters. A quadrupole mass spectrometer utilizing a cryogenically-cooled shroud was used to ionize and detect desorbed molecules form the surface. Isotopically labeled ^{13}CO (m/e = 29; Cambridge Isotopes) was used to avoid interference from background CO (m/e = 28) in the vacuum chamber. The Mo_6S_8/Au(111) surface was typically dosed at 200 K to minimize ^{13}CO desorption signal from defect sites on the Au(111) crystal between 170 K and 200 K. After cooling to 145 K, TPD spectra were recorded by ramping the surface temperature at a rate of 2K/sec.

4.2.1 Computational Details

Computational details for the geometric calculations which gave HOMO-LUMO gap information for the cation clusters has been described in Chapter 3, Section 3.2.1. Additional calculations in this chapter were done on the Mo_6S_8 cluster

using periodic density function theory (DFT) calculations with the projector-augmented wave (PAW)[105] method were carried out for all calculations, as implemented in the Vienna *ab initio* simulation package (VASP).[106,107] The generalized gradient approximation (GGA) with the Perdew-Burke-Ernzerhof (PBE) exchange-correlation functional[108] was used. The kinetic energy cutoff for a plane wave basis set was 400 eV. We applied a Monkhorst-Pack mesh[109] with (3×3×3) and (3×3×1) **k**-points for bulk and surface calculations, respectively, allowing convergence to 0.01 eV of the total electronic energy. For the 2-D slab model calculations, the Au(111) metal surfaces comprised of three atomic layers were separated by a vacuum space equivalent to four layers (~23 Å) in the direction perpendicular to the surface. Only the top most layer of the Au(111) surface was relaxed, the bottom two layers were fixed.

The binding energy of the Mo_6S_8 on the Au(111) surface was calculated from the following expression:

$$\Delta E_{ads} = E(Mo_6S_8/Au) - E(Mo_6S_8) - E(Au) \qquad (4.1)$$

Similarly, the total adsorption energy of CO bound to the supported cluster was calculated from the following:

$$E_{ads} = E(n\mathrm{CO}/Mo_6S_8/Au) - E(Mo_6S_8/Au) - E(n\mathrm{CO}) \qquad (4.2)$$

The binding energy for the sequenctial addition of CO onto the supported cluster was determined using the following equation:

$$\Delta E_{ads}(n) = E_{ads}(n) - E_{ads}(n\text{-}1) \qquad (4.3)$$

The effective coverage of the deposited clusters in the calculations is ~0.1 ML as estimated from the area of the base of the cluster divided by the total area of the Au(111) surface used.

4.3 Results and Discussion

4.3.1 $Mo_xS_y^+$ on Au(111)

A range of $Mo_xS_y^+$ clusters were deposited on the Au(111) surface and a TPD spectrum for the desorption of ^{13}CO for each of the clusters is compared in Figure 4.1. The adsorption of CO has proven to be a good probe of available metal sites in previous studies and the strength of the CO-Mo bond has be shown to correlate with binding energies seen in systems used as hydrodesulfurization catalyst. The binding energy for CO was calculated using a Redhead analysis (equation 2.6) with estimations given in Chapter 2.

The smallest cluster to be deposited on the Au surface is the Mo_3S_7. The black trace in Figure 4.1 shows the CO desorption peak at a temperature of 240K, which corresponds to desorption energy of ~0.70eV using equation 2.6. In Chapter 3, it was found that the lowest energy configuration for the Mo_3S_7 cluster was an open structure that possessed one long metal-metal bond and several dangling sulfur bonds. The calculated HOMO-LUMO gap for the free cluster is 1.41eV and therefore, in comparison the other clusters, it is the least stable as can be seen in Figure 4.2. It may be possible that the small cluster does not maintain structural integrity once it is deposited onto the surface. This would not be a consequence of high energy landing as the kinetic energy profiles show an energy distribution of ~0.15 eV/atom which is still consistent with soft-landing. It may be possible that as a result of the dangling

sulfur bonds found in the lowest energy structure, binding onto the surface may not be stable. Bond breakage between the molybdenum and sulfur atoms may occur due to strong Au-S interactions resulting in amorphous species on the surface that have no real structural integrity. This will be discussed further in the next section when each of the clusters is analyzed for their thermal stability.

The magic cluster Mo_4S_6 has been studied previously in our laboratory[33] and will be shown here for comparison. The desorption temperature for ^{13}CO occurs at a peak maximum of 270K that correlates to a CO binding energy of ~0.77eV. This cluster has been thought to be unusually stable as a consequence of its large HOMO-LUMO gap of 2.91eV.[21,41] The $Mo_4S_6^+$ cluster is the most prominent peak in our mass spectrum (Figure 3.1) and is consistent with high stability. Its cage-like structure (internal metal tetrahedral core with edge sharing sulfur atoms) adds to its unique stability (see Figure 4.2). The rigid nature of the Mo_4S_6 geometry allows it to stay structurally intact when binding onto the Au substrate as suggested by previous DFT studies in which the cluster is only slightly distorted when bound to the Au surface.[33,54]

The Mo_5S_7 was the next to be examined and it was shown to be a structural adaptation of the Mo_4S_6, with the addition of one metal and one sulfur atom. The CO desorption peak (blue trace Figure 4.1) is very broad in nature with a FWHM of 92K. This suggests that there are a variety of different CO binding sites once the cluster is deposited onto the surface. The calculated HOMO-LUMO gap, 1.47eV is similar to that of the Mo_3S_7 (Figure 4.2) and is likely to be less stable in comparison to the other

clusters. This may be the result of the dangling sulfur bond which is similar to that of the Mo_3S_7.

The Mo_6S_8 is comprised of an octahedral core of Mo atoms and face capping S atoms as described in the previous chapter. The CO desorption intensity is higher than any of the other clusters with a maximum temperature of 288K which corresponds to a CO adsorption energy of ~0.83eV. Previous calculations on this cluster have shown it to retain its geometry on the surface and more details on its characterization will be addressed in the following sections.[55,56]

The two largest clusters that were deposited on the Au surface are the Mo_7S_{10} and the Mo_8S_{12} clusters. In the previous gas phase studies, we were unable to determine conclusively the lowest energy structure for the Mo_7S_{10} cluster based on CO collision studies and the Mo_8S_{12} was never evaluated due to its low ion beam intensity. However, based on their CO TPD peak profiles, some observations can be made for possible low energy structures for each of these clusters.

In Figure 4.3a, there is a comparison for the CO TPD profile for the Mo_6S_8 cluster and the Mo_7S_{10}. They each have a FWHM of ~ 51K and hold the highest CO binding energies at ~0.83eV and ~0.80eV, respectively. The desorption temperature for ^{13}CO is slightly lower for the Mo_7S_{10} cluster at 277K in comparison to 288K for the Mo_6S_8. Despite the difference, the peak shapes are very similar and may suggest a similarity in Mo binding sites. It has been shown previously that the larger clusters may be formed by the addition of Mo and S atoms to the more stable cage like structures (i.e. $Mo_4S_6 \rightarrow Mo_5S_7$). Therefore, it is likely that the Mo_7S_{10} has structural similarities to the more stable octahedral Mo_6S_8. Gas phase collision studies suggest

that the addition of a MoS_2 unit will make two Mo sites unfavorable for adsorption. Collision studies Mo_7S_{10} cluster and CO shows the most stable adduct to be the n=5 configuration with only weak binding up to n=7.

Figure 4.3b shows the TPD spectra for ^{13}CO on the Mo_4S_6 and the Mo_8S_{12} clusters. A rather remarkable observation is that both TPD profiles are nearly identical. One possible explanation is that the Mo_8S_{12} is actually a dimer of the Mo_4S_6 cluster. It has been reported that non-stoichiometric nanoplate formation can occur from these smaller clusters as well as self assembly on the surface.[57] The Mo_4S_6 cluster exhibits trigonal symmetry similar to larger $Mo_{21}S_{48}$ structures observed experimentally.[57,110] These platelets are sulfur rich in nature without the observation of any dangling sulfur bonds consistent with the dimer presented. Self assembly and ordered arrays of Mo_xS_y units are not uncommon and may be building blocks for unusually stable sulfur rich phases such as the Chevrel phase of the Mo_6S_8 cluster.

As a general feature, it is likely that the structure stability of the clusters prior to deposition is a good indication of its stability on the Au(111) surface and its ability for adsorption of CO. Figure 4.4 shows the calculated CO binding energy for the different clusters on the surface, the error bars denoted are the peak widths of desorption signal. This helps to point out the binding energy distribution resulting from different adsorption sites that are possible for a given cluster on the surface.

4.3.2 Thermal Stability of the Mo_xS_y on Au(111)

The thermal stability of the Mo_xS_y clusters on Au(111) was examined using desorption studies of ^{13}CO on the surface. Figure 4.5-4.7 shows the ^{13}CO TPD

spectra for each of the deposited clusters as a function of substrate annealing temperature. Each series of spectra shows that the surface undergoes morphological changes as probed by decreases in CO uptake intensity as well as changes in TPD peak shape. The most notable feature is the decline of the ^{13}CO signal intensity as a consequence of annealing, indicating that the number of available metal sites for binding has decreased. This observation is consistent with the formation of larger nanoparticles and or amorphous agglomerates on the Au(111) surface. For all of the clusters except the Mo_3S_7, as the surface is heated up, a low temperature shoulder arises at ~240K, with the majority of the TPD signal still coming from the main high temperature contribution. This indicates that there are still Mo sites that are similar in chemical nature to the parent structure that was deposited on the surface and we attribute the low temperature feature to desorption from amorphous Mo_xS_y species. The diffusion of the clusters is thermally activated at temperatures slightly above room temperature as the low temperature feature occurs generally at ~400K. It is interesting to note that the initial desorption temperature for the Mo_3S_7 occurs at 240K and does not shift during annealing cycles. Therefore, we conclude that the Mo_3S_7 is deposited on the surface in an amorphous phase similar to that of the annealed clusters. Examining the cluster structure (Figure 3.6 Isomer III), it is not too surprising that such a geometric configuration would not survive deposition on the surface.

In the specific case of Mo_6S_8 previous DFT studies as well as our own DFT studies have shown that the square bridge position is the most favorable binding configuration for the cluster on Au (111) with an energy of -1.79eV. However,

because of the incommensurate nature of the binding between the quasi-cubic Mo_6S_8 cluster and the hexagonally packed Au surface, several other binding configurations are nearly degenerate in energy (within 0.1-0.2 eV).[55] The different binding sites give rise to a low barrier for diffusion promoting mobilization once the surface is thermally activated.

The possibility of desorption of the clusters into the gas phase as well as encapsulation by Au atoms were examined via pre and post annealing AES studies. It has been shown that Au-atom encapsulation can occur on deposited materials on Au(111) as a consequence of the high mobility of Au adatoms on the surface. Thermally induced encapsulation by Au adatoms has been observed in previous studies of both Mo metal[50,111] and MoC_x[52] deposited on Au(111) as a result of the lower surface free energy of Au relative to Mo metal. The addition of sulfur, however, has been shown to inhibit encapsulation of Mo by Au.[50,111] When analyzing the AES spectra, the Au:Mo and Au:S Auger signal ratio did not change indicating that the loss of CO uptake at higher temperature is not due to site blocking by Au atoms.

4.3.3 Mo_6S_8 on Au(111): Theory of Cluster on Surface

In light of the stability of the Mo_6S_8 cluster as indicated by its relatively large HOMO-LUMO gap (1.99eV) and CO binding energy, a more comprehensive study was performed on this cluster beginning with theoretical results as to the nature of the binding on the surface. The structure of the free Mo_6S_8 cluster and the supported cluster on Au(111) as calculated by VASP can be seen in Figure 4.8. The unsupported Mo_6S_8 cluster (Figure 4.8a) consists of an octahedral core of Mo atoms

with a Mo-Mo bond length of 2.62Å and a Mo-S bond length of 2.44Å giving it an overall symmetry near O_h with fine tolerances (within 0.01Å). Imposing more strict tolerances (within .001Å) lowers the symmetry of the cluster to $C_{i.}$ Once bound to the surface in a square bridge position, the octahedral core of the cluster remains unaffected as the Mo-Mo bond length changes only slightly to a value of 2.64Å. The Mo-S bonds closest to the Au(111) surface displays a slight elongation to 2.50Å at the base of the cluster while the Mo-S bonds at the top of the cluster experience a slight contraction to 2.40Å. These relatively small distortions in the supported cluster are accompanied by a slight tilt in the final adsorption configuration that breaks the local symmetry to $C_{1.}$ This particular binding configuration (Figure 4.8b) gives an energy of -1.79eV with a Mo-Au bond length of ~2.90 Å and Au-S bonds having a range between 2.60-2.95Å. There is little overall charge transfer between the cluster and the Au(111) surface. The Mo_6S_8 becomes less negative with an overall charge transfer of 0.04e while the Au(111) surface becomes more negative with a charge transfer of -0.04e. In fact, this small electron transfer seems to only affect the local sulfur atoms as both the Mo top and side sites retain a mulliken charge of -1.41e and -1.21e respectively from the gas phase to the surface. The predicted charge density differences are very small and should have little effect in the reactivity of the cluster on the surface. This, however, is in stark contrast to previously investigated small magic cluster, Mo_4S_6 supported on Au(111). [33] In this study an electron transfer of -0.23e to the Mo top site was found and a -0.36e charge transfer for the Mo side site. The sulfur atoms also saw considerable redistribution of charges with a +0.23e transfer for the sulfur top site and a +0.32 transfer for the sulfur atoms bound to Au.

Qualitatively, it may be that because of the much higher binding energy predicted for the Mo_4S_6 (4.2eV) than the Mo_6S_8 (1.79eV) on Au, the charge transfer (interaction) with the surface is greater.

4.3.4 Mo_6S_8 on Au(111): Cluster Coverage Dependence

The $Mo_6S_8^+$ clusters were deposited with coverages between 0.05 and 0.5ML. For every cluster coverage an Auger spectrum was taken to measure relative surface concentrations of Au, S, and Mo atoms. A typical AES spectrum for a 0.4ML coverage can be seen in Figure 4.9. The raw AES signal was first smoothed and the first derivative was taken to highlight the regions of interest. In this case we display the Au(MNN) line at 74eV, the S(LMM) line at 153eV, and the Mo(MNN) line at 190eV. The peak areas can then be used to analyze the Au to S ratio as a function of cluster coverage. The beam from the electron gun is small in size, $\leq$ 0.2mm in diameter, relative to the actual deposition area (23 mm^2) and so we are confident that the Auger signal only corresponds to those within this region.

The coverage dependence of the Au:S peak ratio for Mo_6S_8 deposited on Au(111) is shown in Figure 4.10. As the cluster coverage increases, the Au:S ratio drops very rapidly but does not go completely to zero. Previous studies on a smaller Mo_4S_6 cluster in our laboratory show that the residual signal is likely a result of incomplete attenuation of the Au Auger electrons by the adsorbed clusters.[33] Multilayer formation was considered as a possibility and in order to evaluate the extent to which it can occur at coverages $\leq$1ML, the Au:S ratio versus cluster coverage was fit to a simple model that we will employ on this cluster as well. The model assumes that the sulfur and gold Auger signals are proportional to xI_S and (1-

$bx)I_{Au,}$ respectively, where I_S and I_{Au} are the signal sensitivity factors for the S(LMM) and the Au(MNN) electrons. The value x ($0 \leq x \leq 1$) is the monolayer coverage of the clusters, and the parameter b represents the residual Au(MNN) signal due to the incomplete screening of the surface. The Au:S Auger intensity ratio can then be written as $a(1/x - b)$ where $a = (I_{Au}/I_S)$ and b is expected to be ~0.9 based on the estimated Auger attenuation length using the NIST database of the Au MNN Auger (74 eV) signal.[112]

The solid lines in Figure 4.10 show least square fits of the Au:S ratio data to the expression $a(1/x - b)$, each of which have different restraints as shown in Table 4.1. For the fit where the parameters a and b are allowed to vary independently (green curve), we obtain a very good fit to the data, with $a = 0.45 \pm 0.03$ (Auger sensitivity ratio) and $b = 0.67 \pm 0.15$ (Au Auger attenuation factor). Although, the latter is not entirely in agreement with that calculated from NIST database (~0.90), fixing b= 0.9 still results in a nearly identical fit to the data (blue curve) with a slight change in the Auger sensitivity factor to $a = 0.51 \pm 0.04$. Overall, the model describes the observed Au:S ratio and therefore we conclude that the experimental Auger data is consistent with the clusters adding to the bare areas of the Au surface to form a monolayer before a second layer. The fitted value $a = I_{Au}/I_S$ in all cases is in excellent agreement with the sensitivity factors obtained from the tabulated sensitivity factors for the S(LMM) and the Au(MNN) Auger transitions for and incident electron energy of 5keV which is $I_{Au}/I_S = 0.51$.

4.3.5 Mo_6S_8 on Au(111): Theory of CO adsorption

It has been seen that ^{13}CO is a good probe for the identification of available metal sites in these small sulfide clusters.[33,35] A series of ^{13}CO TPD curves are shown in Figure 4.11 as a function of Mo_6S_8 coverage on the Au(111) surface. The desorption of ^{13}CO from the deposited clusters occurs at temperatures between 281-295K as the cluster coverage increases. All TPD curves shown are for a saturated dose of ^{13}CO, and these exposures can be used to calculate the sticking coefficient for that particular cluster coverage. We use 0.1ML as our base as it represents clusters that are isolated and that should be able to bind 5 CO molecules (one Mo site is bonded to the substrate). We are able to make reasonable estimations in the sticking coefficient as a result of knowing how many ions are on the surface after each deposition. In that way, we are able to calculate the number of available sites for adsorption (5 available sites for each cluster). The sticking coefficient has a value of 0.75 ± 0.1, which was calculated by the number of ^{13}CO molecules that stick to the surface versus the number of ^{13}CO molecules that impinge the surface.

Figure 4.12 shows the ^{13}CO TPD peak temperature and integrated area as a function of cluster coverage. For the ^{13}CO TPD peak area there is a steady increase in intensity until approximately 0.40ML after which there is a plateau in the desorption signal. Similarly, the peak temperature rises until the same monolayer coverage and plateaus after that point. This indicates that the addition of clusters onto the Au(111) up until 0.40ML results in an increase in adsorption sites after which cluster crowding would result in no increase in available metal sites. Changes in the electronic structure on the surface can be observed by the increase in ^{13}CO TPD peak temperature as the cluster coverage increases. It has been seen previously for the

$Mo_4S_6^+$ cluster on Au(111) that as the cluster coverage increases the ^{13}CO TPD peak temperature decreases as a result of crowding on the surface making some sites inaccessible to binding, while other available sites weaken the cluster-CO bond as a result of electronic interactions on the surface.[33] This is not the case for the Mo_6S_8 cluster since the desorption temperature increases indicating there is a strengthening of the Mo-CO bond as the cluster coverage increases on the Au(111) surface. One explanation could be that there is a change in the local electronic structure as the surface accumulates more clusters. Despite the fact that there is little charge transfer between the cluster and the surface, cluster-cluster interactions may highly influence CO binding energies resulting in an overall increases in strength. Density functional theory was used to examine CO binding to the different Mo sites on the supported clusters. The calculations were carried out for the sequential binding of CO to the point of saturation. The total adsorption and binding energies for CO as defined by equation 4.2 and 4.3 can be seen in Figure 4.13. For a coverage of 0.1ML, the cluster will bind up to 5 CO molecules as noted by the steady decrease in the total adsorption energy. For n=1 to n=4 (which are all equivalent Mo sites) the binding energy shows little fluctuation as can be seen by the inset in Figure 4.13. The average binding energy is between -1.2 and -1.3 eV for the occupation of all of the side sites with CO. When the 5^{th} CO is added there is a slight increase in binding energy to -1.48eV demonstrating the inequivalent nature of the top site. The increase in binding energy indicates that the local electronic structure of the Mo is such that the Mo-CO interaction is enhanced. This has been observed previously with the Mo_4S_6 structure where the top Mo site was seen to also have the highest CO binding energy as a

consequence of its slightly positive mulliken charge in comparison to the side sites.[33] Therefore, it could be said that the sequential addition of CO would first begin with the occupation of the top site with the side sites following suit. A decrease in binding energy is observed with the addition of the n=6 CO molecule with a binding energy of -0.35eV, indicating that the adsorption would be energetically unfavorable. In Figure 4.14 it can be seen that the 6th CO molecule would be added to an already occupied Mo site and that the crowding and/or local electronic environment of the Mo atom would not allow this to occur experimentally.

Qualitatively, the observation for a steady CO binding energy up until n=5 may be correlated to the fact that the CO TPD temperature increases slightly as the cluster coverage increases. Repulsive interactions of the adsorbates is not observed with the calculations which would in turn show a decrease in binding energy (desorption temperature). The calculated sticking coefficient of 0.75 ± 0.1 would indicate the binding of an average of 4 CO molecules onto the supported clusters at saturation. This is in relatively good agreement with the calculated CO binding trends.

4.3.6 Mo_6S_8 on Au(111): UPS

A UPS spectra of a clean Au(111) crystal is shown in Figure 4.15a. The features shown between the energies of -2 and -7 eV are attributed to the 5d valence band which has been observed in previous studies.[113] The feature just below the Fermi edge is assigned as the Shockley surface state.[114] Figure 4.15b also shows a UPS spectrum for a 0.30ML coverage of the Mo_6S_8 on the Au(111) surface. Overall, the intensity for the valence band peaks of the Au are lowered in intensity and a small

feature appears at a binding energy of -1.0eV, which can be seen in the expanded region in Figure 4.15b. The difference spectrum helps to denote the cluster contribution at this energy on the surface. DOS calculations of the bare Au(111) and the supported cluster were done and are shown in Figure 4.16 for comparison to experiment. In order to compare to the UPS data recorded in our laboratory the calculated DOS was broadened by a Gaussian function with a FWHM of 0.1eV which is comparable to the resolution our spectrometer. Generally, the DOS is in good agreement with the experiment showing the decrease in signal intensity for the 5d Au contribution as the clusters are deposited as well as the indication of a feature at -0.80eV. Partial density of states calculations done by Popov et. al. is in good agreement with those shown here. It was determined that the Mo-S bonding states should be found between the energies of -5.1eV and -2.0eV.[55] Experimentally we are unable to see these states as a result of the overwhelming signal of the Au valence band. Energies above -2.0eV are the Mo-Mo bonding states of the Mo_6 cluster core, therefore the broad feature at -1.0eV that is observed would correspond to those Mo metal d states within the octahedral center.

4.4 Summary and Conclusions

In this chapter size-selected deposition has been used to investigate the adsorption and thermal properties of the Mo_xS_y clusters supported on a Au(111) single crystal. The nature of the as-deposited clusters were investigated using TPD ^{13}CO studies where the peak shape, desorption temperature, and response to thermal activation, gave information regarding the stability on the surface. Those with small HOMO-LUMO gaps and dangling sulfur bonds exhibit weak CO binding with broad

TPD profiles, while the structures with higher HOMO-LUMO gaps and cage-like geometries appeared more stable on the surface. Previous gas phase studies of the size-selected clusters with CO were used to determine the lowest energy configuration of each of the clusters. The larger clusters Mo_7S_{10} and Mo_8S_{12} were not included in this study but structural information was inferred by comparing the TPD peak shape and temperature to those clusters whose structures have already been solved. As a result, the Mo_7S_{10} could be structurally similar to the Mo_6S_8 in light of the fact that the addition of one MoS unit has been seen to give higher order structures like the Mo_5S_7 based on the more energetically stable smaller Mo_4S_6 unit. In the case of the Mo_8S_{12} the TPD profile suggests that a dimerization may occur of the magic cluster, Mo_4S_6 as the TPD peaks are identical.

Annealing of the Mo_xS_y/Au(111) surface up to temperatures of 400K resulted in the onset of a low temperature peak indicating the formation of an amorphous Mo_xS_y phase on the surface with a desorption temperature of ~240K for each case. The smallest cluster, Mo_3S_7, is unique in this instance since its ^{13}CO desorption temperature falls in this temperature region and exhibits no shift as the cluster is annealed. This demonstrates its instability as it lands on the surface as a consequence of its dangling sulfur bonds. These coordinatively unsaturated sulfur atoms may have strong interactions with the Au substrate stripping the small cluster of its geometric integrity. Upon further annealing to ~700K, each cluster exhibits a loss of CO uptake suggesting that there is a less adsorption sites available. The thermal activation of the surface can therefore promote diffusion of the clusters on the Au and the formation of two-dimensional amorphous Mo_xS_y islands.

A more comprehensive study on the Mo_6S_8 on the Au surface revealed a stable square bridge adsorption orientation with a relatively strong binding energy of -1.79eV which is comparable to previous calculations done on the cluster.[55] Auger measurements as a function of cluster coverage show that the clusters should behave independently to coverages up to ~0.15ML. However, ^{13}CO thermal desorption studies show that there is a non-linear increase in the CO signal intensity up to ~0.40ML and that the number of available metal sites does not increase at 0.50ML indicating that cluster crowding has begun. Since there is a low barrier for diffusion on the surface it may be that there is an adsorbate induced organization of the clusters so as to limit repulsion between CO molecules. It has been reported that the Mo_6S_8 may be able to self assemble on the Au(111) surface.[56] However, this has yet to be observed experimentally. The top site was found to bind CO more strongly, likely due to the local electronic structure of the Mo atom that is far removed from the Au surface. Calculations suggest that the CO binding is additive up to 5 CO molecules and is in good agreement with the calculated sticking coefficient of 0.75±0.1eV. Photoemission experiments and theoretical calculations show an appearance of a broad feature at -1.0eV that is a consequence of the Mo-Mo bonding d states of the octahedral metal core.

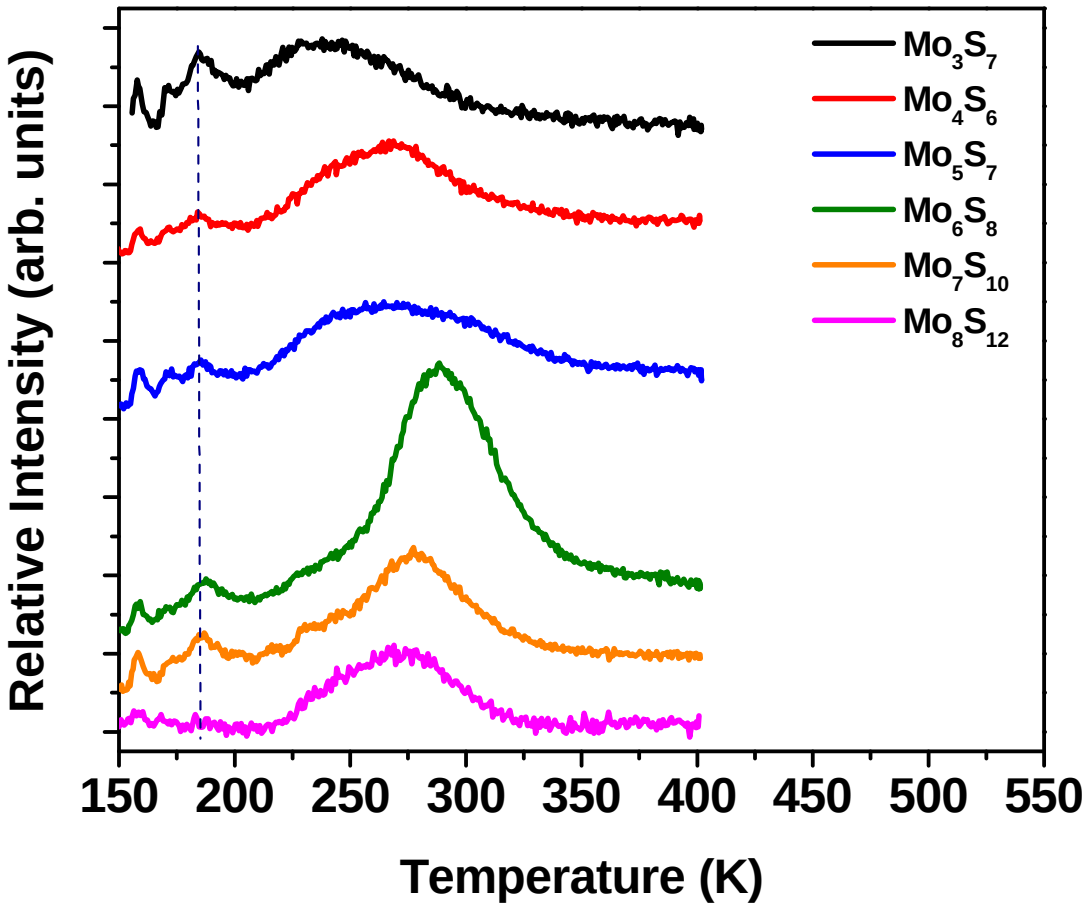

Figure 4.1: ^{13}CO TPD spectra for the a 0.3ML coverage of the Mo_xS_y clusters deposited on Au(111). Dotted line denotes ^{13}CO desorption signal from defect sites on the Au(111) crystal.

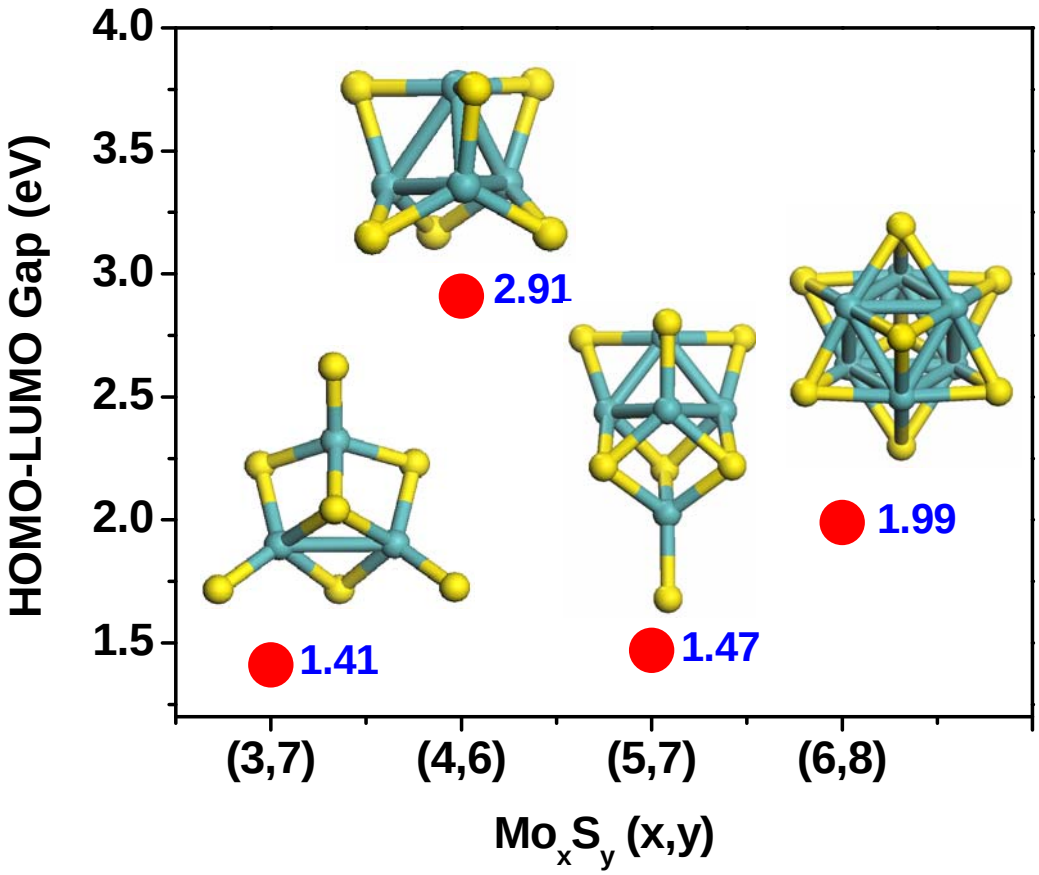

Figure 4.2: DFT calculated HOMO-LUMO gaps for the Mo_3S_7, Mo_4S_6, Mo_5S_7, and Mo_6S_8 clusters. The lowest energy structure for each cluster is also shown.

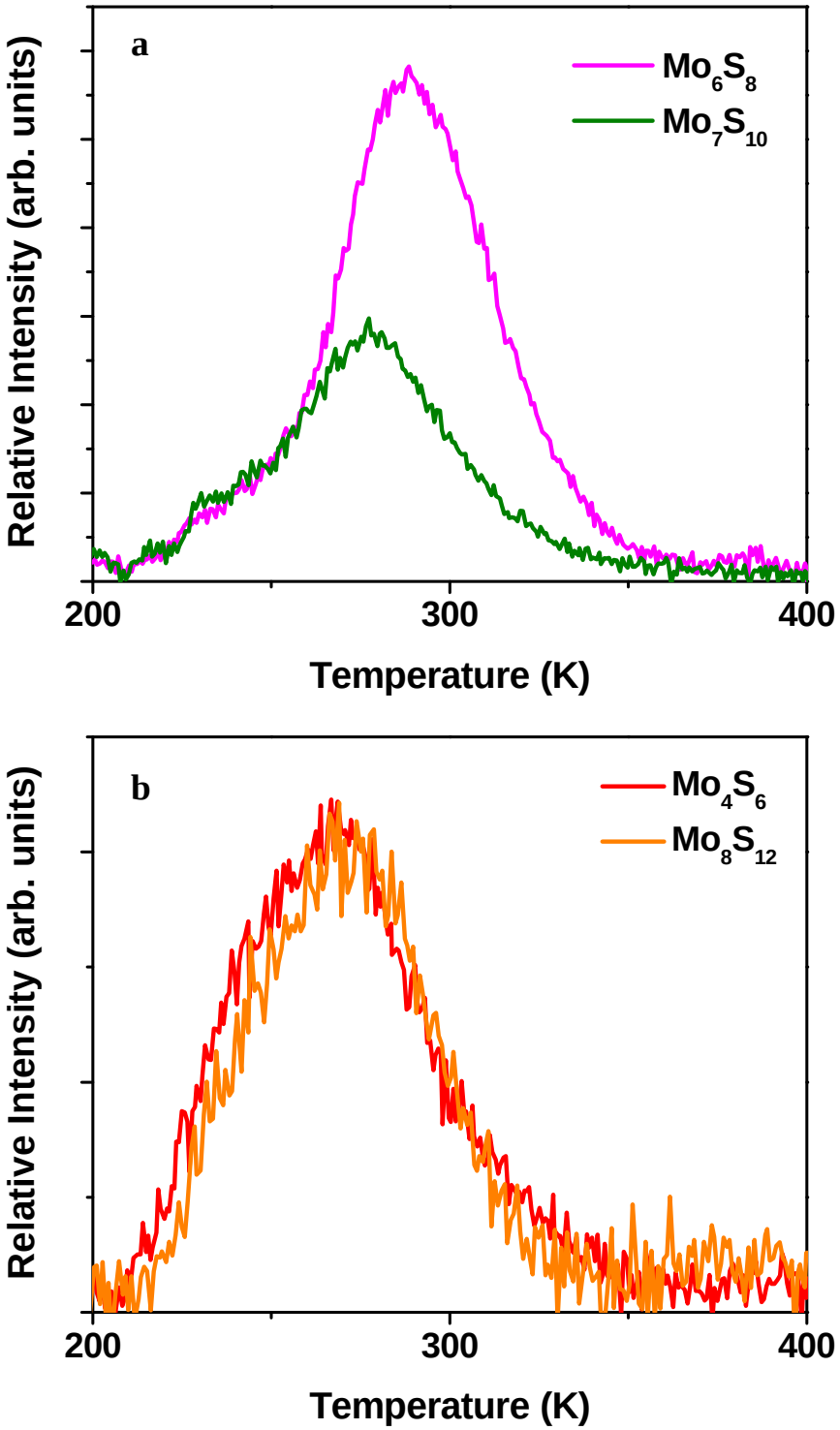

Figure 4.3: ^{13}CO TPD comparison spectra for the a) Mo_6S_8 and Mo_7S_{10} clusters and b) the Mo_4S_6 and Mo_8S_{12} clusters supported on Au(111). Each cluster is at a coverage of 0.3ML.

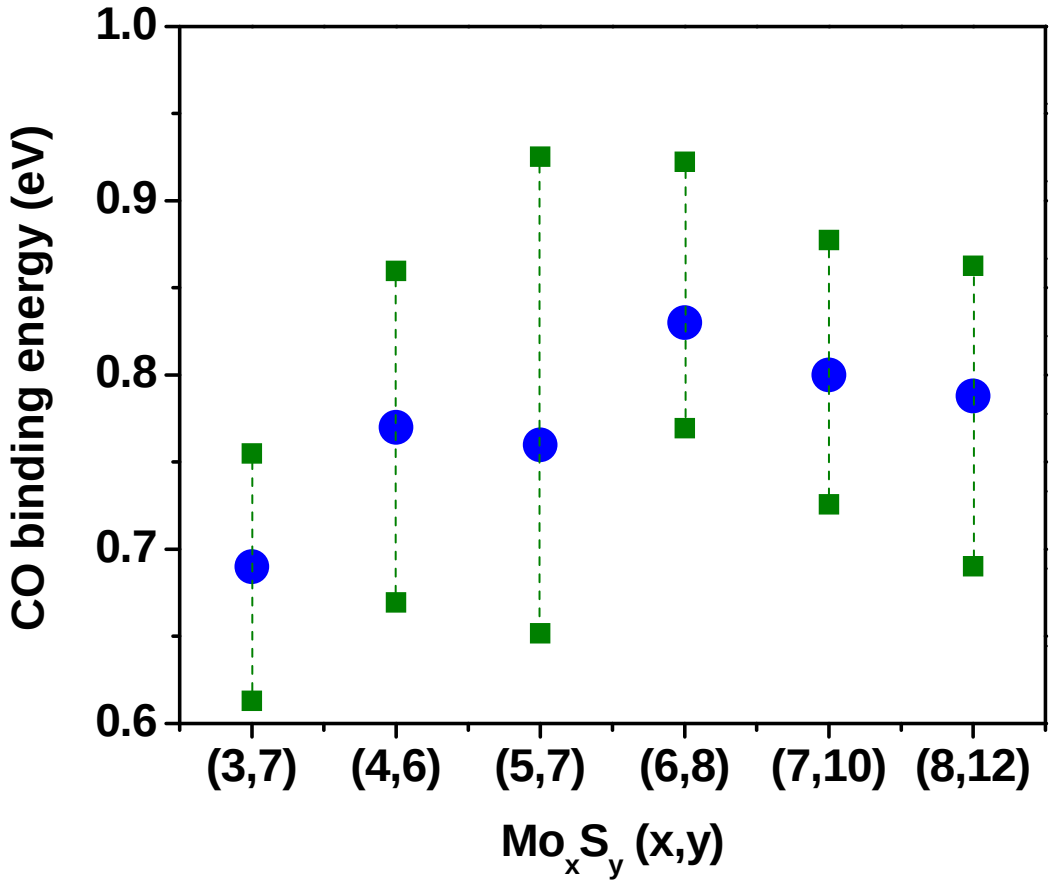

Figure 4.4: Calculated CO binding energy for the different Mo_xS_y clusters supported on Au(111). The blue dot denotes the binding energy at the peak maximum while the dotted green line is indicative of the peak width in eV.

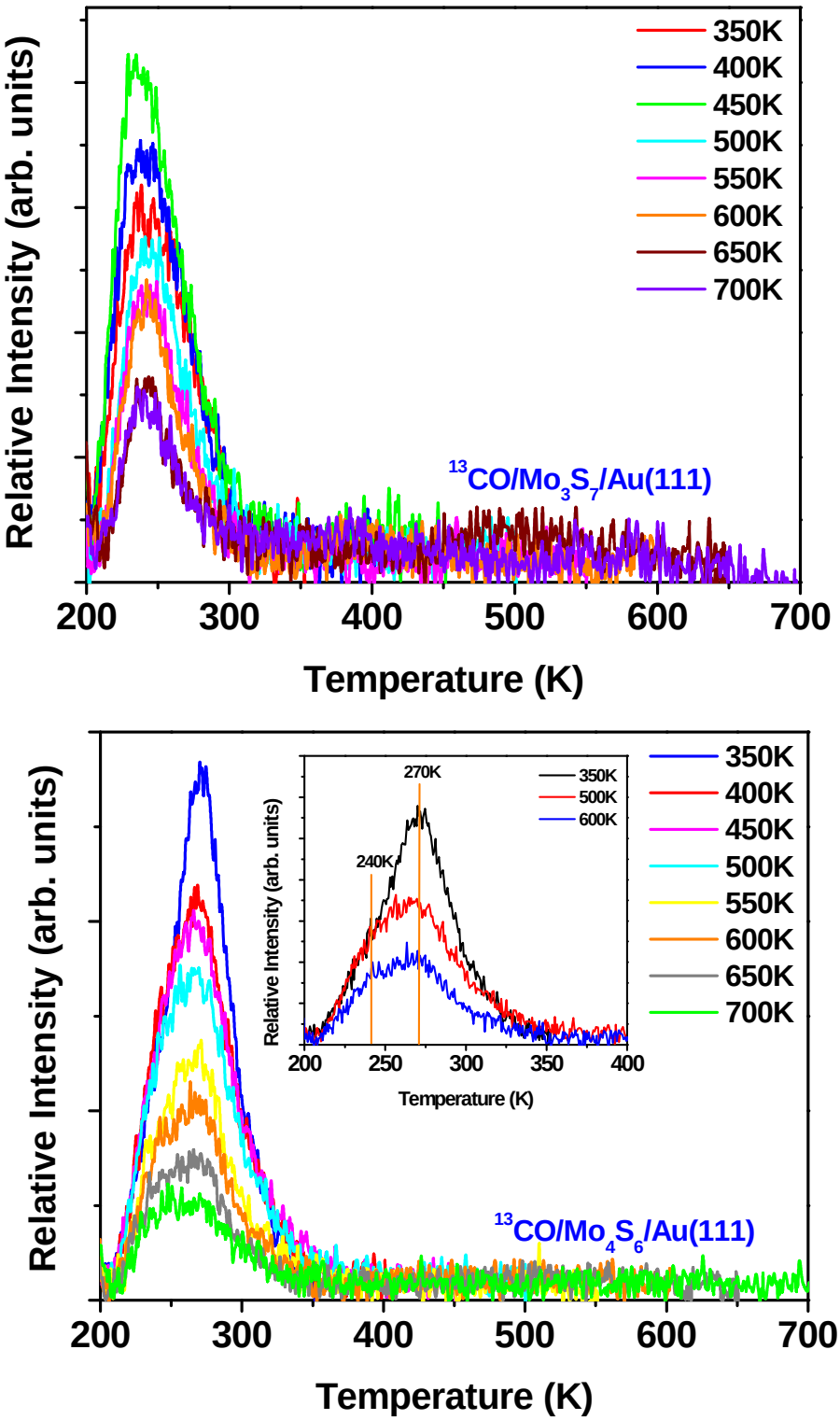

Figure 4.5: Temperature programmed desorption spectra of ^{13}CO on 0.30ML of Mo_3S_7 and Mo_4S_6 on Au(111) as a function of crystal annealing temperature. The inset in shows the onset of a low temperature feature.

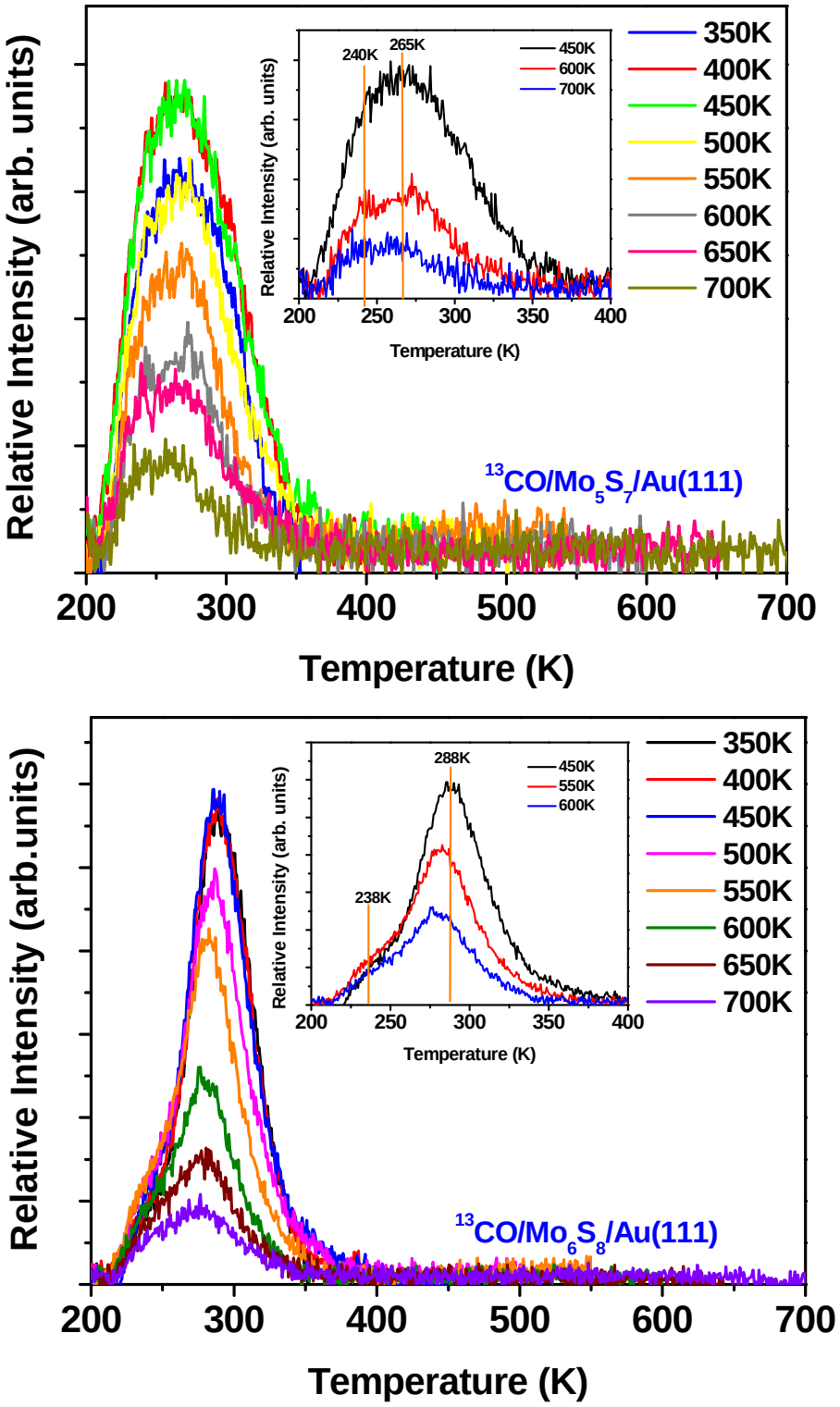

Figure 4.6: Temperature programmed desorption spectra of ^{13}CO on 0.30ML of Mo_5S_7 and Mo_6S_8 on Au(111) as a function of crystal annealing temperature. The insets in shows the onset of a low temperature feature.

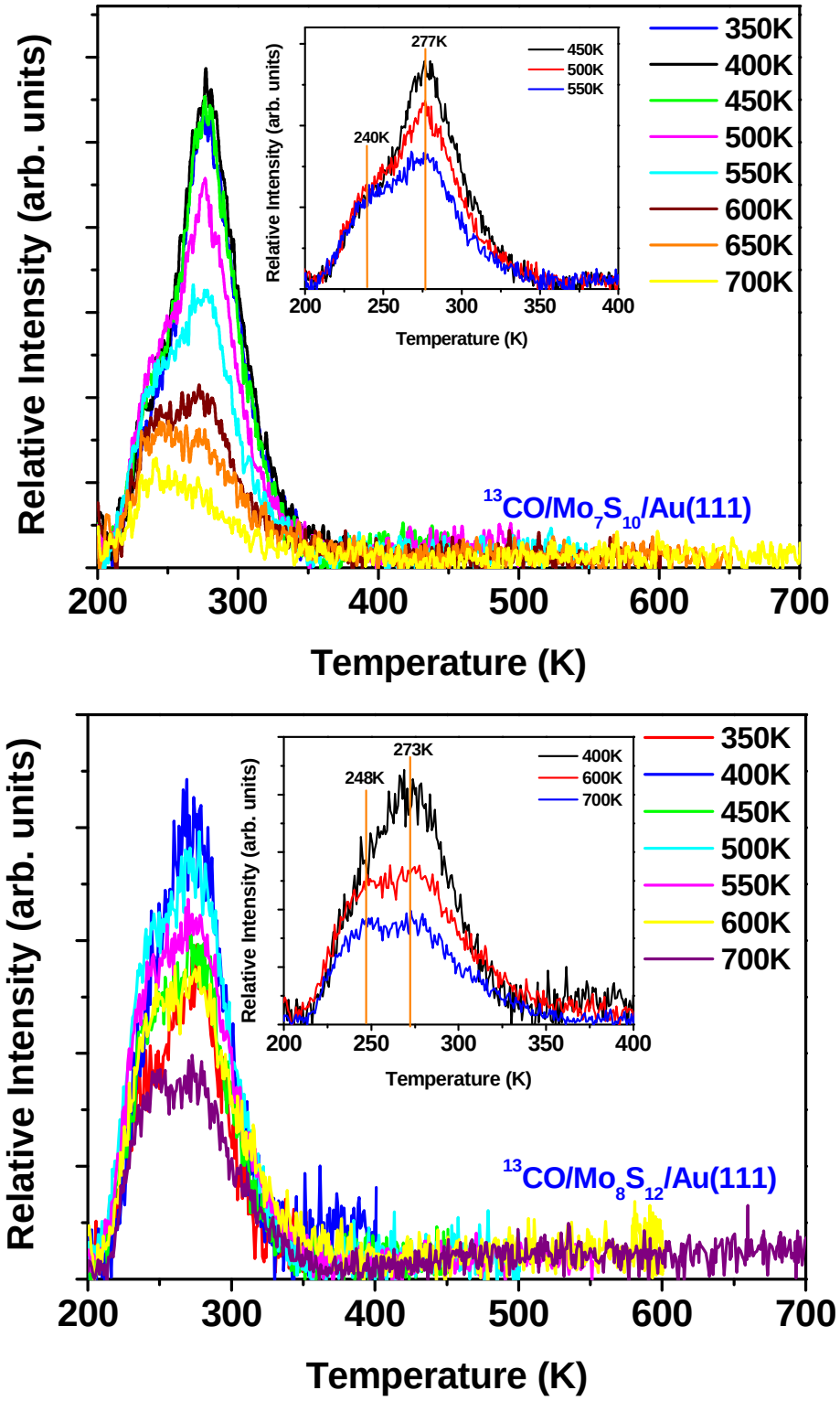

Figure 4.7: Temperature programmed desorption spectra of ^{13}CO on 0.30ML of Mo_7S_{10} and Mo_8S_{12} on Au(111) as a function of crystal annealing temperature. The insets in shows the onset of a low temperature feature.

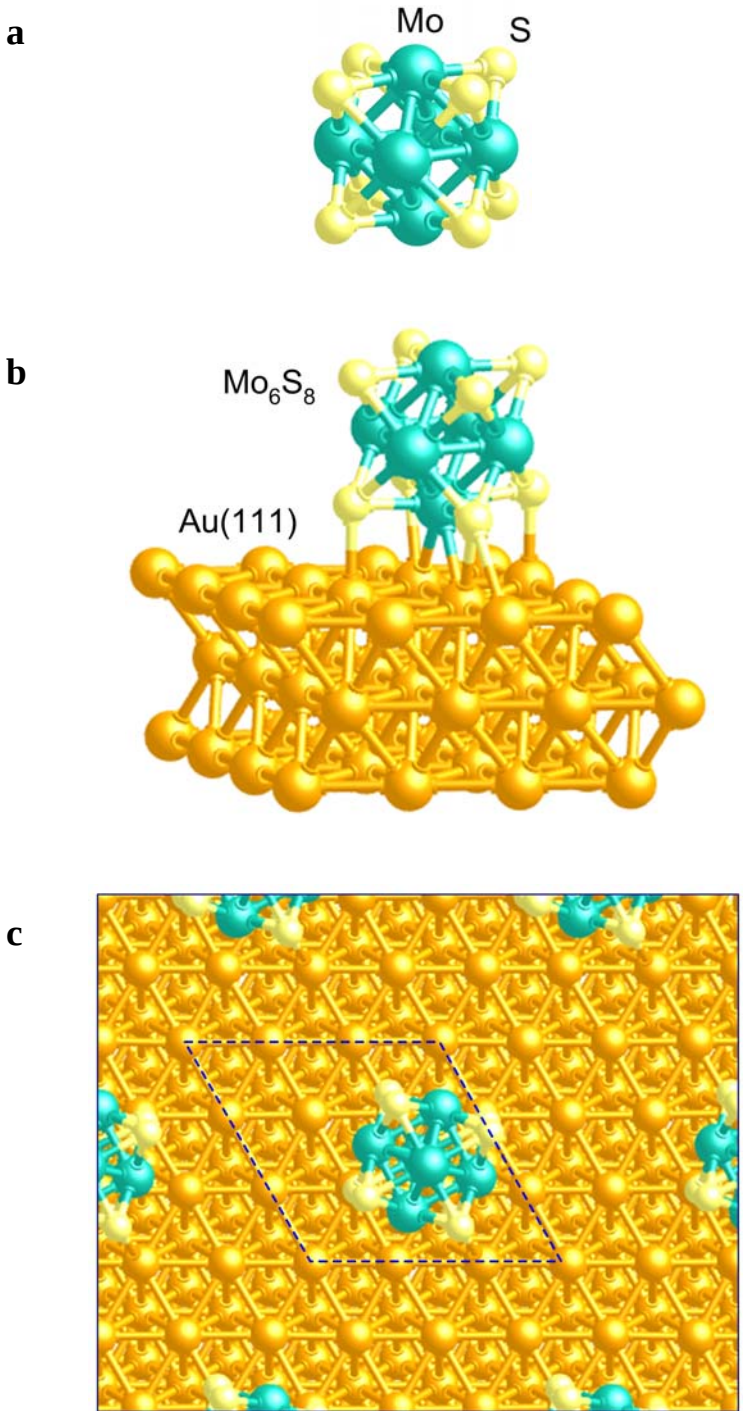

Figure 4.8: a)Geometry optimized structure as calculated by DFT of the a)Mo_6S_8 cluster, b) Mo_6S_8 cluster supported on Au(111), and c) top down view of 4x4 supercell.

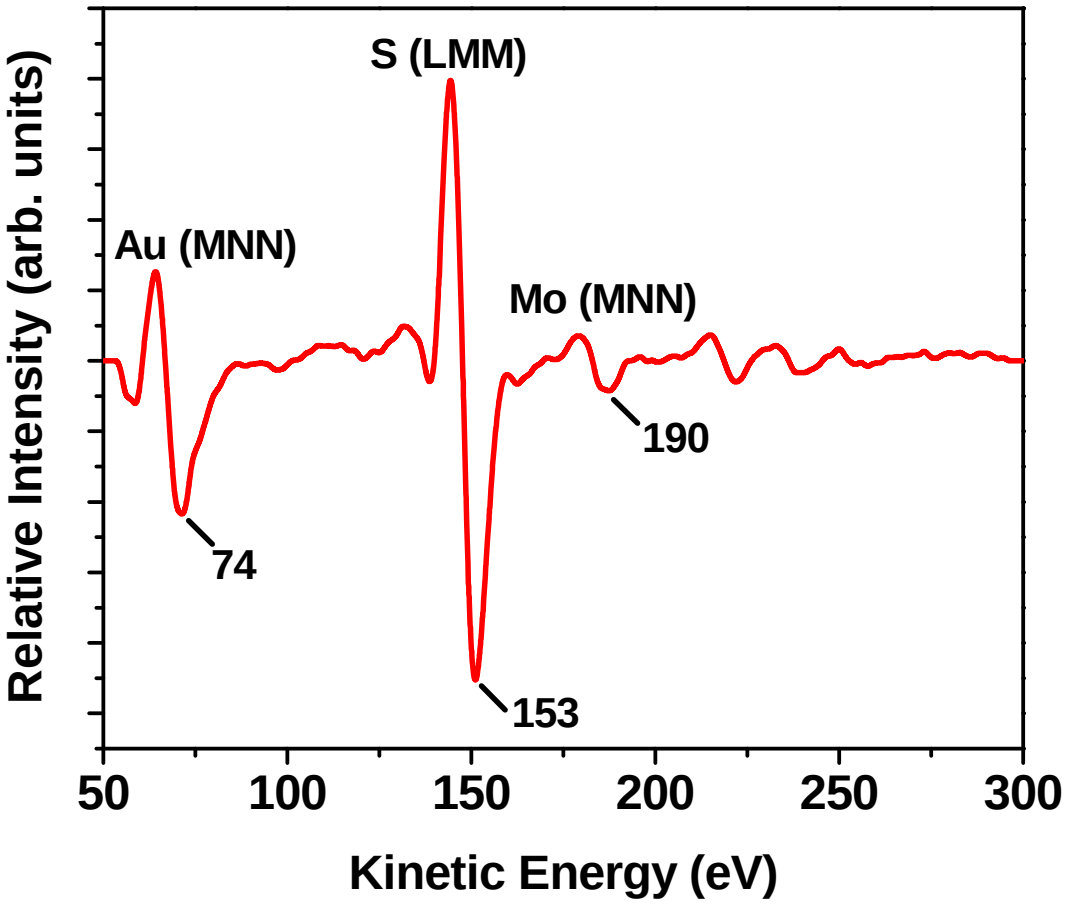

Figure 4.9: AES spectra of a 0.4ML coverage of Mo_6S_8 on Au(111).

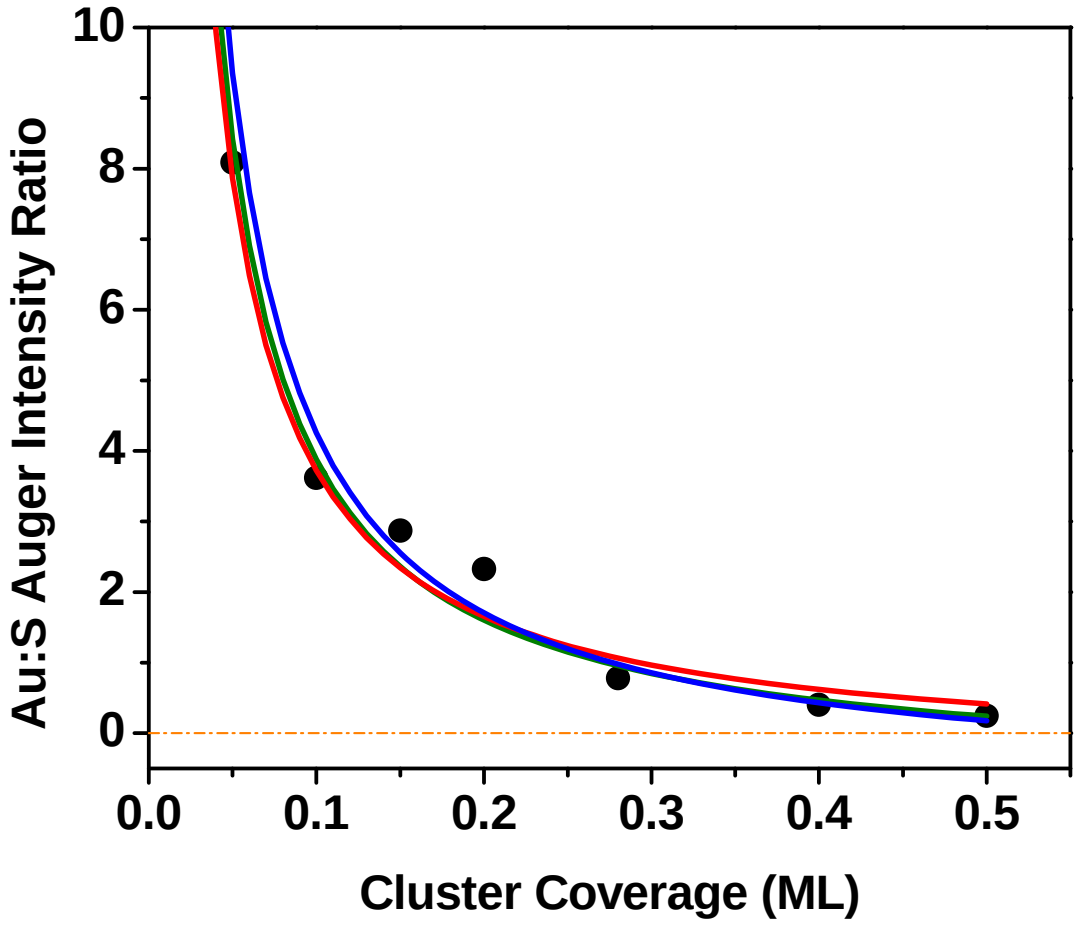

Figure 4.10: Cluster coverage dependence of the Au:S Auger Electron Spectroscopy peak intensities. The three lines represent least-squares fits of the data to a model function. See section 4.3 and table 4.1 for details. Orange dashed line is displayed to show the origin.

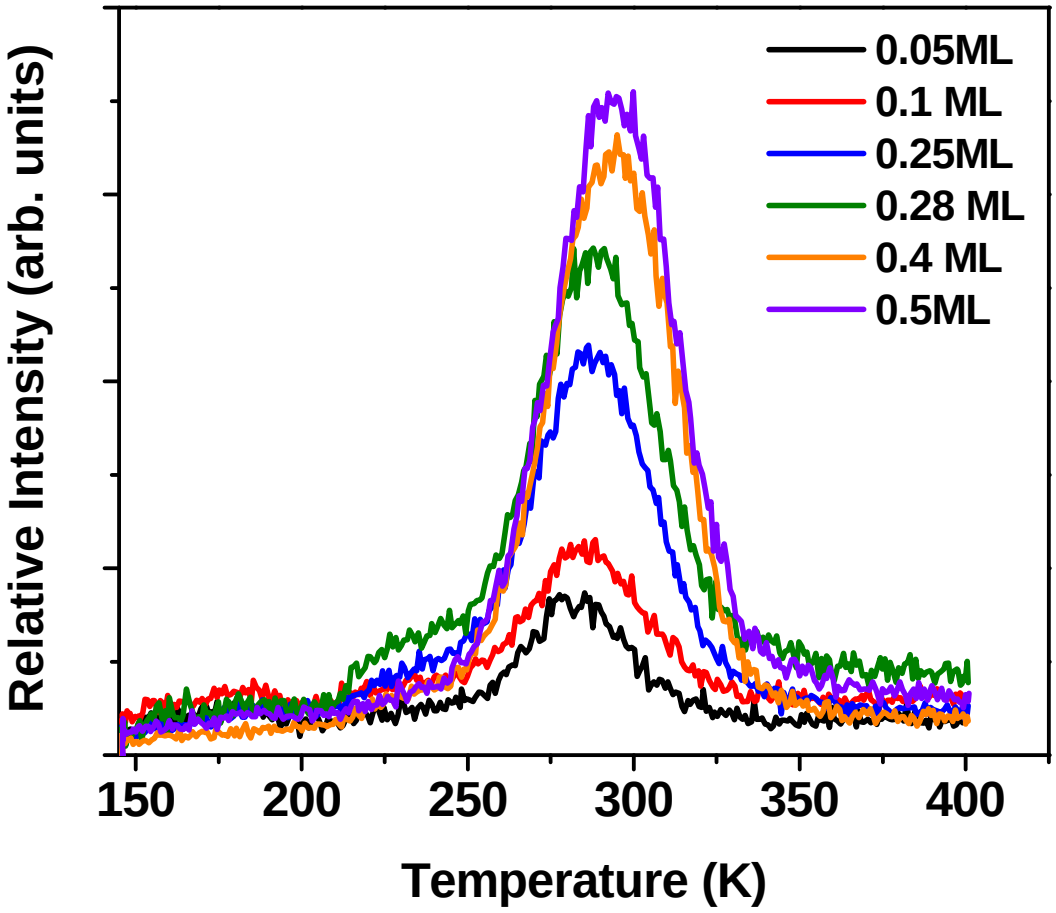

Figure 4.11: Temperature programmed desorption of ^{13}CO as a function of Mo_6S_8 cluster coverage on Au(111). A saturated dose of ^{13}CO was used in each case.

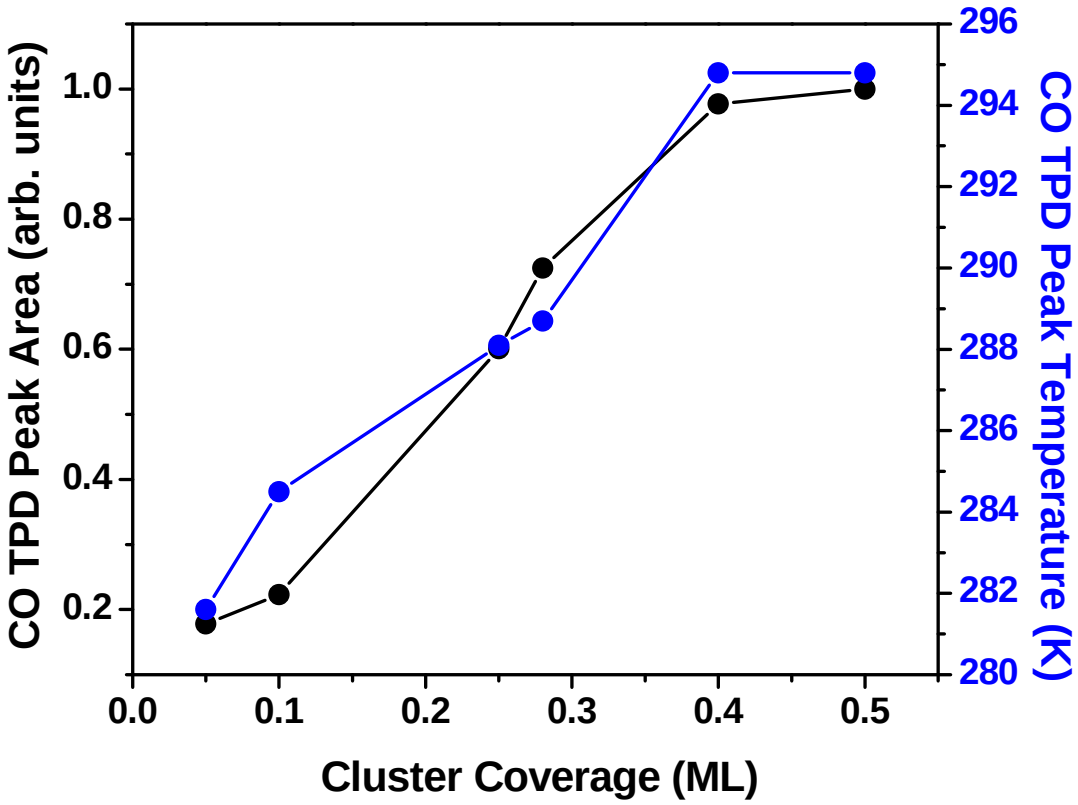

Figure 4.12: ^{13}CO TPD peak temperature (blue) and integrated peak area (black) as a function of cluster coverage.

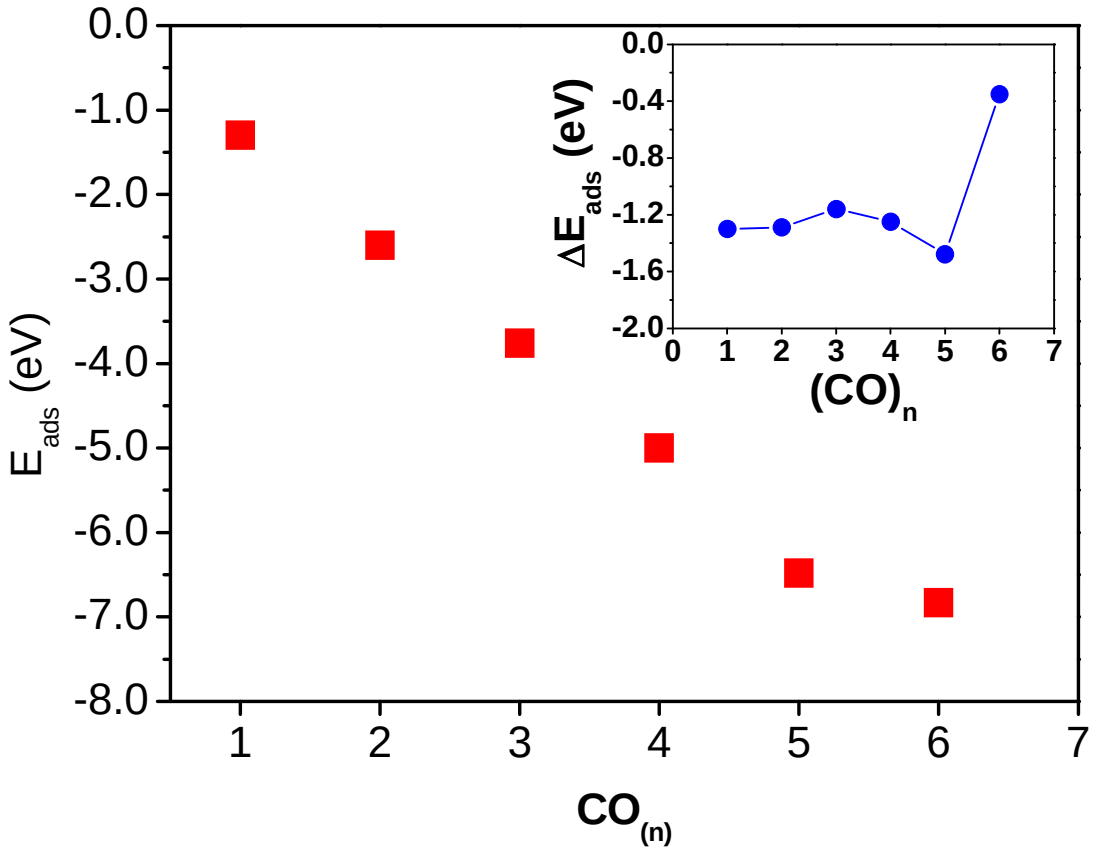

Figure 4.13: Total adsorption energy diagram for the sequential addition of CO on the Mo_6S_8 cluster supported on Au(111). The inset shows the binding energy for each CO molecule.

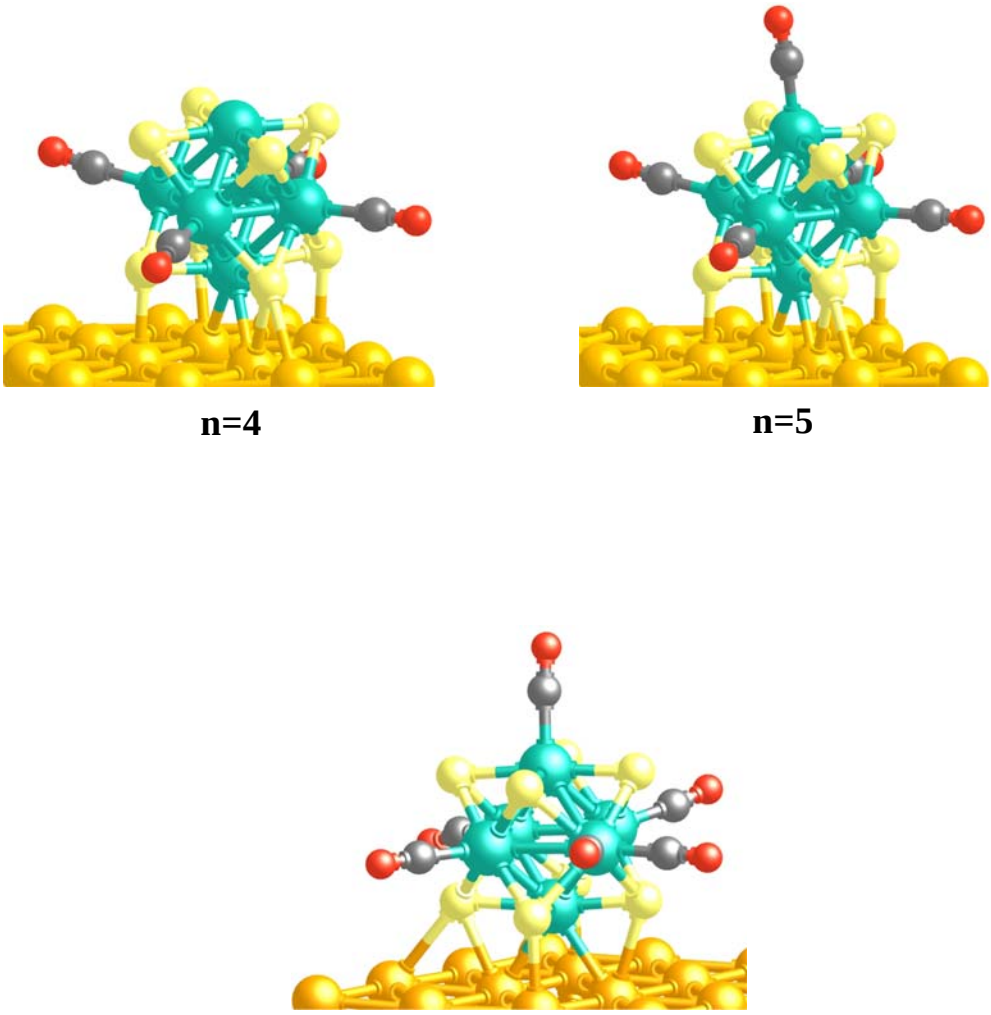

Figure 4.14: Geometry optimized structures for the n =4, n=5, and n=6 CO configurations on Mo_6S_8/Au(111) configurations as determined by density functional theory.

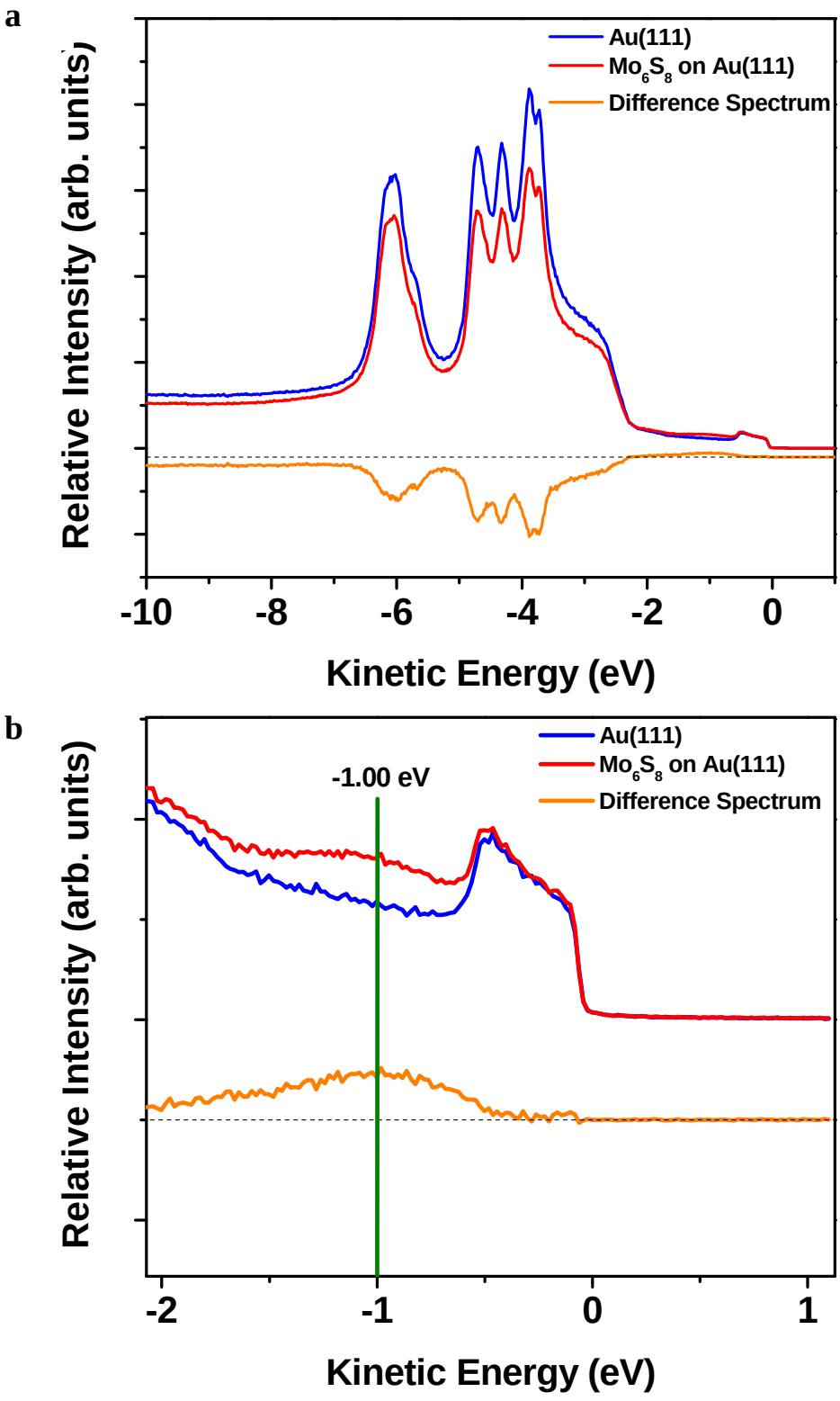

Figure 4.15: a) UPS spectrum of bare Au(111) and 0.30ML of Mo_6S_8 on Au(111) and b) expanded region of the Mo_6S_8 contribution on the surface.

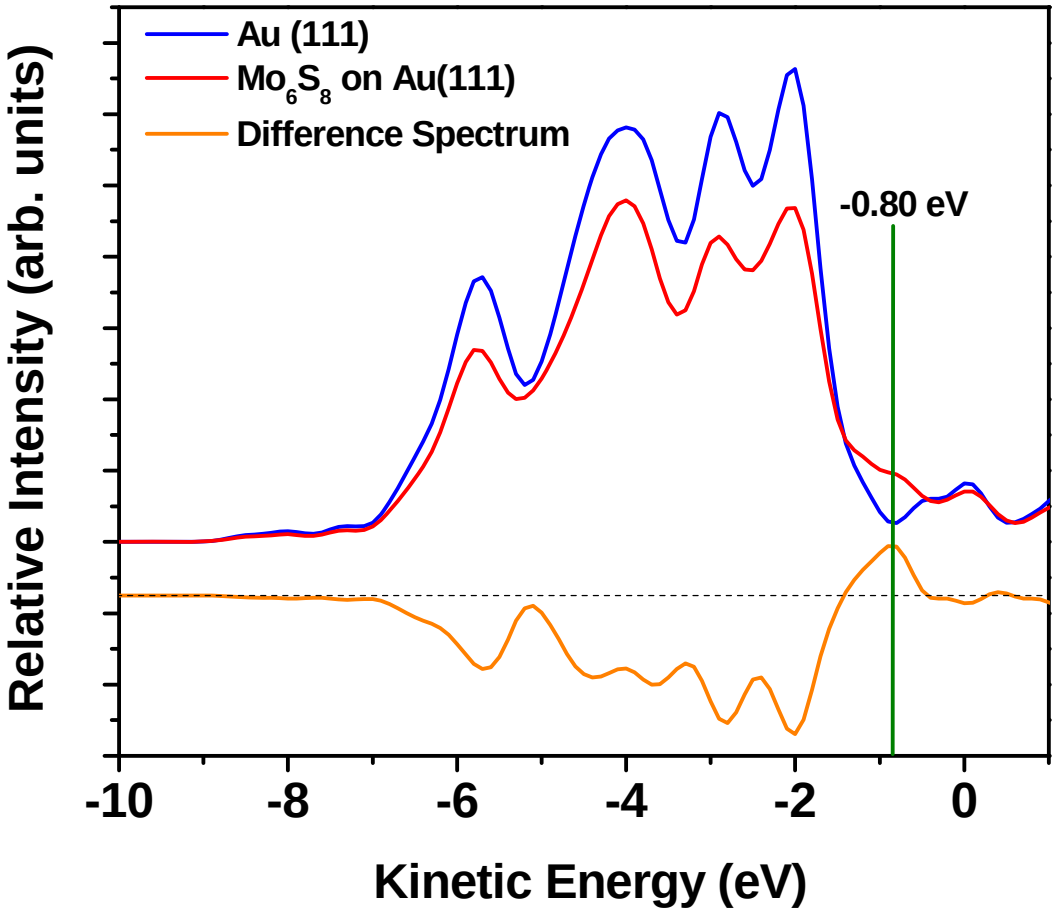

Figure 4.16: Calculated DOS for the bare Au(111) and the Mo_6S_8 cluster supported on Au(111).

Fit Constraints	Calculated S_x	Calculated Attenuation Factor
b = a where a and b vary independently	0.45	0.68
b = a	0.41	1.00
a = 0.51* and b can vary	Fixed at 0.51	0.60

Table 4.1: Fit parameters and constraints for the least squares fit of the Au:S signal intensity as a function of cluster coverage.

Chapter 5. Dissociation of OCS on Mo_6S_8/Au(111)

5.1 Introduction

The need to study hydrotreating processes for the clean-up of fossil fuel and crude oil of impurities through hydrodesulfurization (HDS) and hydrodenitrogenation (HDN) is of significant importance from an economic and environmental standpoint. Pollutants such as SO_x and NO_x gases are of primary concern as they create hazards to human health and atmospheric quality. To date, one of the most widely used catalysts for HDS and HDN processes is stoichiometric molybdenum sulfide, MoS_2.[11,97] Characterization of such catalysts are difficult because of their chemical and structural heterogeneity therefore making it unclear which properties are important for these processes. Model catalytic systems on single crystal substrates or well characterized thin films have been used in surface science to probe catalytic processes that otherwise could not be thoroughly studied as a result of inhomogeneity in the active components.[44,46,47] For example, HDS reaction pathways have been examined on MoS_2 nanoclusters supported on Au(111) detailing interactions between thiophene and the supported nanoclusters with no involvement of the support.[45]

In bulk form, gold is considered an unreactive metal and the closed packed Au(111) surface has often been used as a non-interacting substrate for studying the electronic structure and reactivity of supported metal[48-50] and metal compound[51-53] nanoparticles. Of particular interest are recent experimental studies of small molybdenum sulfide nanoclusters deposited on the Au(111) surface which are used to explore the atomistic details of desulfurization reactions that are relevant to the

industrial hydrotreating of fossil fuels.[33,43,45,47,57,58] In the work of Besenbacher and coworkers,[43,45,57,58] the electronic structure and reactivity of triangular nanoplatelets of MoS_2 grown on the Au(111) surface were found to be unperturbed by the underlying gold surface. For the non-stoichiometric Mo_4S_6 and Mo_6S_8 nanoclusters on the Au(111) surface, theory predicts relatively strong S-Au bonds,[54-56] and recent experiments suggest that cluster-Au interactions modify their electronic and chemical properties.[33] In this work, we report the observation of an unusual catalytic reaction in which the Au(111) surface directly participates in the catalytic decomposition of carbonyl sulfide (OCS) which is initiated by the Mo_6S_8 supported on the Au surface. The reaction studied here is the dissociation of carbonyl sulfide, i.e.,

$$OCS_{(a)} \rightarrow CO_{(g)} + S_{(a)} \qquad (5.1)$$

on a surface consisting of a sub-monolayer coverage of Mo_6S_8 clusters deposited on a Au(111) surface. As a simple desulfurization reaction, the dissociation of OCS yields gas-phase $CO_{(g)}$ products which are readily detected in the gas phase. Moreover, the relative simplicity of the reaction also makes this system more amenable to theoretical modeling, including transition states as demonstrated in this work. The selection of the Mo_6S_8 cluster for investigation is due to its unique structural properties and potential as a nanocatalyst. The Mo_6S_8 cluster is well-known as the basic building block of the Chevrel phase of molybdenum sulfide with a unique cage-like structure in which the eight sulfur atoms are located in the triangular faces of a Mo_6 octahedral core. From the standpoint of HDS catalysis, it is known that the active sites for reaction on industrial catalysts are associated with metal sites (Mo or Ni/Co promoter atoms) located at the edges of MoS_2 nanoparticles.[11,99] In addition to having

Mo-Mo bonds that are absent in stoichiometric MoS_2, the Mo_6S_8 cluster bonded to Au(111) has five (one atop site, 4 side sites) coordinatively unsaturated Mo atoms which can act as active sites for adsorbate binding and reaction.

5.2 Experimental

Experimental details for this chapter have been described in Chapter 4, Section 4.2. Briefly, we use a magnetron sputtering source to generate a distribution of $M_xS_y^+$ cation clusters, from which the $Mo_6S_8^+$ cluster is mass-selected by a quadrupole filter and then "soft-landed" on the Au(111) surface under UHV conditions. Cluster deposition was performed at room temperature at coverages between 0.05 ML and 0.5ML. The TPD experiments were performed using a linear heating ramp of ~2 K/sec and desorbing molecules were detected by quadrupole mass spectrometer (electron impact ionization) enclosed in a LN-cooled vacuum housing.

Theoretical calculations using density functional theory (DFT) were also performed in this work using the VASP code for OCS binding and dissociation on the Au-supported Mo_6S_8 cluster. YongMan Choi and Ping Liu of Brookhaven National Laboratory did all calculations in this section of the work. The total adsorption energy of OCS bound to the supported cluster was calculated from the following:

$$E_{ads} = E(n\mathrm{OCS}/\mathrm{Mo_6S_8}/\mathrm{Au}) - E(\mathrm{Mo_6S_8}/\mathrm{Au}) - E(n\mathrm{CO}) \qquad (5.2)$$

The binding energy for the sequential addition of OCS onto the supported cluster was determined using the following equation:

$$\Delta E_{ads}(n) = E_{ads}(n) - E_{ads}(n\text{-}1) \qquad (5.3)$$

The Mo_6S_8 cluster is slightly distorted relative to the free cluster as a result of the mismatch between the cubic arrangement the four S-atoms at the base of the cluster and the hexagonal structure of the Au surface atoms.

5.3 Results and Discussion

5.3.1 Thermal Desorption of OCS on Mo_6S_8/Au(111)

Figure 5.1a and 5.1b show the TPD spectra for the desorption of OCS on the bare Au(111) crystal and the Mo_6S_8 supported on Au(111) respectively. In each, the desorption signal for CO (m/e = 28) and OCS (m/e = 60) is monitored. For the bare Au(111) surface an OCS desorption peak is observed at ~121K as well as a small amount of CO (6% of the OCS signal) which is a consequence of fragmentation of the parent molecule in the ion source of the mass spectrometer. Once the clusters are deposited there is a shift in the substrate OCS desorption peak to ~125K. The assignment for the shift in the bare Au(111) OCS desorption peak is consistent with Figure 5.2 which displays TPD spectra for the interaction of OCS on the supported cluster as a function of the cluster coverage. As the coverage increases (less Au exposed on the surface), the contribution of the low temperature OCS on Au(111) peak decreases. By comparing TPD spectra for the bare substrate and the cluster covered Au(111), it is clear that the CO dissociation signal is a consequence of the deposited clusters. The latter is supported by the fact that the CO fragmentation signal is very low and therefore it should have a negligible contribution to the resulting OCS dissociation peak.

The higher temperature OCS TPD peak in Figure 5.1 is only observed in the presence of clusters and is attributed to reversible adsorption/desorption of OCS on

the supported Mo_6S_8 cluster with a desorption temperature of 195K (at 0.2ML). With increasing coverage (Figure 5.2), the peak temperature is seen to shift from 190 K to 209 K, while the integrated intensity initially increases but then plateaus as shown in Figure 5.3. The saturation behavior of OCS desorption from the cluster is similar to that observed in a previous study (chapter 4) of ^{13}CO adsorption/desorption on the Mo_6S_8 cluster also deposited on Au(111). The observed plateau in the ^{13}CO desorption yield was explained by cluster crowding at higher coverage that leads to the physical blocking of Mo-side sites therefore there would be no net increase in the amount of adsorbate binding. The shift in the OCS TPD peak temperature is also consistent with ^{13}CO trends indicating an increase in binding energy as the cluster coverage increases. This may be a result of changes in the electronic structure of the deposited clusters as previously observed with ^{13}CO thermal desorption measurements.

Figure 5.4 shows the TPD profiles for the OCS reaction cycle as a function of OCS exposure time to the Mo_6S_8/Au(111) system. A notable aspect of this dissociation reaction is that it occurs at lower temperature (110-175 K; peak temperature is cluster coverage dependent) than desorption of intact OCS molecules from the cluster (160-230K). This indicates that some adsorption sites on the Mo_6S_8 cluster can activate dissociation, whereas others cannot. From the relative desorption yields of CO versus OCS, dissociation is favored over simple adsorption. These two observations suggest that most of the Mo-atom sites can promote dissociation. The latter is supported by OCS coverage-dependent TPD experiments shown in Figure 5.4, that show that OCS desorption saturates at lower coverages than the CO product.

From the calculated structure of the cluster it is expected that the supported cluster has four equivalent Mo-atom side sites active for dissociation (see Figure 4.5b) and one top site for molecular adsorption/desorption. Theoretical calculations presented later on this chapter will help support the idea of the sides sites being the preferred binding site for the dissociation channel.

Presuming that the dissociation reaction is occurring on the cluster and the resulting S-atom binds to the Mo-atoms of the cluster, it should be the case that at some point the reaction will no long occur. Generally, HDS catalysts are often "poisoned" by the reaction processes as their goal is to remove impurities through binding on the metal sites. Based on this, the dissociation channel should "shut" off at a certain point since there are limited Mo sites for reaction and sulfur binding. However, we did not observe a decrease in the activity of the catalyst after many reaction cycles. Figure 5.5 shows ^{13}CO thermal desorption spectra before and after ~15 OCS reaction cycles. ^{13}CO binds to the available Mo sites on the cluster, therefore if the Mo sites are being poisoned through dissociation sulfur dissociation products binding to the Mo sites, there should be a significant decline in the ^{13}CO signal intensity as the reaction cycle is run over and over again. This is not the case, as it can be seen that both TPD spectra before and after the reaction cycles are nearly identical.

One possible explanation for such an observation is that the reaction is occurring on the Au surface modified by the presence of the cluster and not on the supported cluster itself. To verify the active species, a "poisoning" experiment was performed in which CO adsorption was used to block the Mo-atom binding sites prior

to exposure to OCS. The Au-supported Mo_6S_8 clusters bind CO more strongly than OCS as evidenced by its significantly higher desorption temperature, i.e., ~300 K for CO versus ~200 K for OCS (see Figure 5.5). In these experiments the as-deposited Mo_6S_8/Au(111) surface was first exposed to a saturation dose of ^{13}CO at 150K so as to avoid ^{13}CO binding to exposed areas of the Au(111) surface. The surface was then cooled to 100 K and dosed with OCS followed by a thermal desorption measurement. The results in Figure 5.6 show that when all of the Mo sites are occupied by ^{13}CO molecules, desorption of OCS (me/ = 60) from the cluster and the CO (m/e = 28) reaction product are strongly suppressed. Desorption of ^{13}CO (m/e = 29) from the cluster and OCS from the Au(111) surface are the only products observed (the very small CO (m/e = 28) signal is due to OCS fragmentation in the ion source). It is clear from these results that the Mo-atom sites on the supported Mo_6S_8 cluster are necessary for OCS dissociation.

5.3.2 OCS Binding on Mo_6S_8/Au(111)

To develop a better understanding of the OCS dissociation mechanism on the Mo_6S_8/Au(111) surface, several DFT calculations were performed starting with the interaction between OCS on the supported Mo_6S_8 cluster. Figure 5.7 shows four different binding configurations for OCS on Mo_6S_8/Au(111). Structure I is the least stable of the four configurations with the OCS doubly coordinated via the S atom bound to a Mo side site (Mo_{ss}) of the cluster and the oxygen atom bound to an atop site on the Au(111) surface. This is a relatively unstable geometry as the OCS molecule is highly distorted when bound to both the cluster and substrate. Structure II with the OCS molecule bound on a Mo top site (Mo_{ts}) has a larger binding energy

than Structure I. The most stable OCS binding configuration (IV), with an adsorption energy of -0.44eV, is shown to be bound via the sulfur atom to a Mo_{ss} with the molecule oriented parallel to the surface normal. Nearly energetically degenerate, structure (III) shows the OCS molecule bound to the same Mo site with its orientation perpendicular to the surface normal. Mulliken population charges, shown in Table 5.1, indicate that there is little charge transfer between the OCS molecule and the Mo site it is occupying with only slight negative charge transfer to the metal atom. However, there is considerable redistribution of charge within the OCS molecule itself, as the sulfur atom shows an electron transfer to the carbon atom in all the configurations shown.

The stability of sequential addition of OCS on the supported cluster was also analyzed using DFT calculations. Previously, it has been seen that the cluster should be able to bind up to 5 adsorbate molecules assuming that there are no adsorbate-adsorbate interactions that would inhibit it. Figure 5.8 shows a total adsorption energy plot for the consecutive addition of OCS molecules onto the surface. The OCS will bind with Structure IV's orientation, as it is the most stable and will continuously add OCS molecules to the other 3 equivalent side sites and finally occupy the top site. The n=4 to n=6 structures are shown in Figure 5.9. The binding energy plot (inset in Figure 5.8) shows a steady decrease in the binding energy from -0.44eV for n=1 to -0.33eV for n=5, while the addition of a 6^{th} molecule is unlikely as demonstrated by the fact that it is unbound to the cluster at the end of the calculation. Therefore, given the theoretical evidence, the supported cluster should be able to

saturate all of its Mo sites with OCS molecules prior to dissociation or molecular desorption.

5.3.3 Dissociation Pathway for OCS/Mo_6S_8/Au(111)

Given that the relative yields of the TPD peaks indicate that dissociation is favored over molecular desorption, and the side site is the most stable binding configuration, it can be assumed that the side site would be the starting point for the dissociation reaction to occur. Furthermore, while there has been evidence through "poisoning" experiments, that the clusters are necessary for the dissociation to occur, the question still remains as to where the sulfur atom goes at the end of the reaction cycle. Theoretical investigations were done to ascertain the most energetically favorable reaction mechanism for the dissociation of OCS on the supported cluster. The lowest energy path for dissociation is shown in Figure 5.9. The relatively low temperature at which the dissociation reaction occurs indicates that the OCS undergoes a dissociative adsorption on the surface. The first barrier and transition state (TS1) involves the breaking of the carbon-sulfur bond of the OCS molecule with the CO molecule still bound to the Mo_{ss} and the sulfur atom doubly coordinated between the Mo-atom and the Au(111) surface. This first local intermediate structure illustrates how the Au directly participates in the dissociation event by anchoring the sulfur atom to the surface. Subsequently, once the full dissociation has occurred, the sulfur atom migrates to the Au(111) surface (TS2) where it binds in a three-fold hollow site with a very high binding energy of -3.54eV. In Figure 5.10 the sulfur binding configurations have been accessed theoretically and it confirms that the sulfur atom bound to the hollow site is the most stable (S5). Once the sulfur atom has

dissociated from the molecule and diffused to the surface, the CO can then be removed from the cluster with a relatively small barrier (TS3) resulting in the intact Mo_6S_8 cluster and a sulfur atom bound nearby on the Au surface. As a result of this observation, it is now understandable why the reaction cycle does not terminate after several runs. Because the dissociated sulfur molecule settles onto the Au surface, all of the active metal sites are still available for further catalysis.

Figure 5.11 helps demonstrate the important role the Au substrate has in the OCS dissociation process. Figure 5.11a shows an alternate reaction pathway in which the sulfur atom does not bind to the Au surface to form a local intermediate structure. Instead, the dissociation occurs with the CO occupying the Mo-top site and the S adsorbed onto the Mo-side site. This configuration was chosen because it was the next stable adsorption site for the dissociated sulfur atom (Figure 5.10, S3) with a binding energy of -3.18eV. The barrier for breaking the carbon-sulfur bond is very high with a transition state energy ~1eV higher than if the dissociative adsorption involves the Au crystal as discussed in the previous mechanism. Thus, in order for the reaction to occur at such a low temperature as is observed experimentally, Au must participate. Otherwise, there would be a need for an increased amount of thermal energy to drive the reaction forward. A second transition state is not available as the sulfur does not migrate to the surface in this pathway. As a result, the barrier to release CO is therefore ~0.33eV higher for the mechanism in which Au is not involved. Figure 5.11b shows the same reaction profile on an unsupported Mo_6S_8 cluster. The two energy pathways are identical. Since all of the sites on the free cluster are equivalent, there is only one possible mechanism for dissociation. Without

the local electronic environment of the Au surface for the sulfur atom to diffuse to, the cluster essentially acts as a free cluster.

5.4 Summary and Conclusions

In this work we have used a combination of experiment and DFT to study the interaction of OCS with the Mo_6S_8 cluster supported on Au(111). We observe a unique dissociation mechanism where the Au substrate directly helps to lower energetic barriers for the successful dissociation of OCS. The reactive surface was prepared by the deposition of *size-selected* $Mo_6S_8^+$ clusters onto a clean Au(111) surface under ultra high vacuum conditions. Thermal desorption studies of OCS on the bare Au(111) surface show no dissociation product, only a single low temperature peak (~125K) attributing to the adsorption of OCS on the surface. Once the clusters were deposited, two additional desorption peaks were observed, a CO (m/e = 28amu) peak denoting a dissociation event and another high temperature OCS peak indicating molecular desorption from the cluster. This provided evidence that the Mo_6S_8 cluster can adsorb OCS molecularly as well as induce OCS dissociation to form S-atoms that remain on the surface and gas-phase CO molecules. Repeated cycles of OCS adsorption and reaction, however, did not result in a loss of dissociation activity suggesting that the S-atoms do not bind to the Mo-atom sites of the cluster. Therefore, "poisoning" experiments were done to ensure that the reaction mechanism was occurring on the cluster itself and not on the Au(111) surface modified by the clusters. The blocking of the metal sites through CO adsorption verified that the clusters were the active sites for reaction as the OCS dissociation channel is completely suppressed when all of the metal sites are occupied. Density functional

theory was used to explore the reaction mechanism on the Au-supported cluster, and the lowest energy reaction path involves OCS dissociation at a Mo-atom side site with a barrier that is significantly smaller than that for the free cluster. The lowest energy pathway show that the S-atom migrates from the cluster to a three-fold hollow site on the Au(111) surface where it is most strongly bound with an energy of -3.54eV. Furthermore, when the dissociated sulfur atom was not bound to the Au crystal and was forced to remain on the cluster, the reaction pathway mimicked that of the free cluster indicating that the local electronic environment of the Au(111) crystal greatly enhances the dissociation process. The overall mechanism makes it possible for the Mo-active sites to be free from poisoning and therefore available for further catalysis. This is in good agreement with our experimental observations.

The reaction system described here highlights the unique interplay between the nanocatalyst particle and its support, and also represents a rare case in which both experiment and theory address precisely the same materials, i.e., cluster, substrate and reactant. The ability to apply ab initio electronic structure theory to experimental systems as complex as even a model catalyst system can provide the kind of insight into reaction mechanisms that is hard to extract from experiment alone.

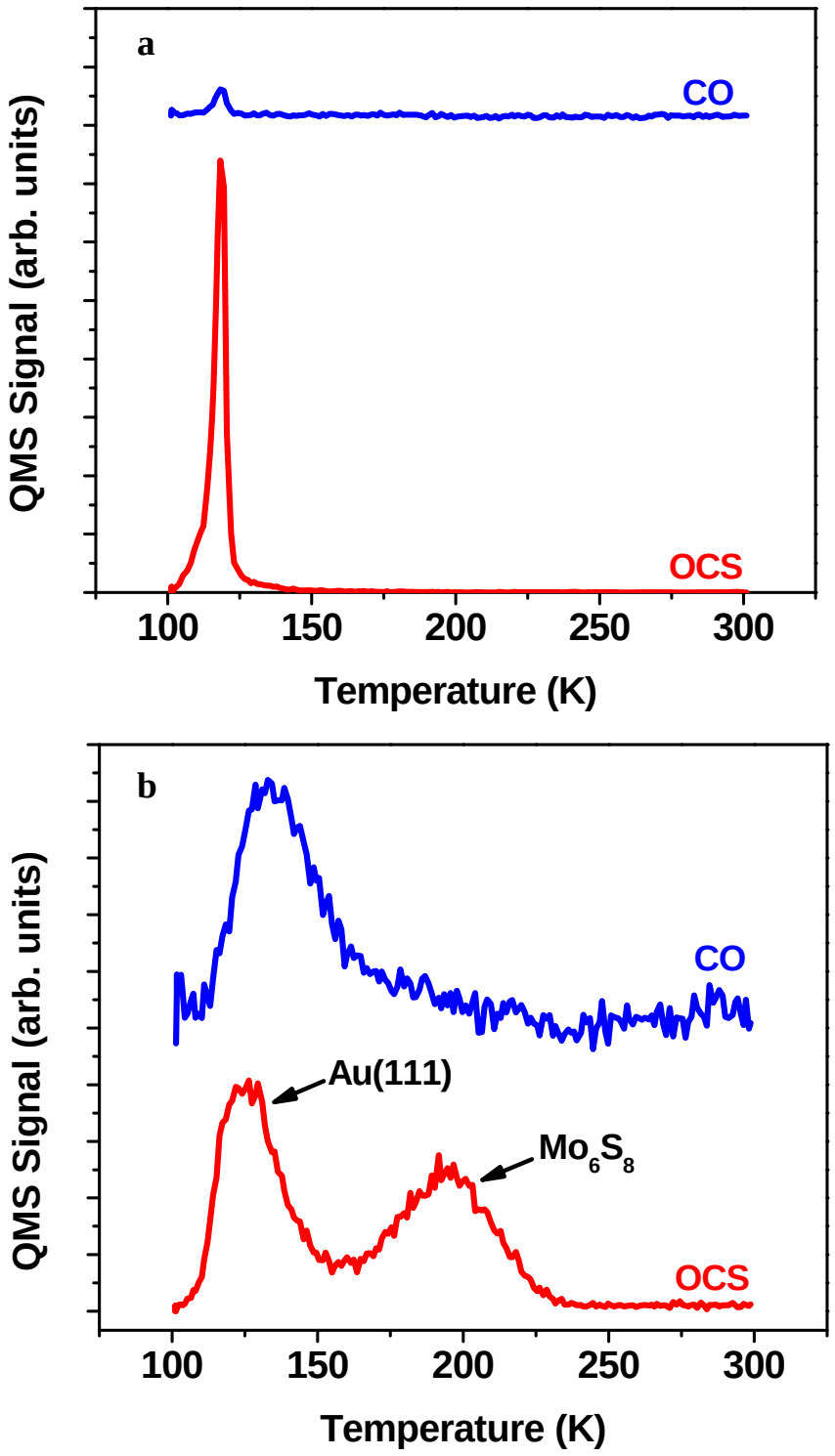

Figure 5.1: a) TPD spectra for OCS on bare Au(111) and b) TPD spectra for OCS on a 0.2ML coverage of Mo_6S_8 on Au(111). TPD was done with a directed doser with a backing pressure of 1 torr for 240s for bare Au and 90s for the supported cluster.

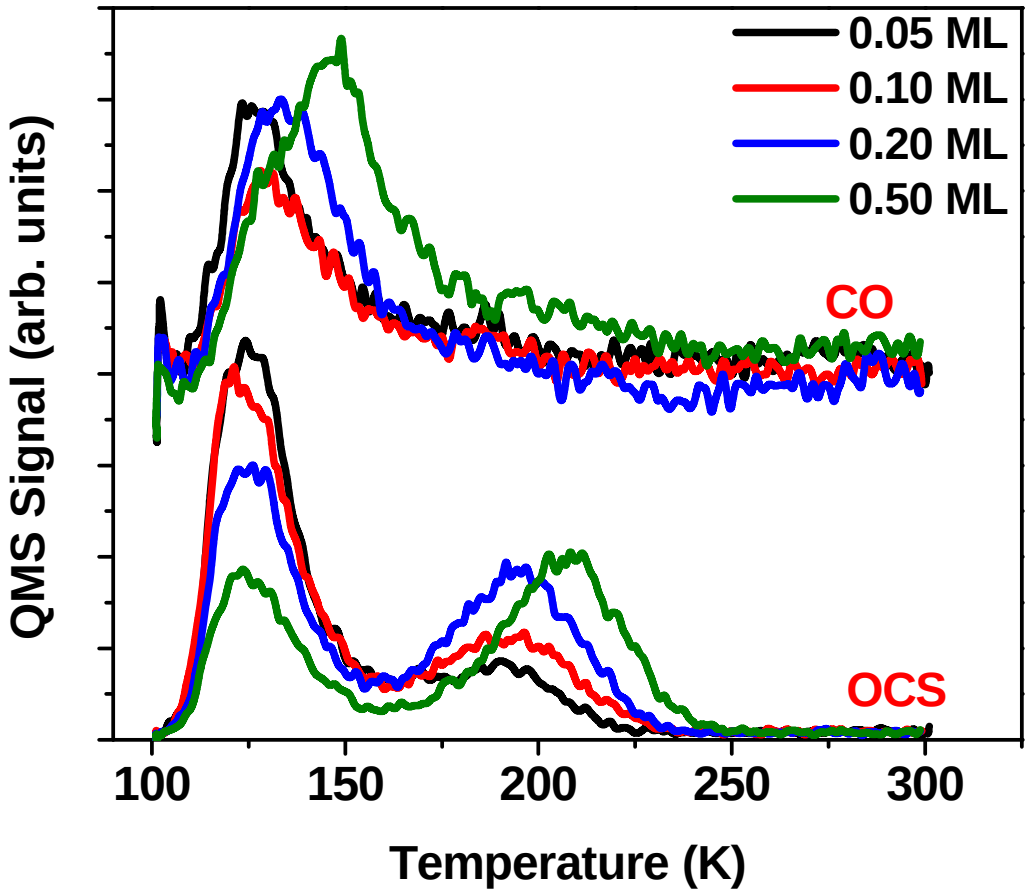

Figure 5.2: TPD spectra of OCS reaction cycle as a function of cluster coverage on a Au(111) surface. OCS TPD was done with a directed doser with a backing pressure of 1 torr for 90 seconds.

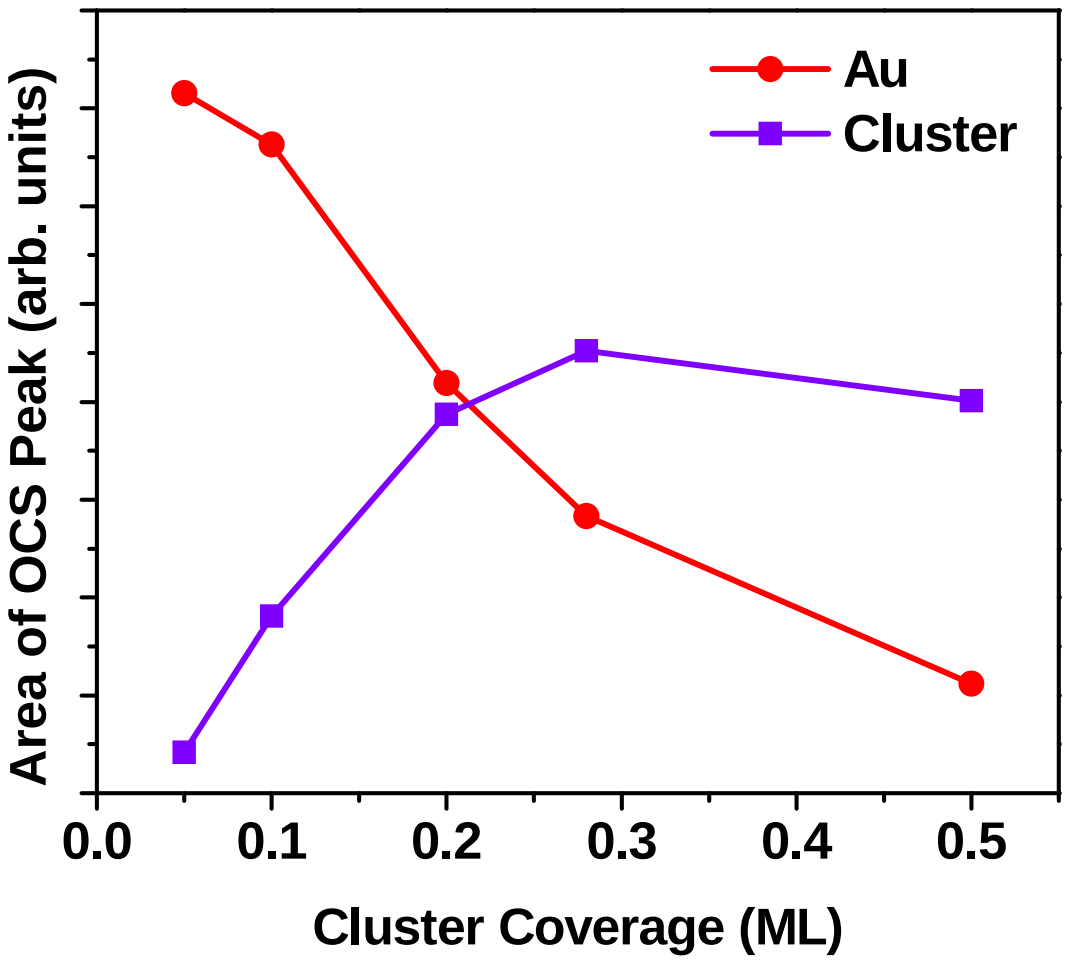

Figure 5.3: Plot displaying area of OCS desorption peak for Au and $Mo_6S_8^+$ as a function of cluster coverage.

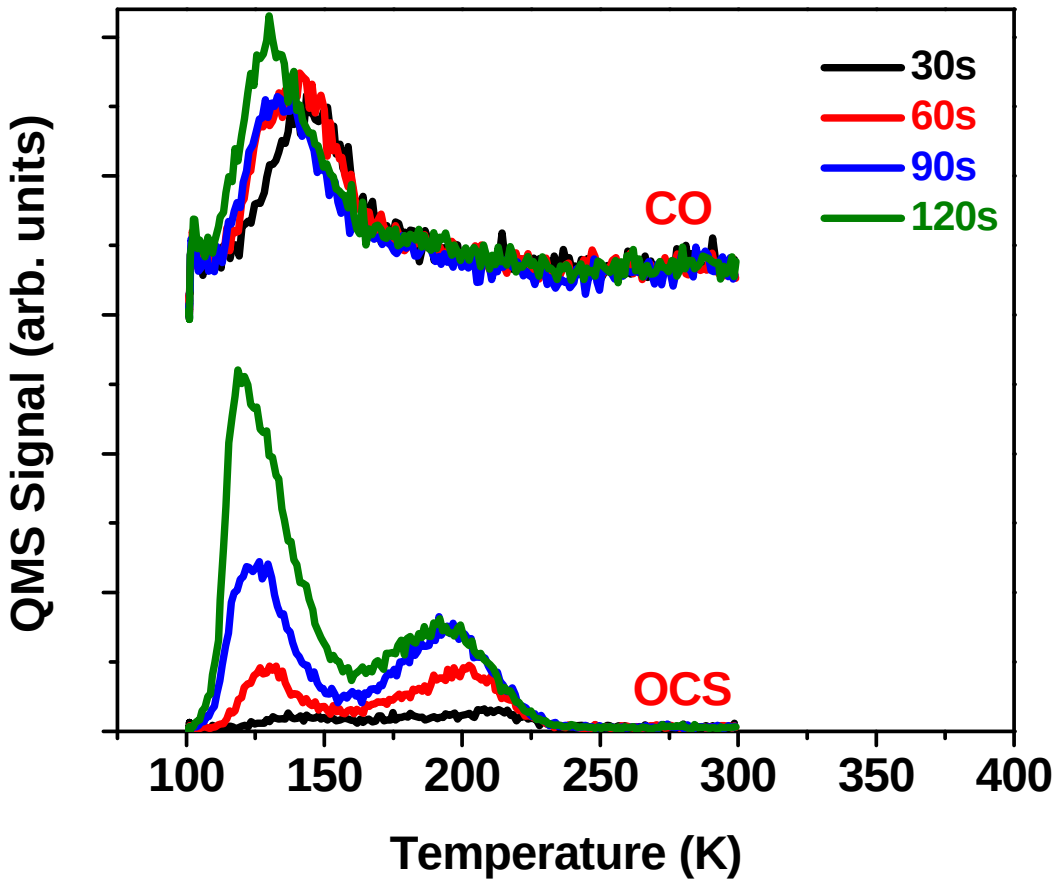

Figure 5.4: TPD spectra of OCS on 0.2ML of Mo_6S_8/Au(111) as a function of OCS exposure time. OCS TPD was done with a directed doser with a backing pressure of 1 torr for time indicated.

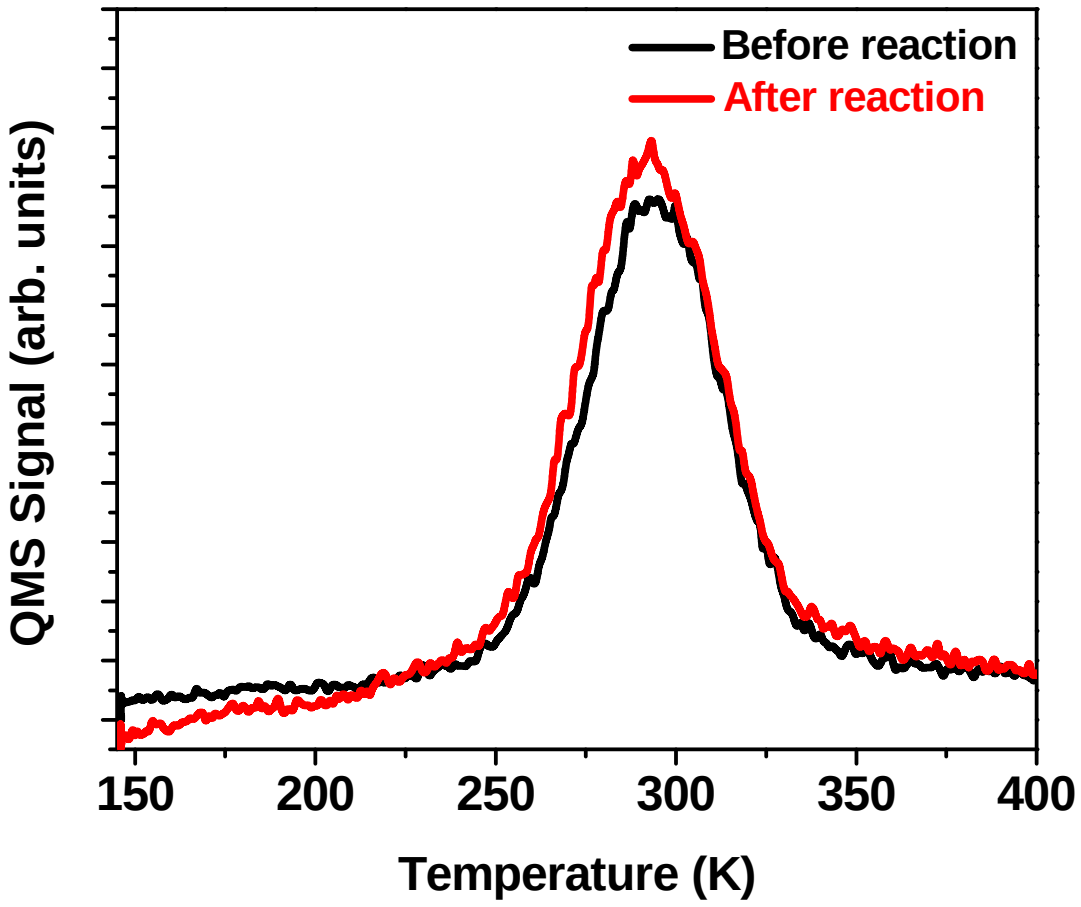

Figure 5.5: TPD spectra of ^{13}CO (saturated background dose) on 0.5ML of Mo_6S_8 on Au(111) before and after ~15 OCS reaction cycles.

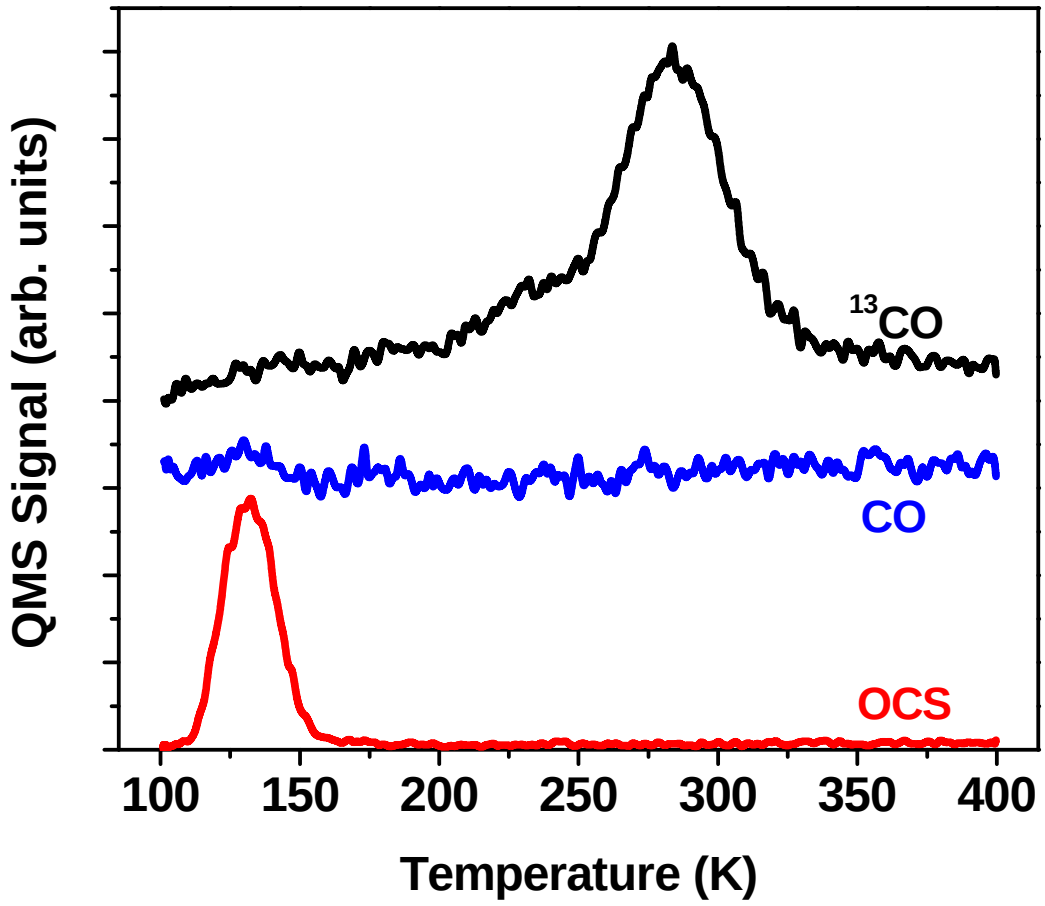

Figure 5.6: TPD "poisoning" experiment showing no reaction after pre-dosing the supported clusters with ^{13}CO prior to the OCS reaction cycle.

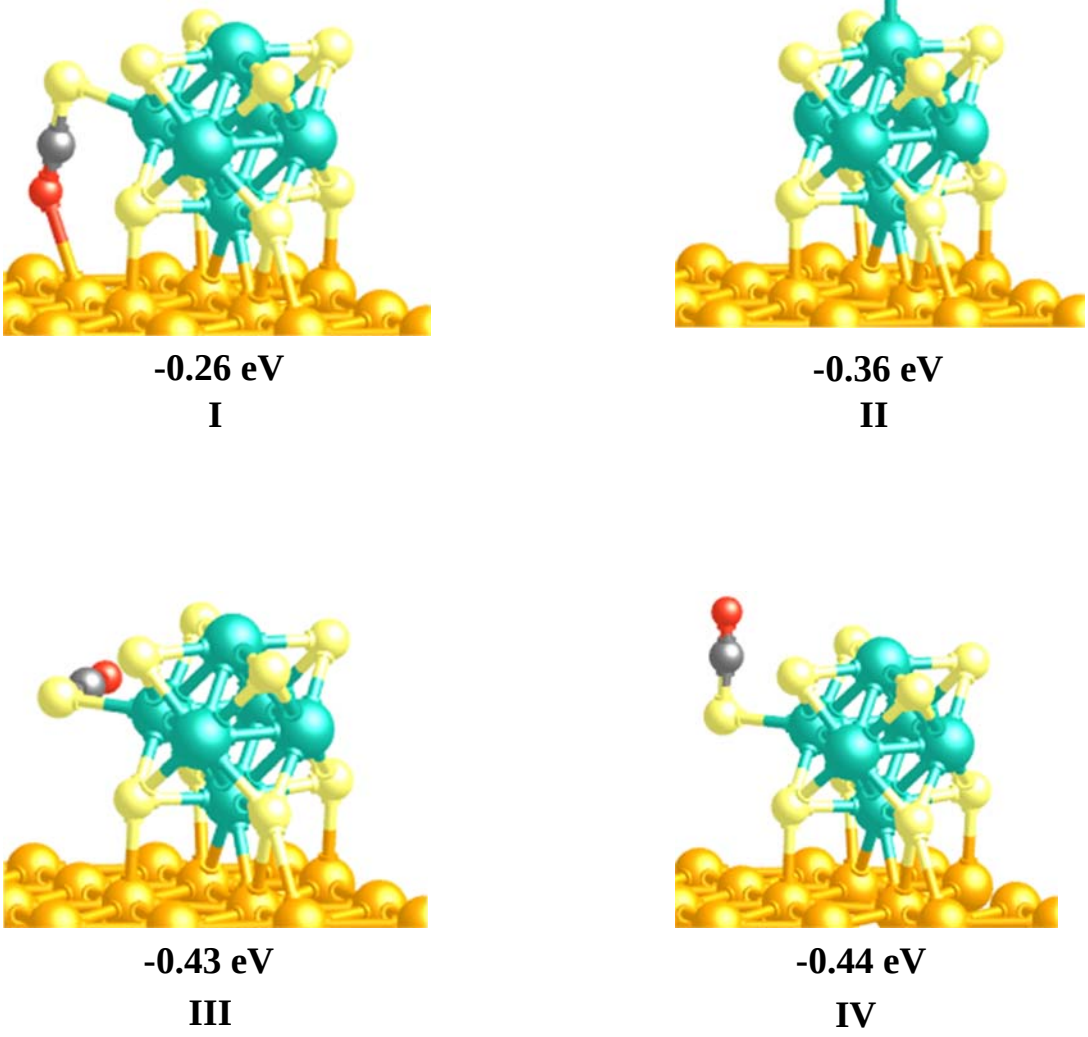

Figure 5.7: Schematic of optimized structures for the interaction of OCS with Mo_6S_8/Au(111).

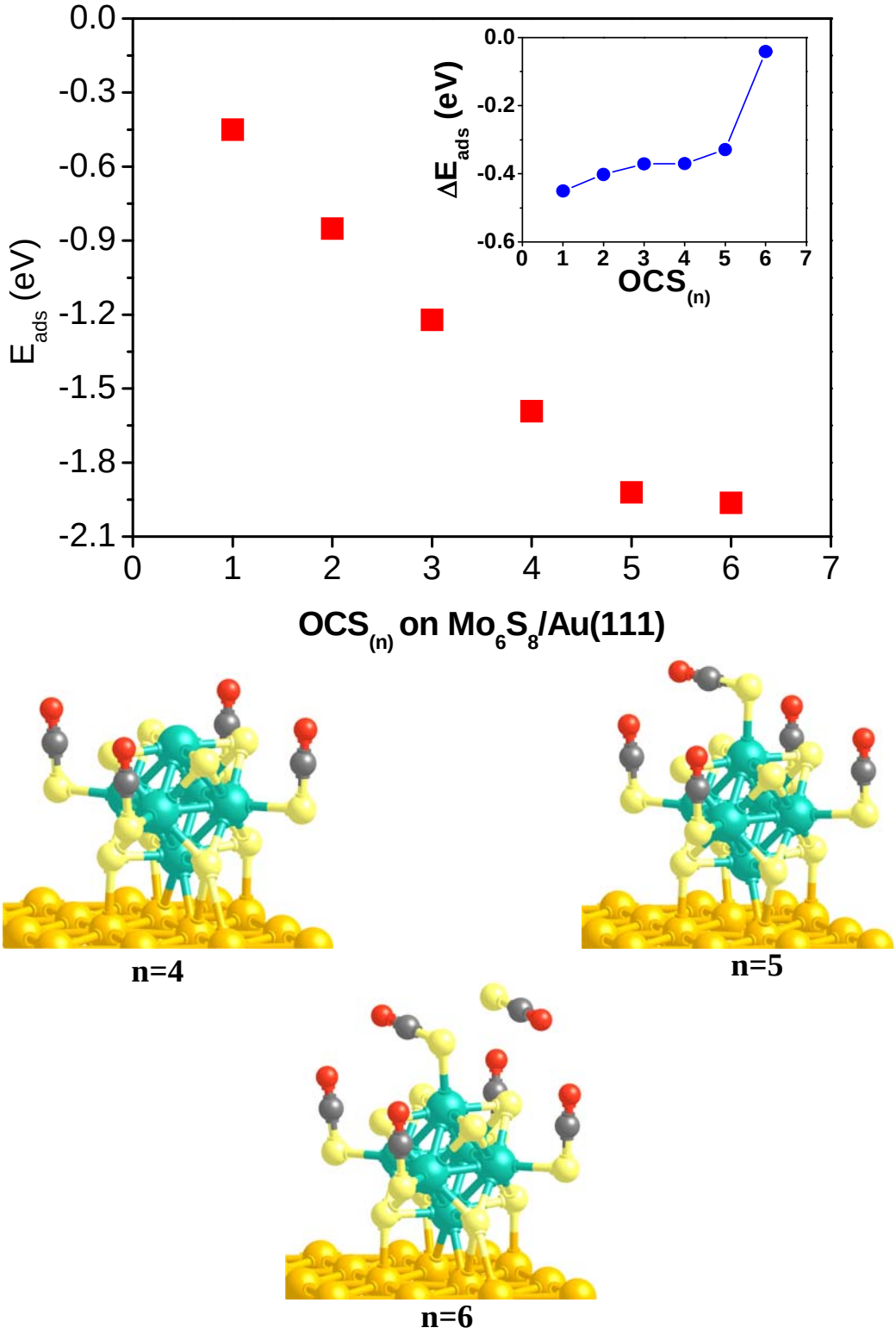

Figure 5.8: Total adsorption energy plot for the sequential addition of OCS on the Mo_6S_8/Au(111) system. Inset shows the binding energy for each OCS molecule. Also shown are the n=4, n=5, and n=6 configurations of the OCS/Mo_6S_8/Au(111).

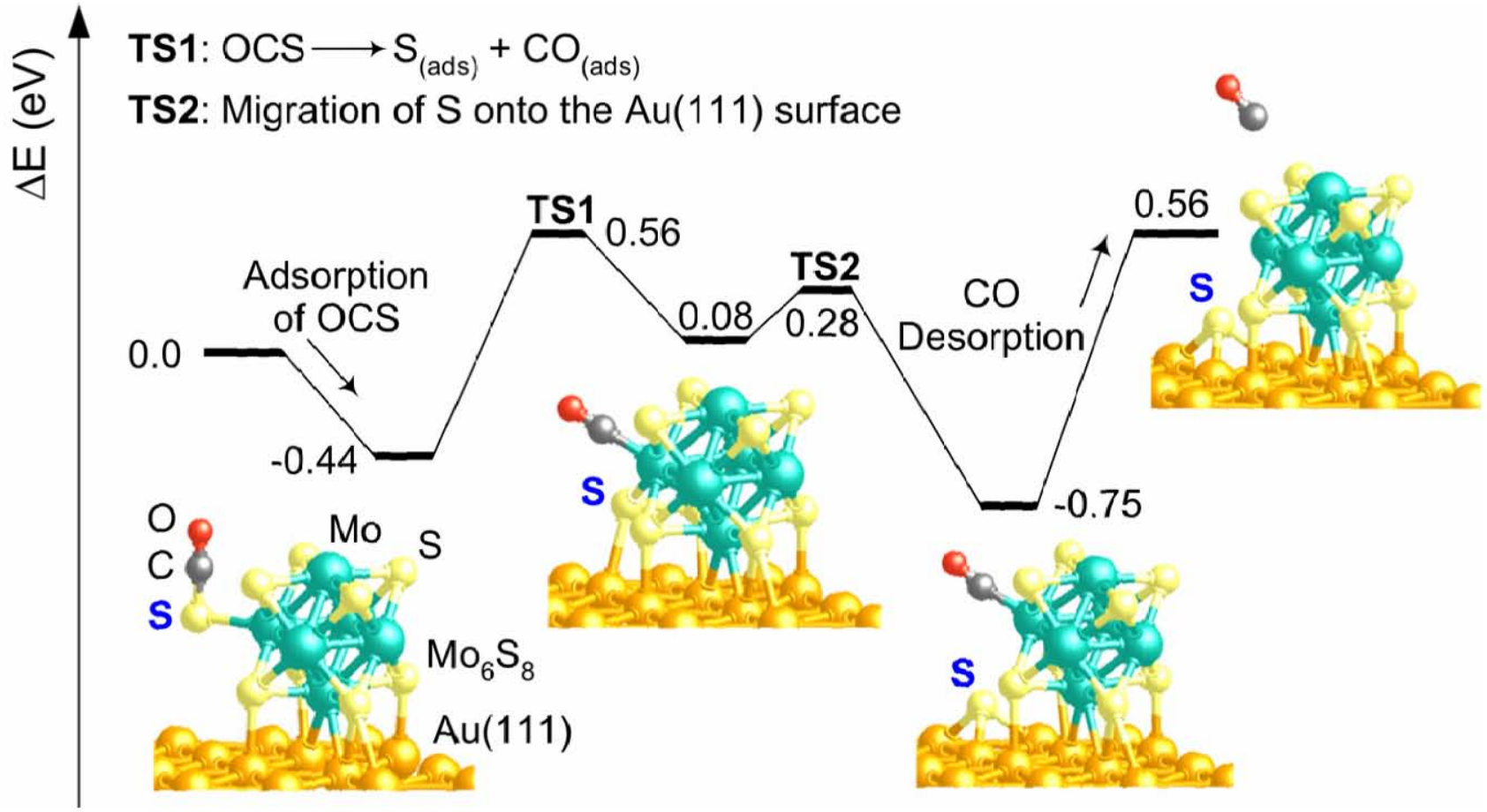

Figure 5.9: Energetically favorable potential energy profile for the dissociation of OCS on Mo_6S_8 on Au(111).

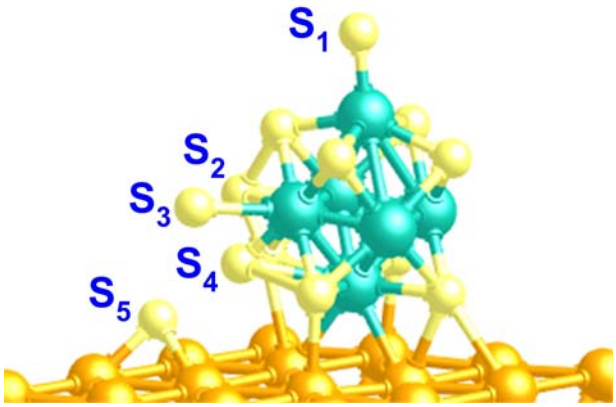

Figure 5.10: Schematic showing the possible sites for the dissociated sulfur species from the OCS reaction. The adsorption energies for S_1-S_5 are -3.00, -2.85, -3.18, -2.75, and -3.54eV respectively.

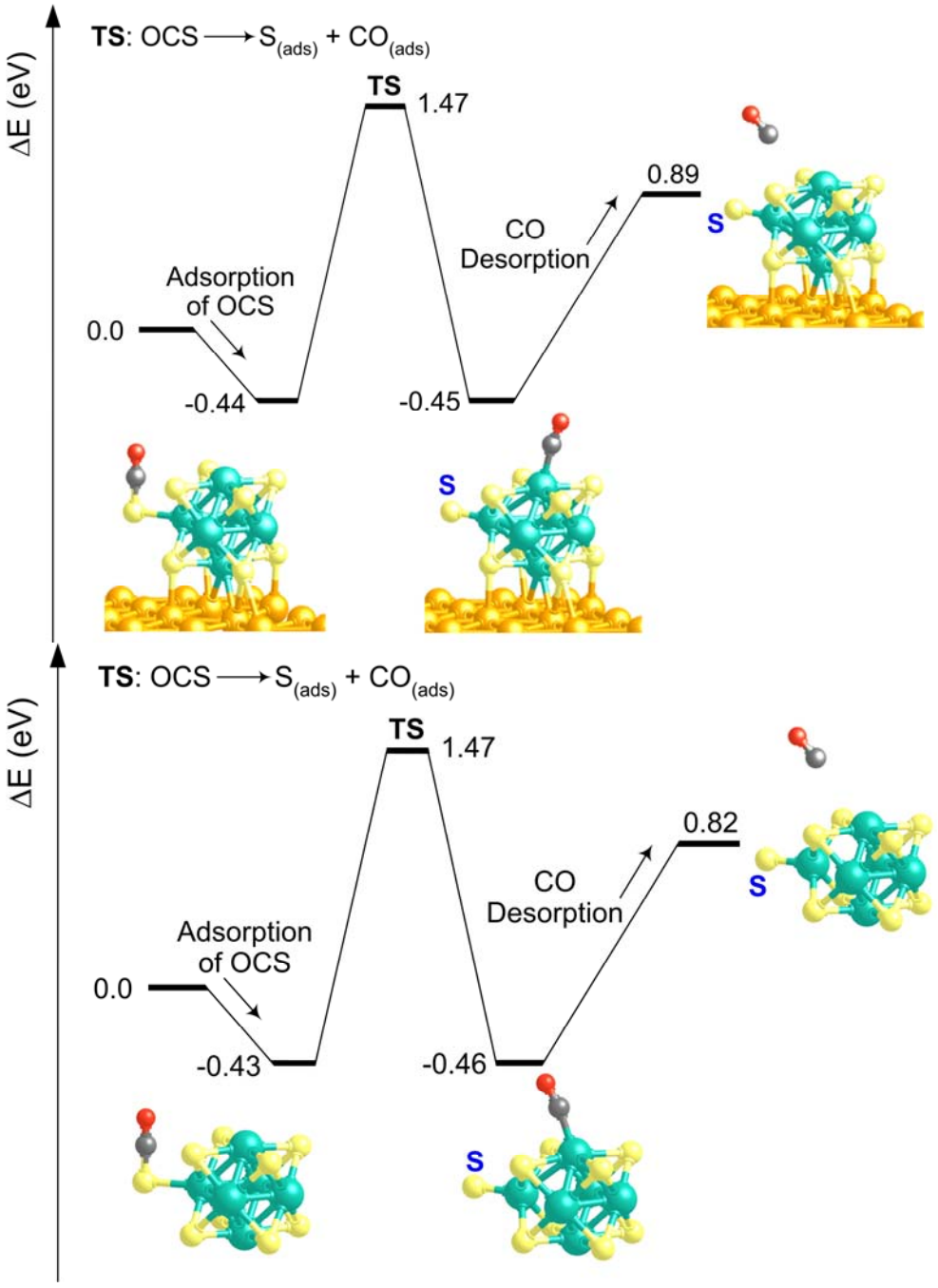

Figure 5.11: a) Potential energy profiles for the dissociation of OCS on (a) the Mo_6S_8 cluster supported on the Au(111) surface in which the resulting S-atom does not migrate to the Au surface and (b) the unsupported Mo_6S_8 cluster (all the Mo-sites are equivalent for adsorption and reaction of one OCS molecule).

Mulliken Population Analysis								
	Mo_6S_8/Au(111)		**Mo_6S_8**		**I**	**II**	**III**	**IV**
Mo	**Mo_{top}**	**Mo_{ss}**	**Mo_{top}**	**Mo_{ss}**				
	-1.41e	-1.21e	-1.41e	-1.21e	-1.28e	-1.43e	-1.28e	-1.28e
S	---		-1.99e		-1.52e	-1.37e	-1.75e	-1.38e
C	---		+0.05e		-0.42e	-0.57e	-0.21e	-0.61e
O	---		+1.94e		+1.98e	+1.91e	+1.95e	+1.97e

Table 5.1: Mulliken population charges for the structures shown in Figure 5.7 for the interaction of OCS on the Mo_6S_8/Au(111) system.

Bibliography

Aizawa, M.; Lee, S.; Anderson, S. L., "*Sintering , oxidation, and chemical properties of size-selected nickel clusters on TiO_2 (110).*" *Journal of Chemical Physics, 117*, 5001 (2002).

Andreev, T.; Barke, I.; Hovel, H., "*Adsorbed rare-gas layers on Au(111): Shift of the shockley surface state studied with ultraviolet photoelectron spectroscopy and scanning tunneling spectroscopy.*" *Physical Review B, 70,* 205426 (2004).

Bell, R. C.; Zemski, K. A.; Justes, D. R.; A. W. Castleman, J., "*Formation, structure and bond dissociation thresholds of gas-phase vanaium oxide cluster ions.*" *Journal of Chemical Physics, 114,* 798 (2001).

Bertram, N.; Kim, Y. D.; Gantefor, G.; Sun, Q.; Jena, P.; Tamuliene, J.; Seifert, G., "*Experimental and theoretical studies on inorganic magic clusters: M_4X_6 (M = W, Mo, X = O, S).*" *Chemical Physics Letters, 396,* 341 (2004).

Biener, M. M.; Biener, J.; Friend, C. M., "*Novel synthesis of two-dimensional TiS_2 nanocrystallites on Au(111).*" *Journal of Chemical Physics, 122,* 34706-1 (2005).

Binns, C., "*Nanoclusters Deposited on Surfaces.*" *Surface Science Reports, 44*, 1, (2001)

Blochl, P. E., "*Projector augmented-wave method*" *Physical Review B,50,* 17953 (1994).

Bollinger, M. V.; Lauritsen, J. V.; Jacobsen, K. W.; Norskov, J. K.; Helvig, S.; Besenbacher, F., "*One-dimensional metallic edge states in MoS_2.*" *Physical Review Letters, 87,* 196803-4 (2001).

Boyd, K. J.; Lapicki, A.; Aizawa, M.; Anderson, S. L., "*A phase-space-compressing, mass selecting beamline for hyperthermal, focused ion beam deposition*." *Review of Scientific Instruments, 69,* 4106 (1998).

Brandle, M.; Calzaferri, G.; Lanz, M., "*Size quantization and surface states of molybdenum sulphide clusters*." *Chemical Physics,201,* 141 (1995).

Busolt, U.; Cottancin, E.; Rohr, H.; Socaciu, L.; Leisner, T.; Woste, L., "*Cluster-surface interaction studied by time-resolved two-photon photoemission.*" *Applied Physics B, 68,* 453 (1999).

Chen, J.; Wu, F., "*Review of hydrogen storage in inorganic fullerene-like nanotubes.*" *Applied Physics A, 78,* 989 (2004).

Chhowalla, M.; Amaratunga, G. A. J., "*Thin films of fullerene-like MoS_2 nanoparticles with ultra-low friction and wear*." *Nature, 407,* 164 (2000).

Chourasia, A. R.; Chopra, D. R., Auger Electron Spectroscopy. In "*Handbook of I nstrumental Techniques for Analytical Chemistry"*, Settle, F. A., Ed. Prentice Hall: Upper Saddle River, 1997.

Dance, I. G., "*Understanding structure and eactivity of new fundamental inorganic molecules: metal sulfides, metallocarbohedrenes, and nitrogenase*." *Chemical Communications,5,* 523, (1998).

Dance, I. G.; Fischer, K. J.; Willett, G. D., "*Molecular mangenese sulfide clusters formed by laser ablation." Journal of the Chemical Society Dalton Transactions, 13,* 2557 (1997).

Dance, I. G.; Fisher, K. J.; Willett, G. D., "*Reactions of 29 Transition Metal Cations, in the Same Oxidation State and under the Same Gas-Phase Conditions, with Sulfur. Inorganic Chemistry, 35,* 4177 (1996).

Davidson, E. R.; Kunze, K. L.; Machado, F. B. C.; "*Chakravorty, S. J., The Transition Metal-Carbonyl Bond.*" *Accounts of Chemical Research, 26,* 628 (1993).

Delmon, B.; Froment, G. F., "*Remote control of catalytic sites by spillover species*." *Catalysis Reviews - Science and Engineering, 38,* 69 (1996)

Deng, H. T.; Kerns, K. P.; A. W. Castleman, "*Formation, Structures, and Reactivities of Niobium Oxide Clusters.*" *Journal of Physical Chemistry, 100,* 13386 (1996).

Deng, H. T.; Kerns, K. P.; Castleman A. W., "*Studies of Met-Car adducts: $Ti_8C_{12}^+(M)_n$ (M=Halogens, pi-bonding molecules, and polar molecules).*"*Journal of the American Chemical Society, 118*, 446 (1996).

Echt, O.; Sattler, K.; Recknagel, E., "*Magic Numbers for Sphere Packings: Experimental Verification in Free Xenon Clusters*." *Physical Review Letters, 47,* 1121 (1981).

Enyashin, A. N.; Gemming, S.; Bar-Sada, M.; Popovitz-Biro, R.; Hong, S. Y.; Prior, Y.; Tenne, R.; Sieffert, G., "*Structure and Stability of Molybdenum Sulfide Fullerenes*." *Angewandte Chemie International Edition, 47,* 623 (2007).

Feldman, Y.; Wasserman, E.; Srolovitz, D. J.; Tenne, R., "*High Rate, Gas-Phase Growth of MoS2 Nested Inorganic Fullerenes and Nanotubes*." *Science, 267*, 222 (1995).

France, C. B.; Parkinson, B. A., "*Physical and electronic structure of p-sexiphenyl on Au(111)*." *Applied Physics Letters, 82,* 1194 (2003).

Gemming, S.; Seifert, G., "*Density-functional study of Mo_4S_6 on Au(111)*." *Applied Physics A, 82,* 175 (2005).

Gemming, S.; Seifert, G., "*Novel Elongated Molybdenum Sulfide Nanostructures*." *AIP Conference Proceedings, 786,* 353 (2005).

Gemming, S.; Tamuliene, J.; Seifert, G.; Bertram, N.; Kim, Y. D.; Gantefor, G., "*Electronic and geometric structures of Mo_xS_y and W_xS_y (x = 1,2,4; y = 1-12) clusters*." *Applied Physics A, 82,* 161 (2005).

Gerlich, D., "*State-Selected and State-toState Ion-Molecule Reaction Dynamics, Part 1: Experiment. In Advances in Chemical Physics Series, Vol. LXXXII.*" Ng, C. Y.; Baer, M., Eds. John Wiley & Sons, Inc.: New York, 1992.

Guo, B. C.; Kerns, K. P.; A. W. Castleman, Jr., "*Reactivities of $Ti_8C_{12}^+$ at thermal energies*." *Journal of the American Chemical Society, 115,* 7415 (1993).

Guo, B. C.; Kerns, K. P.; Castleman, A. W., "*Chemistry and kinetics of size-selected colbalt cluster cations at thermal energies. I. Reactions with CO*." *Journal of Chemical Physics, 96,* 8177 (1992).

Guzowski, J. P., Jr.; Hieftje, G. M., "*Characteristics of a rf-only hexapole ion-guide interface for plasma-source time-of flight mass spectrometry*." *Journal of Analytical Atomic Spectroscopy, 16,* 781 (2001).

Haberland, H.; Insepov, Z.; Moseler, M., "*Molecular-dynamics simulation of thin-film growth by energetic cluster impact*." *Physical Review B, 51,* 11061 (1995).

Haberland, H.; Karrais, M.; Mall, M.; Thurner, Y., "*Thin films from energetic cluster impact: A feasibility study*." *Journal of Vacuum Science and Technology A, 10,* 3266 (1992).

Haberland, H.; Mall, M.; Moseler, M.; Qiang, Y.; Reiners, T.; Thurner, Y., "*Filling of micron-sized contat holes with copper by energetic cluster impact*." *Journal of Vacuum Science and Technology A., 12,* 2925 (1994).

Hadjikyriacou, A. I.; Coucouvanis, D., "*New Members of the $[Mo_2(S)_n\ (S_2)_{6-n}]^{2-}$ Series. Synthesis, Structural Characterization, and Properties of the $[Mo_2S_9]^{2-}$, $[Mo_2S_7]^{2-}$, and $[Mo_2S_6]^{2-}$ Thio Anions*." *Inorganic Chemistry, 26,* 2400 (1987).

Hammer, B.; Morikawa, Y.; Norskov, J. K., "*CO Chemisorption at Metal Surfaces and Overlayers*." *Physical Review Letters, 76,* 2141 (1996).

He, S.-G.; Xie, Y.; Guo, Y.; Bernstein, E., "*Formation, detection, and stability studies of neutral vanadium sulfide clusters*." *The Journal of Chemical Physics, 126,* 194315 (2007).

Heiz, U.; Schneider, W., "*Nanoassembled model catalysts*." *Journal of Physics - D Applied Physics, 33,* R85 (2000).

Heiz, U.; Vanolli, F.; Trento, L.; Schneider, W.-D., "*Chemical reactivity of size-selected supported clusters: an experimental setup*." *Review of Scientific Instruments, 68,* 1986 (1997).

Helveg, S.; Lauristen, J. V.; Laegsgaard, E.; Stensgaard, I.; Norskov, J. K.; Clausen, B. S.; Toposoe, H.; Besenbacher, F., "*Atomic-Scale Structure of Single-Layer Mo_2 Nanoclusters." Physical Review Letters, 84,* 951 (2000).

Hibble, S. J.; Feaviour, M. R.; Almond, M. J., "*Chemical excision from amorphous MoS_3; a quantitative EXAFS study*." *Dalton Transactions, 6,* 935 (2001).

Horn, J. M.; Song, Z.; Potapenko, D. V.; Hrbek, J.; White, M. G., "*Characterization of Molybdenum Carbide nanopraticles Formed on Au(111) using Reactive-Layer Assisted Deposition*." *Journal of Physical Chemistry, 109,* 44 (2004).

Hrbek, J.; Hwang, R. Q., Interaction of adsorbates on strained metallic layers. *Current Opinion in Solid State and Materials Science* **2001,** 5, 67.

Huang, J. M.; Laitinen, R. A.; Kelley, D. F., "*Spectroscopy and dynamics of WS_2 nanoclusters." Physical Review B, 62,*10995 (2000).

Jones, R. M.; Anderson, S. L., "*Simplified radio-frequency generator for driving ion guides, traps, and other capacitive loads*." *Review of Scientific Instruments, 71,* 4335 (2000).

Klabunde, K. J.; Mulukutla, R. S., "Chemical and Catalytic Properties of Nanocrystals. In *Nanoscale Materials in Chemistry*, Klabunde, K. J., Ed. John Wiley and Sons: 2001; p 223.

Knight, W. D.; Clemenger, K.; Heer, W. A. d.; Saunders, W. A.; Chou, M. Y.; Cohen, M. L., "*Electronic Shell Stucture and Abundances of Sodium Clusters*." *Physical Review Letters, 53,* 2141 (1984)

Koelling, D. D.; Harmon, B. N., "*A technique for relativistic spin-polarised calculations." Journal of Physical Chemistry C: Solid State Physics, 10,* 3107 (1977).

Kresse, G.; Furthmuller, J., "*Efficient iterative schemes for ab initio total-energy calculations using a plane-wave basis set.*" *Physical Review B, 54,* 11169 (1996).

Kresse, G.; Hafner, J., "*Ab inito molecular dynamics for liquid metals*." *Physical Review B, 47,* 558 (1993).

Lauritsen, J. V.; Bollinger, M. V.; Laegsgaard, E.; Jacobsen, K. W.; Norskov, J. K.; Clausen, B. S.; Topsoe, H.; Besenbacher, F., "*Atomic-scale insight into structure and morphology changes of MoS_2 nanoclusters in hydrotreating catalysts*." *Journal of Catalysis, 221,* 510 (2004).

Lauritsen, J. V.; Kibsgaard, J.; Helvig, S.; Clausen, B. S.; Topsoe, H.; Laegsgaard, E.; Besenbacher, F., "*Size-Dependent Structure of MoS_2 Nanocrystals*." *Nature, 2,* 53 (2007).

Lauritsen, J. V.; Nyberg, M.; Norskov, J. K.; Clausen, B. S.; Topsoe, H.; Laegsgaard, E.; Besenbacher, F., "*Hydrodesulfurization Reaction Pathways on MoS_2 Nanocluster Revealed by Scanning Tunneling Microscopy*." *Journal of Catalysis, 224,* 94 (2004).

Lauritsen, J. V.; Nyberg, M.; Vang, R. T.; Norskov, J. K.; Clausen, B. S.; Topsoe, H.; Laegsgaard, E.; Besenbacher, F., "*Chemistry of one-dimensional metallic edge states in MoS_2 nanoclusters*." *Nanotechnology, 14,* 385 (2003).

Lauritsen, J. V.; Vang, R. T.; Besenbacher, F., "*From atom-resolved scanning tunneling microscopy STM studies to the design of new catalysts*." *Catalysis Today, 111,* 34 (2006).

Leskiw, B. D.; A. W. Castleman, J., "*Met-Cars: A Unique Class of Molecular Solids". C. R. Physique, 3,* 251 (2002).

Leuchtner, R. E.; Harms, A. C.; A. W. Castleman, J., "*Metal cluster cation reactions: Carbon monoxide association to Cu_n^+ ions*." *Journal of Chemical Physics, 92,* 6527 (1989).

Lightstone, J. M.; Mann, H. A.; Wu, M.; Johnson, P.; White, M. G., "*Gas-Phase Production of Molybdenum Carbide, Nitride, and Sulfide clusters and Nanocrystallites." Journal of Physical Chemistry B, 107,* 10359 (2003).

Lightstone, J. M.; Patterson, M.; White, M. G., "*Gas Phase Reactivity of the $Ti_8C_{12}^+$ Met-Car with Tri-Atomic Sulfur Containing Molecules: CS_2, SCO, and SO_2.*" *Journal of Physical Chemistry A, 110,* 3505 (2006).

Lightstone, J. M.; Patterson, M. J.; Liu, P.; J. C. Lofaro, J.; White, M. G., "*Characterization and Reactivity of the $Mo_4S_6^+$ Cluster Deposited on Au(111).*" *Journal of Physical Chemistry C, 112,*11495 (2008).

Lightstone, J. M.; Patterson, M. J.; White, M. G., "*Reactivity of the $M_4S_6^+$ (M=Mo, W) cluster with CO and NH3 in the gas-phase: An experimental and DFT study*." *Chemical Physics Letters, 413,* 429 (2005).

Liu, P.; Rodriguez, J. A.; Muckerman, J. T.; Hrbek, J., "*The deposition of Mo nanoparticles on Au(111) from $Mo(CO)_6$.*" *Surface Science, 530*, L313 (2003).

Llusar, R.; Uriel, S.; Vicent, C.; Clemente-Juan, J. M.; Coronado, E.; Gomez-Garcia, C. J.; Braida, B.; Canadell, E., "*Single-Component Magnetic Conductors Based on Mo_3S_7 Trinuclear Clusters with Outer Dithiolate Ligands*." *Journal of the American Chemical Society, 126,* 12076 (2004).

Loh, S. K.; Hales, D. A.; Lian, L.; Armentrout, P. B., "*Collision-induced dissociation of Fe_n^+ (n=2-10) with Xe: Ionic and neutral iron binding energies*." *Journal of Chemical Physics, 90,* 5466 (1989),

Mahaffy, P. R.; Lai, K., "*An electrostatic quadrupole deflector for mass spectrometer applications*." *Journal of Vacuum Science and Technology A, 8,* 3244 (1990).

Mancour-Billah, A.; Chevrel, R., "*A new increasing delocalization of M = 3d-elements (Ti,Fe,Co) in the channels network of ternary $M_yMo_6Se_8$ Chevrel Phases*."*Journal of Solid State Chemistry, 170,* 281 (2003).

Martin, T. P.; Bergmann, T.; Gohlich, H.; Lange, T., "*Observation of electronic shells and shells of atoms in large Na clusters*." *Chemical Physics Letters, 172,* 209 (1990).

Monkhorst, H. J.; Pack, J. D., "*Special points for brillouin-zone integrations" Physical Review B, 13,* 5188 (1976)

Moore, J. H.; Davis, C. C.; Coplan, M. A., *Building Scientific Apparatus: A Practical Guide to Design and Construction*. Perseus Books Group: Cambridge, 2002.

Muller, A.; Sarkar, S.; Bhattacharyya, R. G.; Pohl, S.; Dartman, M., "*Directed Synthesis of the $[Mo_3S_{13}]^{2-}$, an Isolated Cluster Containing Sulfur Atoms in Three Differeent States of Bonding*." *Angewandte Chemie International Edition, 17,* 535 (1978).

Murugan, P.; Kumar, V.; Kawazoe, Y.; Ota, N., "*Ab initio Study of Structural Stability of Mo-S Clusters and Size Specific Stoichiometries of Magic Clusters*." *Journal of Physical Chemistry A, 111,* 2778 (2007).

Murugan, P.; Kumar, V.; Kawazoe, Y.; Ota, N., "*Atomic structures and magnetism in small MoS_2 and WS_2 Clusters*." *Physical Review A, 71,* 063203 (2005).

Nakat, J. E.; Fisher, K. J.; Dance, I. G.; Willet, G. D., "*Gas Phase Metal Chalcogenide Cluster Ions: A New $[Co_xS_y]^-$ Series Up to $[Co_{38}S_{24}]^-$ and Two $[Fe_xS_y]^-$ Series*." *Inorganic Chemistry, 32,* 1931 (1993).

Nakat, J. H. E.; Dance, I. G.; Fischer, K. J.; Rice, D.; Willett, G. D., "*Laser Ablation FTICR Mass Spectrometry of Metal Sulfides*." *Journal of the American Chemical Society, 113,* 5141 (1991).

Nayak, S. K.; Jena, P.; Stepanyuk, V. S.; Hergert, W.; Wildberger, K., "*Magic Numbers in supported metal clusters*." *Physical Review B, 56,* 6952 (1997).

Orita, H.; Uchida, K.; Itoh, N., "*Adsorption on thiophene on an MoS_2 cluster model catalyst*." *Journal of Molecular Catalysis A: Chemical, 193,* 197 (2003).

Orita, H.; Uchida, K.; Itoh, N., "*A volcano-type relationship between the adsorption energy of thiophene on promotoed MoS_2 cluster-model catalsts and the exprimental HDS activity*." *Applied Catalysis A: General, 258,* 115 (2004).

Parilla, P. A.; Dillion, A. C.; Parkinson, B. A.; Jones, K. M.; Alleman, J.; Riker, G.; Ginley, D. S.; Heben, M. J., "*Formation of Nanooctahedra in Molybdenum Disulfide and Molybdenum DiSelenide Using Pulsed Laser Vaporization*." *Journal of Physical Chemistry B, 108,* 6197 (2004).

Paskach, T. J.; Hilsenbeck, S. J.; Thompson, R. K.; McCarley, R. E.; Schrader, G. L., "*Synthesis and characterization of a novel platinum molybdenum sulfide containing the Mo_6S_8 cluster*." *Journal of Alloys and Compounds, 311,* 169 (2000).

Paskach, T. J.; Schrader, G. L.; McCarley, R. E., "*Synthesis of methanethiol from methanol over reduced molybdenum sulfide catalysts based on the Mo_6S_8 cluster*." *Journal of Catalysis, 211,* 285 (2002).

Patterson, M. J.; Lightstone, J. M.; White, M. G., "*Structure of Molybdenum and Tungsten Sulfide $M_xS_y^+$ Clusters: Experiment and DFT Calculations*." *Journal of Physical Chemistry A, 112,* 12011 (2008).

Perdew, J. P.; Erzerhof, M., *"Generalized Gradient Approximation Made Simple" Physical Review Letters, 77,* 3865 (1996).

Popov, I.; Gemming, S.; Seiffert, G., "*Structural and electronic properties of Mo_6S_8 clusters deposited on Au(111) surface investigate by density functional theory*." *Physical Review B, 75,* 245436 (2007).

Popov, I.; Kunze, T.; Gemming, S.; Seifert, G., "*Self-assembly of Mo_6S_8 clusters on the Au(111) surface*." *European Physical Journal D: Atomic, Molecular, Optical and Plasma Physics, 45,* 439 (2007).

Potapenko, D. V.; Horn, J. M.; Beuhler, R. J.; Song, X.; White, M. G., "*Reactivity studies with gold supported Mo nanoparticles*." *Surface Science, 574,* 244 (2005).

Potapenko, D. V.; Horn, J. M.; White, M. G., "*The reactions of cyclohexene on Au(111)-supported molybdenum carbide nanoparticles*." *Journal of Catalysis, 236,* 346 (2005).

Powell, C. J.; Jablonski, A. *NIST ElectronEffective-Attenuation-Lenght Database Version 1.1*, National Institute of Standards and Technology: Gaithersburg, 2003.

Prins, R.; Beer, V. H. J. d.; Somorjai, G. A., "*Structure and function of the catalyst and the promoter in Co-Mo hydrodesulfurization catalysts" Catalysis Reviews - Science and Engineering, 31,* 1 (1989).

Rapoport, L.; Bilik, Y.; Feldman, Y.; Homyonfer, M.; Cohen, S. R.; Tenne, R., "*Hollow nanoparticles of WS2 as potential solid-state lubricants*." *Nature, 387,* 791 (1997).

Rodriguez, J. A.; Dvorak, J.; Jirsak, T.; Hrbek, J., "*Formation of Mo and MoS_x nanoparticles on Au(111) from $Mo(CO)_6$ and S_2 precursors; electronic and chemical properties*." *Surface Science, 490,* 315 (2001).

Seifert, G.; Kohler, T.; Tenne, R., "*Stability of Metal Chalcogenide Nanotubes*." *Journal Physical Chemistry B, 106,* 2497 (2002).

Seifert, G.; Tamuliene, J.; Gemming, S., "*Mo_nS_{2n+x} clusters-magic numbers and platelets*."*Computational Materials Science, 35,* 316 (2006).

Song, Z.; Cai, T.; Rodriguez, J. A.; Hrbek, J.; Chan, A. S. Y.; Friend, C. M., "*A Novel Growth Mode of Mo on Au(111) from a $Mo(CO)_6$ Precursor: An STM Study*." *Journal of Physical Chemistry B, 107,* 1036 (2003).

Speight, J. G., *The Chemistry and Technology of Petroleum*. second ed.; McGraw-Hill: New York, 1991.

Tanner, S. D.; Baranov, V. I., "*Theory design and operation*." *Atomic Spectroscopy, 20,* 45 (1990).

Tenne, R., "*Fullerene-like materials and nanotubes from inorganic compounds with a layered (2-D) structure*." *Colloids and Surfaces, 208,* 83 (2002).

Tenne, R., "*Inorganic Nanotubes and Fullerene-Like Materials*." *Chemistry- A European Journal, 8,* 5296 (2002).

Thomas, M.; Dickinson, J. T.; Poppa, H.; Pound, G. M., "*Chemisorption of CO on Pd particles supported on mica." Journal of Vacuum Science and Technology, 15,* 568 (1978).

Thurston, T. R.; Wilcoxon, J. P., "*Photooxidation of Organic Chemicals Catalyzed by Nanoscale MoS_2." Journal of Physical Chemistry B, 103,* 11 (1998).

Topsoe, H.; Clausen, B. S.; Massoth, F. E., *Hydrotreating Catalysts: Catalysis-Science and Technology*. Springer-Verlag: Berlin-Heidelberg, 1996; Vol. 11.

Travert, A.; Dujardin, C.; Mauge, F.; Cristol, S.; Paul, J. F.; Payen, E.; Bougeard, D., "*Parallel between infrared characterization and ab initio calculations of CO adsorption on sulfided Mo catalysts*." *Catalysis Today, 70,* 255 (2001).

Umarji, A. M.; Rao, G. V. S.; Janawadkar, M. P.; Radhakrishnan, T. S., "*Metal atom incorporation studies on $A_xMo_6S_8$ chevrel phases*." *Journal of Physics and Chemistry of Solids, 41,* 421 (1980).

Vajda, S.; Wolf, S.; Leisner, T.; Busolt, U.; Woste, L. H., "*Reaction of size-selected positively charged nickel clusters with carbon monoxide in molecular beams*." *Journal of Chemical Physics, 107,* 3492 (1997).

Vandoni, G.; Felix, C.; Goyhenex, C.; Monot, R.; Buttet, J.; Harbich, W., "*The fate of mass selected silver clusters deposited on Pd(100)." Surface Science, 838,* 331 (1985).

Woodruff, D. P.; Delchar, T. A., *Modern techniques of surface science*. Cambridge University Press: Cambridge, 1986.

Zeng, T.; Wen, X.-D.; Li, Y.-W.; Jiao, H., "*Density Functional Theory Study of Triangular Molybdenum Sulfide Nanocluster and CO Adsorption on It*." *Journal of Physical Chemistry B, 109,* 13704 (2005).

Zeng, T.; Wen, X.-D.; Wu, G.-S.; Li, Y.-W.; Jiao, H., "*Density Functional Theory Study of CO Adsorption on Molybdenum Sulfide*." *Journal of Physical Chemistry B, 109,* 2846 (2005).

Zhang, N.; Yu, Z.; Wu, X.; Gao, Z.; Zhu, Q.; Kong, F., "*Formation and photolysis of tantalum sulfide cluster ions." Journal of the Chemical Society, Faraday Transactions, 89,* 1779 (1993).

References

(1) Feldman, Y.; Wasserman, E.; Srolovitz, D. J.; Tenne, R. *Science* **1995**, *267*, 222.

(2) Tenne, R. *Chemistry- A European Journal* **2002**, *8*, 5296.

(3) Tenne, R. *Colloids and Surfaces* **2002**, *208*, 83.

(4) Seifert, G.; Kohler, T.; Tenne, R. *Journal of Physical Chemistry B* **2002**, *106*, 2497.

(5) Parilla, P. A.; Dillion, A. C.; Parkinson, B. A.; Jones, K. M.; Alleman, J.; Riker, G.; Ginley, D. S.; Heben, M. J. *Journal of Physical Chemistr B* **2004**, *108*, 6197.

(6) Enyashin, A. N.; Gemming, S.; Bar-Sada, M.; Popovitz-Biro, R.; Hong, S. Y.; Prior, Y.; Tenne, R.; Sieffert, G. *Angewandte Chemie International Edition* **2007**, *46*, 623.

(7) Rapoport, L.; Bilik, Y.; Feldman, Y.; Homyonfer, M.; Cohen, S. R.; Tenne, R. *Nature* **1997**, *387*, 791.

(8) Thurston, T. R.; Wilcoxon, J. P. *Journal of Physical Chemistry B* **1998**, *103*, 11.

(9) Chhowalla, M.; Amaratunga, G. A. J. *Nature* **2000**, *407*, 164.

(10) Chen, J.; Wu, F. *Applied Physics A* **2004**, *78*, 989.

(11) Topsoe, H.; Clausen, B. S.; Massoth, F. E. *Hydrotreating Catalysts: Catalysis-Science and Technology*; Springer-Verlag: Berlin-Heidelberg, 1996; Vol. 11.

(12) Brandle, M.; Calzaferri, G.; Lanz, M. *Chemical Physics* **1995**, *201*, 141.

(13) Orita, H.; Uchida, K.; Itoh, N. *Journal of Molecular Catalysis A: Chemical* **2003**, *193*, 197.

(14) Orita, H.; Uchida, K.; Itoh, N. *Applied Catalysis A: General* **2004**, *258*, 115.

(15) Zeng, T.; Wen, X.-D.; Wu, G.-S.; Li, Y.-W.; Jiao, H. *Journal of Physical Chemistry B* **2005**, *109*, 2846.

(16) Zeng, T.; Wen, X.-D.; Li, Y.-W.; Jiao, H. *Journal of Physical Chemistry B* **2005**, *109*, 13704.

(17) Travert, A.; Dujardin, C.; Mauge, F.; Cristol, S.; Paul, J. F.; Payen, E.; Bougeard, D. *Catalysis Today* **2001**, *70*, 255.

(18) Gemming, S.; Tamuliene, J.; Seifert, G.; Bertram, N.; Kim, Y. D.; Gantefor, G. *Applied Physics A* **2005**.

(19) Murugan, P.; Kumar, V.; Kawazoe, Y.; Ota, N. *Physical Review A* **2005**, *71*, 063203.

(20) Murugan, P.; Kumar, V.; Kawazoe, Y.; Ota, N. *Journal of Physical Chemistry A* **2007**, *111*, 2778.

(21) Seifert, G.; Tamuliene, J.; Gemming, S. *Computational Materials Science* **2006**, *35*, 316.

(22) Klabunde, K. J.; Mulukutla, R. S. Chemical and Catalytic Properties of Nanocrystals. In *Nanoscale Materials in Chemistry*; Klabunde, K. J., Ed.; John Wiley and Sons, 2001; pp 223.

(23) Echt, O.; Sattler, K.; Recknagel, E. *Physical Review Letters* **1981**, *47*, 1121.

(24) Knight, W. D.; Clemenger, K.; Heer, W. A. d.; Saunders, W. A.; Chou, M. Y.; Cohen, M. L. *Physical Review Letters* **1984**, *52*, 2141.

(25) Martin, T. P.; Bergmann, T.; Gohlich, H.; Lange, T. *Chemical Physics Letters* **1990**, *172*, 209.

(26) Bell, R. C.; Zemski, K. A.; Justes, D. R.; A. W. Castleman, J. *Journal of Chemical Physics* **2001**, *114*, 798.

(27) Deng, H. T.; Kerns, K. P.; A. W. Castleman, J. *Journal of the American Chemical Society* **1996**, *118*, 446.

(28) Guo, B. C.; Kerns, K. P.; A. W. Castleman, J. *Journal of the American Chemical Society* **1993**, *115*, 7415.

(29) Deng, H. T.; Kerns, K. P.; A. W. Castleman, J. *Journal of Physical Chemistry* **1996**, *100*, 13386.

(30) Lightstone, J. M.; Mann, H. A.; Wu, M.; Johnson, P.; White, M. G. *Journal of Physical Chemistry B* **2003**, *107*, 10359.

(31) Leskiw, B. D.; A. W. Castleman, J. *C. R. Physique* **2002**, *3*, 251.

(32) Lightstone, J. M.; Patterson, M.; White, M. G. *Journal of Physical Chemistry A* **2006**, *110*, 3505.

(33) Lightstone, J. M.; Patterson, M. J.; Liu, P.; J. C. Lofaro, J.; White, M. G. *Journal of Physical Chemistry C* **2008**, *112*, 11495.

(34) Lightstone, J. M.; Patterson, M. J.; White, M. G. *Chemical Physics Letters* **2005**, *413*, 429.

(35) Patterson, M. J.; Lightstone, J. M.; White, M. G. *Journal of Physical Chemistry A* **2008**, *112*, 12011.

(36) Heiz, U.; Vanolli, F.; Trento, L.; Schneider, W.-D. *Review of Scientific Instruments* **1997**, *68*, 1986.

(37) Boyd, K. J.; Lapicki, A.; Aizawa, M.; Anderson, S. L. *Review of Scientific Instruments* **1998**, *69*, 4106 and references therein.

(38) Nayak, S. K.; Jena, P.; Stepanyuk, V. S.; Hergert, W.; Wildberger, K. *Physical Review B* **1997**, *56*, 6952.

(39) Binns, C. *Surface Science Reports* **2001**, *44*, 1.

(40) Bertram, N.; Kim, Y. D.; Gantefor, G.; Sun, Q.; Jena, P.; Tamuliene, J.; Seifert, G. *Chemical Physics Letters* **2004**, *396*, 341.

(41) Gemming, S.; Tamuliene, J.; Seifert, G.; Bertram, N.; Kim, Y. D.; Gantefor, G. *Applied Physics A* **2005**, *82*, 161.

(42) Thomas, M.; Dickinson, J. T.; Poppa, H.; Pound, G. M. *Journal of Vacuum Science and Technology* **1978**, *15*, 568.

(43) Lauritsen, J. V.; Bollinger, M. V.; Laegsgaard, E.; Jacobsen, K. W.; Norskov, J. K.; Clausen, B. S.; Topsoe, H.; Besenbacher, F. *Journal of Catalysis* **2004**, *221*, 510.

(44) Lauritsen, J. V.; Kibsgaard, J.; Helvig, S.; Clausen, B. S.; Topsoe, H.; Laegsgaard, E.; Besenbacher, F. *Nature* **2007**, *2*, 53.

(45) Lauritsen, J. V.; Nyberg, M.; Norskov, J. K.; Clausen, B. S.; Topsoe, H.; Laegsgaard, E.; Besenbacher, F. *Journal of Catalysis* **2004**, *224*, 94.

(46) Lauritsen, J. V.; Nyberg, M.; Vang, R. T.; Norskov, J. K.; Clausen, B. S.; Topsoe, H.; Laegsgaard, E.; Besenbacher, F. *Nanotechnology* **2003**, *14*, 385.

(47) Rodriguez, J. A.; Dvorak, J.; Jirsak, T.; Hrbek, J. *Surface Science* **2001**, *490*, 315.

(48) Hrbek, J.; Hwang, R. Q. *Current Opinion in Solid State and Materials Science* **2001**, *5*, 67.

(49) Song, Z.; Cai, T.; Rodriguez, J. A.; Hrbek, J.; Chan, A. S. Y.; Friend, C. M. *Journal of Physical Chemistry B* **2003**, *107*, 1036.

(50) Potapenko, D. V.; Horn, J. M.; Beuhler, R. J.; Song, X.; White, M. G. *Surface Science* **2005**, *574*, 244.

(51) Horn, J. M.; Song, Z.; Potapenko, D. V.; Hrbek, J.; White, M. G. *Journal of Physical Chemistry* **2004**, *109*, 44.

(52) Potapenko, D. V.; Horn, J. M.; White, M. G. *Journal of Catalysis* **2005**, *236*, 346–355.

(53) Biener, M. M.; Biener, J.; Friend, C. M. *Journal of Chemical Physics* **2005**, *122*, 34706.

(54) Gemming, S.; Seifert, G. *Applied Physics A* **2005**, *82*, 175.

(55) Popov, I.; Gemming, S.; Seiffert, G. *Physical Review B* **2007**, *75*, 245436.

(56) Popov, I.; Kunze, T.; Gemming, S.; Seifert, G. *European Physical Journal D: Atomic, Molecular, Optical and Plasma Physics* **2007**, *45*, 439.

(57) Helveg, S.; Lauristen, J. V.; Laegsgaard, E.; Stensgaard, I.; Norskov, J. K.; Clausen, B. S.; Toposoe, H.; Besenbacher, F. *Physical Review Letters* **2000**, *84*, 951.

(58) Bollinger, M. V.; Lauritsen, J. V.; Jacobsen, K. W.; Norskov, J. K.; Helvig, S.; Besenbacher, F. *Physical Review Letters* **2001**, *87*, 196803.

(59) Umarji, A. M.; Rao, G. V. S.; Janawadkar, M. P.; Radhakrishnan, T. S. *Journal of Physics and Chemistry of Solids* **1980**, *41*, 421.

(60) Mancour-Billah, A.; Chevrel, R. *Journal of Solid State Chemistry* **2003**, *170*, 281.

(61) Paskach, T. J.; Schrader, G. L.; McCarley, R. E. *Journal of Catalysis* **2002**, *211*, 285.

(62) Heiz, U.; Schneider, W. *Journal of Physics - D Applied Physics* **2000**, *33*, R85.

(63) Haberland, H.; Karrais, M.; Mall, M.; Thurner, Y. *Journal of Vacuum Science and Technology A* **1992**, *10*, 3266.

(64) Haberland, H.; Mall, M.; Moseler, M.; Qiang, Y.; Reiners, T.; Thurner, Y. *Journal of Vacuum Science and Technology A* **1994**, *12*, 2925.

(65) Gerlich, D. State-Selected and State-toState Ion-Molecule Reaction Dynamics, Part 1: Experiment. In *Advances in Chemical Physics Series, Vol. LXXXII*; Ng, C. Y., Baer, M., Eds.; John Wiley & Sons, Inc.: New York, 1992.

(66) Jones, R. M.; Anderson, S. L. *Review of Scientific Instruments* **2000**, *71*, 4335.

(67) Moore, J. H.; Davis, C. C.; Coplan, M. A. *Building Scientific Apparatus: A Practical Guide to Design and Construction*; Perseus Books Group: Cambridge, 2002.

(68) Deng, H. T.; Kerns, K. P.; Castleman, A. W. *Journal of the American Chemical Society* **1996**, *118*, 446.

(69) Leuchtner, R. E.; Harms, A. C.; A. W. Castleman, J. *Journal of Chemical Physics* **1989**, *92*, 6527.

(70) Vajda, S.; Wolf, S.; Leisner, T.; Busolt, U.; Woste, L. H. *Journal of Chemical Physics* **1997**, *107*, 3492.

(71) Loh, S. K.; Hales, D. A.; Lian, L.; Armentrout, P. B. *Journal of Chemical Physics* **1989**, *90*, 5466.

(72) Guzowski, J. P., Jr.; Hieftje, G. M. *Journal of Analytical Atomic Spectroscopy* **2001**, *16*, 781.

(73) Tanner, S. D.; Baranov, V. I. *Atomic Spectroscopy* **1999**, *20*, 45.

(74) Mahaffy, P. R.; Lai, K. *Journal of Vacuum Science and Technology A* **1990**, *8*, 3244.

(75) Hammer, B.; Morikawa, Y.; Norskov, J. K. *Physical Review Letters* **1996**, *76*, 2141.

(76) Chourasia, A. R.; Chopra, D. R. Auger Electron Spectroscopy. In *Handbook of Instrumental Techniques for Analytical Chemistry*; Settle, F. A., Ed.; Prentice Hall: Upper Saddle River, 1997.

(77) Woodruff, D. P.; Delchar, T. A. *Modern techniques of surface science*; Cambridge University Press: Cambridge, 1986.

(78) Dance, I. G.; Fischer, K. J.; Willett, G. D. *Journal of the Chemical Society, Dalton Transactions* **1997**, 2557.

(79) Nakat, J. H. E.; Dance, I. G.; Fischer, K. J.; Rice, D.; Willett, G. D. *Journal of the American Chemical Society* **1991**, *113*, 5141.

(80) Dance, I. G. *Chemical Communications* **1998**, *5*, 523.

(81) Zhang, N.; Yu, Z.; Wu, X.; Gao, Z.; Zhu, Q.; Kong, F. *Journal of the Chemical Society, Faraday Transactions* **1993**, *89*, 1779.

(82) Nakat, J. E.; Fisher, K. J.; Dance, I. G.; Willet, G. D. *Inorganic Chemistry* **1993**, *32*, 1931.

(83) Dance, I. G.; Fisher, K. J.; Willett, G. D. *Inorganic Chemistry* **1996**, *35*, 4177.

(84) Gemming, S.; Siefert, G. "Electronic Properties of Novel Nanostructures", *AIP Conference Proceedings,* **2005***,786, 353*

(85) Gemming, S.; Seifert, G. "Novel Enlongated Molybdenum Sulfide Nanostructures" *AIP Conference Proceedings* **2005**, *786*, 353.

(86) Koelling, D. D.; Harmon, B. N. *Journal of Physical Chemistry C: Solid State Physics* **1977**, *10*, 3107.

(87) He, S.-G.; Xie, Y.; Guo, Y.; Bernstein, E. *The Journal of Chemical Physics* **2007**, *126*, 194315.

(88) Hadjikyriacou, A. I.; Coucouvanis, D. *Inorganic Chemistry* **1987**, *26*, 2400.

(89) Hibble, S. J.; Feaviour, M. R.; Almond, M. J. *Dalton Transactions* **2001**, *6*, 935.

(90) Llusar, R.; Uriel, S.; Vicent, C.; Clemente-Juan, J. M.; Coronado, E.; Gomez-Garcia, C. J.; Braida, B.; Canadell, E. *Journal of the American Chemical Society* **2004**, *126*, 12076.

(91) Muller, A.; Sarkar, S.; Bhattacharyya, R. G.; Pohl, S.; Dartman, M. *Angewandte Chemie International Edition* **1978**, *17*, 535.

(92) Guo, B. C.; Kerns, K. P.; Castleman, A. W. *Journal of Chemical Physics* **1992**, *96*, 8177.

(93) Davidson, E. R.; Kunze, K. L.; Machado, F. B. C.; Chakravorty, S. J. *Accounts of Chemical Research* **1993**, *26*, 628.

(94) Zeng, T.; Wen, X.-D.; Wu, G.-S.; Li, Y.-W.; Jiao, H. *Journal of Physical Chemistry B* **2005**, *109*, 2846.

(95) Paskach, T. J.; Hilsenbeck, S. J.; Thompson, R. K.; McCarley, R. E.; Schrader, G. L. *Journal of Alloys and Compounds* **2000**, *311*, 169.

(96) Zeng, T.; Wen, X.-D.; Li, Y.-W.; Jiao, H. *Journal of Physical Chemistry B* **2005**, *109*, 13704.

(97) Speight, J. G. *The Chemistry and Technology of Petroleum*, second ed.; McGraw-Hill: New York, 1991.

(98) Delmon, B.; Froment, G. F. *Catalysis Reviews - Science and Engineering* **1996**, *38*, 69.

(99) Prins, R.; deBeer, V. H. J.; Somorjai, G. A. *Catalysis Reviews - Science and Engineering* **1989**, *31*, 1.

(100) Lauritsen, J. V.; Vang, R. T.; Besenbacher, F. *Catalysis Today* **2006**, *111*, 34 and references therein.

(101) Aizawa, M.; Lee, S.; Anderson, S. L. *Journal of Chemical Physics* **2002**, *117*, 5001.

(102) Busolt, U.; Cottancin, E.; Rohr, H.; Socaciu, L.; Leisner, T.; Woste, L. *Applied Physics B* **1999**, *68*, 453.

(103) Haberland, H.; Insepov, Z.; Moseler, M. *Physical Review B* **1995**, *51*, 11061.

(104) Vandoni, G.; Felix, C.; Goyhenex, C.; Monot, R.; Buttet, J.; Harbich, W. *Surface Science* **1995**, *331-333*, 838.

(105) Blochl, P. E. *Physical Review B* **1994**, *50*, 17953.

(106) Kresse, G.; Hafner, J. *Physical Review B* **1993**, *47*, 558.

(107) Kresse, G.; Furthmuller, J. *Physical Review B* **1996**, *54*, 11169.

(108) Perdew, J. P.; Erzerhof, M. *Physical Review Letters* **1996**, *77*, 3865.

(109) Monkhorst, H. J.; Pack, J. D. *Physical Review B* **1976**, *13*, 5188.

(110) Huang, J. M.; Laitinen, R. A.; Kelley, D. F. *Physical Review B* **2000**, *62*, 10995.

(111) Liu, P.; Rodriguez, J. A.; Muckerman, J. T.; Hrbek, J. *Surface Science* **2003**, *530*, L313.

(112) Powell, C. J.; Jablonski, A. *NIST Electron Effective-Attenuation-Length Database Version 1.1*; National Institute of Standards and Technology: Gaithersburg, 2003.

(113) France, C. B.; Parkinson, B. A. *Applied Physics Letters* **2003**, *82*, 1194.

(114) Andreev, T.; Barke, I.; Hovel, H. *Physical Review B* **2004**, *70*, 205426 and references therein.